A STUDY OF THE FLOW RESISTANCE OF COMPOSITE POROUS STRUCTURES

A thesis submitted by

John F. Perry

B.S.ChE. 1963, The University of Wisconsin
M.S. 1965, Lawrence University

in partial fulfillment of the requirements
of The Institute of Paper Chemistry
for the degree of Doctor of Philosophy
from Lawrence University,
Appleton, Wisconsin

June, 1968

TABLE OF CONTENTS

SUMMARY

A review of the literature on the aqueous permeation of fibrous mats points out discrepancies between thick mat and thin-mat studies. Several authors have speculated that this discrepancy for the thin mats is the result of a hydrodynamic interaction between the mat and the forming wire screen. This interaction becomes negligible for the thick-mat studies. Meyer (8) has studied this phenomenon for isotropic D'Arcy mats in ideal flow for straight bridging and draped mats. His results indicate the interaction to be a function of the amount of drape, with no interaction occurring for straight bridging mats.

The mat-wire system was modeled physically by representing the forming wire as a parallel array of cylinders and the mat as a stack of nondeformable wire screens. Pressure drop-velocity data were obtained for mats of two different porosity values over a range of ratios of mat thickness-to-cylinder radius of 0.0 to 3.4. The ratio of the distance between the cylinder centers to cylinder radius was held at a constant value of 4.0. The experimental results indicated a specific interaction taking place. The interaction appears to be independent of the mat thickness, and has a magnitude about two times greater than the resistance of the bare cylinders.

Finite difference approximations were introduced into the Navier-Stokes equation and solutions were obtained for two-dimensional flow past the parallel array of cylinders at Reynolds numbers of 2, 10, 20, 40, and 60. These solutions agreed with the experimental data and are consistent with the results of Tamada and Fujikawa (32) and Miyagi (33). The Navier-Stokes equations were modified according to Brinkman (31) to include the effects of an isotropic porous medium obeying D'Arcy's equation. The numerical results confirm the nature of the interaction. Further analysis shows the resistance of the cylinder to increase by about 25% as a result of the presence of the porous medium. This portion, however, represents only about 10% of the total interaction. Since the wake of

the parallel array of cylinders is unaffected by the presence of the mat as shown by the mathematical model, it is concluded that the major portion of the interaction takes place in the mat. This interaction is observed as a shift in the upstream streamlines due to the presence of the mat.

This flow convergence effect in a real fiber mat-wire system is expected to be dependent upon the wire geometry as well as the mat properties. Because of the nature of the interaction between the fiber mat and wire, it is necessary to consider the system as a single entity rather than two separate elements. Suggestions for further work include refinements to the mathematical model for the purpose of possibly characterizing the interaction on the basis of mat and wire properties.

INTRODUCTION

Considerable work has been done in recent years to quantitatively describe the process of filtration and permeation of fibrous systems basic to the paper industry. Essentially, the equations used to describe the flow through porous media are applied to the flow through fiber mats (1).

Generally, the Forchheimer equation is employed (2) for a uniform fiber mat where the pressure loss, ΔP, across the mat is related to the approach velocity, U_∞, by the following.

$$\Delta P = aU_\infty + bU_\infty^2. \tag{1}$$

Hence, the coefficient, a, is the viscous resistance and may be defined by the following equation:

$$a = \frac{\alpha S^2 (1 - \varepsilon)^2 \mu t}{\varepsilon^3} \tag{2}$$

where t is the thickness of the porous medium, ε is the porosity, S is the specific surface of the porous medium based on the volume of the solid component, and μ is the viscosity of the fluid. The viscous resistance coefficient, α, is usually interpreted as the Kozeny constant found in the D'Arcy equation of flow through porous media at low flow rates. The inertial resistance, b, may be defined by

$$b = \frac{\beta S (1 - \varepsilon) \rho t}{\varepsilon^3} \tag{3}$$

where ρ is the density of the fluid and β is the inertial resistance coefficient.

When applying these relationships to fibrous mats, it is necessary to take the compressibility into account. The effect of compressibility will cause a porosity gradient in the mat. Since the Kozeny constant is highly dependent on the porosity for values of $\varepsilon > 0.75$, the need for this correction is apparent.

Independent experimental studies on compressibility have been performed, and these results can be incorporated into the Forchheimer equation.

In experimental studies of flow through fiber mats, the pressure drop across the mat is usually measured. It is necessary, however, to obtain the pressure drop across the mat and a forming wire screen, since the mat cannot be suspended independently. The pressure drop across the wire screen, as determined from independent studies, is subtracted from the overall pressure drop to yield a computed mat pressure loss. Results from such operations have been well documented in the literature (3, 4).

While these equations work well for thick mats, it has been observed that discrepancies appear for thin mats (basis weight < 50 g./m.^{2}) (2). The experimental pressure drops were higher than those determined by extrapolation of thick-mat results. The discrepancy became greater as the mat thickness approached zero. This phenomenon is called the mat-wire interaction.

Ingmanson (5) in a discussion of the mat-wire interaction considered four effects: (a) flow convergence, (b) pore size distribution, (c) porosity distribution, and (d) compressibility. Flow convergence is a term used to describe the effect of the forming wire on the upstream flow pattern in the mat. The component wires of the forming screen are about an order of magnitude larger than the fibers comprising the mat. As the fluid passes through the mat and approaches the forming wire, the streamlines begin to diverge around the individual wires. This gives the appearance of the flow lines converging toward the openings in the wire screen. The increased resistance of the mat is believed to be the result of a higher velocity gradient in the mat and, as a consequence, a higher shear stress on the internal surfaces of the porous medium.

The pore size distribution is a factor to consider since the terms in the Forchheimer equation are defined strictly for a uniform pore size distribution. The porosity distribution effect arises from the method in which the porosity in the mat is determined. The compressibility effect is the result of assuming that the deformability of a mat is independent of the mat thickness even though the mat densities are the same. Ingmanson concluded from experimental studies that only the flow convergence and porosity distribution contribute to the mat-wire interaction, the latter effect accounting for about 15% of the total interaction.

Another factor which has been suggested (6, 7) as a possible contribution to the mat-wire interaction is the penetration of the mat into the forming wire screen. This penetration is due to the manner in which the mat is initially formed and to the deformable nature of the mat under a load.

Meyer (8) made a study of the flow convergence and mat penetration contributions to the mat-wire interaction by means of an ideal system. The forming wire was simulated by a parallel array of cylinders. An isotropic porous medium obeying D'Arcy's equation was used to represent the fiber mat. The unperturbed flow pattern past the cylinders for irrotational flow was superimposed on the mat. Obtaining mat-averaged velocities, Meyer was able to derive a flow convergence correction factor. His results showed that this factor is dependent upon the degree of mat penetration and mat thickness. For zero penetration (straight bridging mat), there is no interaction; however, as the penetration increases, the interaction becomes significant. For thin mats the interaction is large and, as the mat thickness increases, the interaction tends to approach a zero asymptote. Application of his model to experimental fiber mat and wire screen system accounts for about a third of the total mat-wire interaction. It should be noted, however, that the lack of complete quantitative agreement may be due to the compressibility and porosity distribution effects described earlier.

Most of the effects which are believed to comprise the mat-wire interaction have been associated with the mat per se. There is another effect which this author believes should be accounted for in the mat-wire interaction phenomenon. The use of fluid resistance elements such as wire screens and grids have long been recognized as devices for producing desirable velocity profiles in flow tunnels (9-12). Applying this same concept to the mat, it would be expected that the presence of the mat would alter the flow pattern around the cylinders and thus affect their resistance to flow. Whether this effect will result in a positive or negative contribution to the mat-wire interaction is a matter which has not been described in the literature.

STATEMENT OF THE PROBLEM

This thesis is concerned with only two of the previously mentioned factors which are believed to contribute to the mat-wire interaction; namely, the flow convergence effect and the effect of the presence of the mat on the resistance of the cylinders. For the purpose of this study, these two factors are jointly referred to as the hydrodynamic interaction of the mat-wire system.

In view of the fact that the compressibility effect has not been clearly resolved and that the porosity distribution and mat penetration effects are complex, it is desirable to eliminate these factors from this study. In order to accomplish this exclusion, an ideal mat-wire system is used in this study.

A real wire screen is a three-dimensional system whose microscopic boundaries cannot be readily described. As a consequence, the equations of flow through the grid cannot be solved. In order to alleviate this problem, the wire screen is replaced with a simple two-dimensional system which consists of a parallel array of infinite cylinders or rods. This model is the same as that used by Meyer (8).

The model mat must be incompressible and have a fairly uniform pore size and porosity distribution, as was mentioned earlier. Layers of wire screens were chosen as the material for the simulated fiber mat to meet these requirements. It should be pointed out, however, that these mats do not have pure isotropic character usually associated with simple porous media models.

The objective of this thesis study is to investigate the hydrodynamic interaction and to ascertain the nature of it. For this ideal mat-wire system, the interaction (I) may be defined in terms of the bare cylinders (BC), the bare mat (BM), and the combined system (C) in the following form.

$$\Delta P_I = \Delta P_C - (\Delta P_{BC} + \Delta P_{BM}) \qquad (4)$$

where the ΔP's are the pressure drops or losses. Equation (4) is stated for convenience only and does not imply that the interaction effect is simply additive.

A mathematical model based on the Navier-Stokes equations, and an experimental program are included in this study. The results of each phase are combined to form the analysis of the interaction phenomenon.

THEORETICAL MODEL OF MAT-CYLINDER SYSTEM

DESCRIPTION OF MODEL

Having defined the idealized mat-wire system as a nondeformable porous medium situated on a parallel array of clinders, a mathematical model is constructed for describing the flow through such a system. The basis of the model is the Navier-Stokes equation as applied to the parallel array of cylinders shown in Fig. 1.

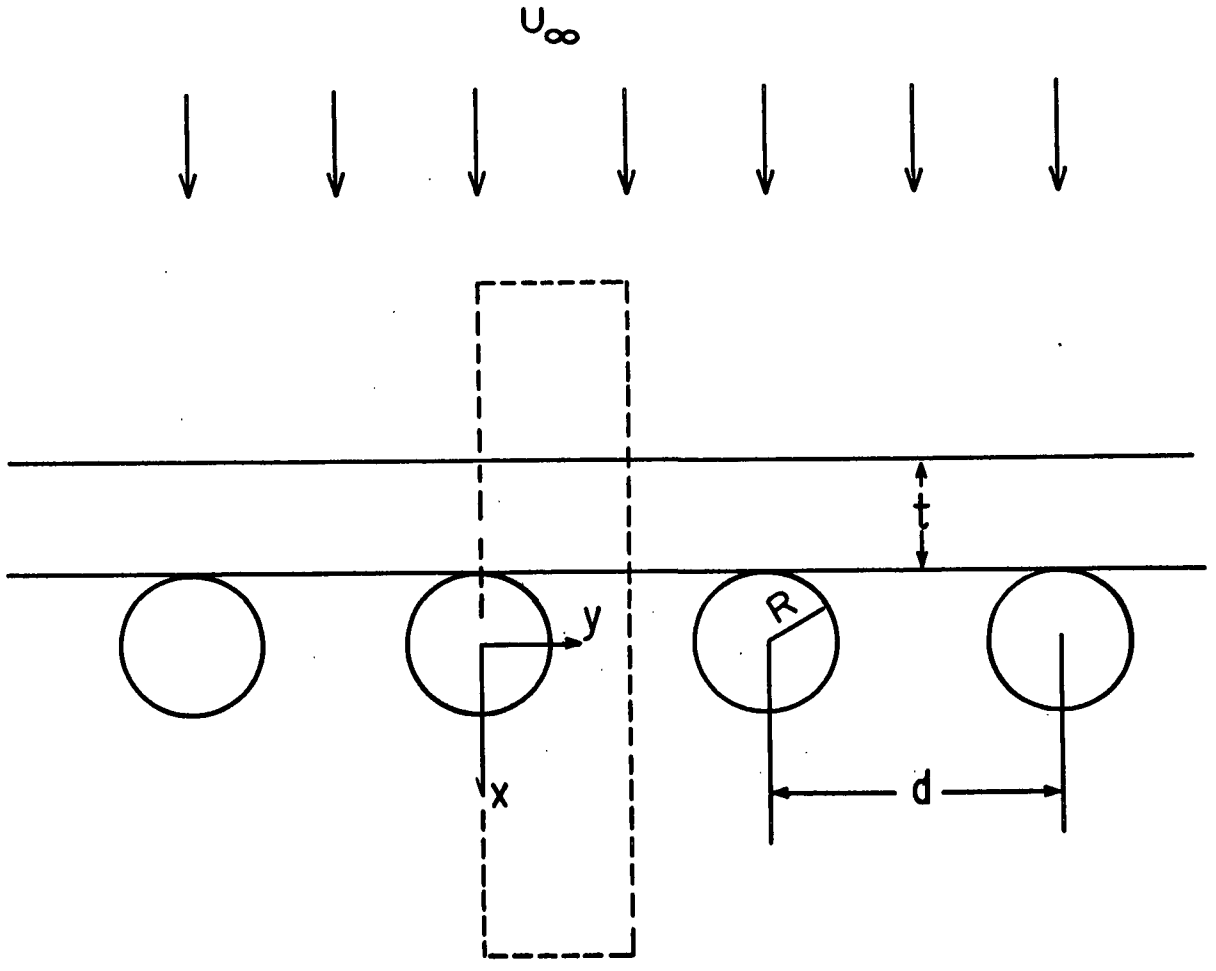

Figure 1. Definition of Parallel Array of Cylinders

The array is composed of infinitely long cylinders of radius, R, and spacing between centers, d. For reasons of symmetry, a unit cell containing only 1/2 of a cylinder is necessary. The fluid is assumed to be incompressible and to have constant viscosity.

With the velocity vector, $\vec{w}$, for the two-dimensional flow case defined as

$$\vec{w} = u(x,y,T)\vec{i} + v(x,y,T)\vec{j} \tag{5}$$

the system of Navier-Stokes equations is

$$\frac{\partial \vec{w}}{\partial T} + (\vec{w} \cdot \nabla)\vec{w} = \frac{1}{\rho}\left[-\nabla P + \rho\vec{g} + \mu\nabla^2\vec{w}\right]. \tag{6}$$

The equation of continuity is

$$\nabla \cdot \vec{w} = 0. \tag{7}$$

The boundary conditions for this problem are

$$u = U_\infty, \quad v = 0, \quad x = \pm\infty \tag{8}$$

$$v = 0, \quad y = 0 \tag{8a}$$

$$v = 0, \quad y = d/2 \tag{8b}$$

and

$$u = v = 0, \quad x = \pm\sqrt{R^2 - y^2} \tag{9}$$

This system of equations now constitutes a complete mathematical description of the problem.

THE VORTICITY TRANSPORT EQUATION

In order to simplify the solution of this equation, the vorticity is introduced and is generally defined as $\vec{\omega} = \text{curl}\ \vec{w}$. This quantity is twice the local angular velocity of the fluid. For two-dimensional flow in the x-y plane, the vorticity has

only one component which is given by

$$\omega = \text{curl } \vec{w} = \omega\vec{k} = \left(\frac{\partial v}{\partial x} - \frac{\partial u}{\partial y}\right) \vec{k}. \tag{10}$$

By taking the curl of each side of Equation (6), one obtains

$$\frac{\partial \vec{\omega}}{\partial T} + (\vec{w} \cdot \nabla)\, \vec{\omega} - (\omega \cdot \nabla)\vec{w} = \nu\, \nabla^2 \vec{\omega}. \tag{11}$$

which for the two dimensional system reduces to Equation (12)

$$\frac{\partial \omega}{\partial T} + u\frac{\partial \omega}{\partial x} + v\frac{\partial \omega}{\partial y} = \nu \left(\frac{\partial^2 \omega}{\partial x^2} + \frac{\partial^2 \omega}{\partial y^2}\right) = \nu\, \nabla^2 \omega. \tag{12}$$

This equation is referred (13) to as the vorticity transport equation. The stream function, ψ, defined by Equation (13) is introduced,

$$u = \frac{\partial \psi}{\partial y} \qquad\qquad v = -\frac{\partial \psi}{\partial x} \tag{13}$$

so that the vorticity from Equation (1) becomes

$$\omega = -\nabla^2 \psi = -\left(\frac{\partial^2 \psi}{\partial x^2} + \frac{\partial^2 \psi}{\partial y^2}\right) \tag{14}$$

and the vorticity transport equation then becomes

$$\frac{\partial \omega}{\partial T} + \frac{\partial \psi}{\partial y}\frac{\partial \omega}{\partial x} - \frac{\partial \psi}{\partial x}\frac{\partial \omega}{\partial y} = \nu\, \nabla^2 \omega. \tag{15}$$

Equations (14) and (15) represent the system of equations describing the problem when the boundary conditions are specified. These two equations are then made nondimensional with respect to the radius of the cylinder, R, and the approach velocity, U_∞, with the following set of equations:

$$X = x/R \tag{16}$$

$$Y = y/R \tag{17}$$

$$\Psi = \psi/(U_\infty R) \tag{18}$$

$$\Omega = \omega R/U_\infty. \tag{19}$$

Equation (14) appears as

$$-\Omega = \nabla^2\Psi. \tag{20}$$

For the purpose of this study, only the steady state case for the vorticity transport equation will be considered. The unsteady case would involve the shedding of vortices which occur at Reynolds numbers between 50 and 90, although some authors report shedding as low as 40 (14-16). Since the flow rates in the experimental program were low ($\underline{Re} < 60$, where $\underline{Re}$ is based on the approach velocity and the diameter of the cylinder), the steady state solutions may be used. The vorticity transport Equation (15), in nondimensional terms is given by

$$\nabla^2\Omega = \frac{Re}{2}\left(\frac{\partial\Psi}{\partial Y}\frac{\partial\Omega}{\partial X} - \frac{\partial\Psi}{\partial X}\frac{\partial\Omega}{\partial Y}\right) \tag{21}$$

for the steady state case, where the Reynolds number is $\underline{Re} = 2\underline{RU}_\infty/\nu$.

The boundary conditions presented earlier [Equation (8) and (9)] may now be stated in terms of the vorticity and stream function.

$$\frac{\partial\Psi}{\partial Y} = 1, \quad \frac{\partial\Psi}{\partial X} = 0, \quad \Omega = 0, \quad X = \pm\infty \tag{22}$$

$$\Psi = 0, \quad \Omega = 0, \quad Y = 0 \tag{23}$$

$$\Psi = \text{constant}, \quad \Omega = 0, \quad Y = \frac{d}{2R}. \tag{24}$$

For the condition of no "slip" (i.e., $\underline{u}=\underline{v}=0$) at the solid boundary, it is convenient to consider a coordinate system where $\underline{s}$ is in the direction tangential to the contour of the surface and $\underline{n}$ is in the direction of the normal to the contour. As a result, the condition of no slip may be expressed as follows:

$$\frac{\partial\Psi}{\partial n} = \frac{\partial\Psi}{\partial s} = \Psi = 0. \tag{25}$$

Equations (20)-(25) represent the system of equations describing the flow problem.

FINITE DIFFERENCE APPROXIMATIONS

A solution of the vorticity transport equation by analytical means is nearly impossible to achieve. Attempts to do so have resulted in assumptions which have given results valid for only limited conditions. Examples of such solutions are the Lamb solution for very low Reynolds numbers past cylinders and potential flow with boundary layer theory for very large Reynolds numbers. In recent years, there have been several articles published in regard to numerical solutions of the complete Navier-Stokes equations in two-dimensional flow systems (14, 17-23). Numerical techniques have been developed and tested in view of the need for more accurate solutions and the availability of high-speed digital computers.

In view of the fact that there are quite a few methods for approximating differential equations, the method of simple finite difference approximations was chosen. The basis of this choice rests on the simplicity of the procedure and the fact that satisfactory results have been reported for similar flow problems.

The formal finite difference approximations are introduced into the differential equations presented earlier. These approximations have been truncated after the first differences. An example of central finite difference approximations for the first and second derivatives of a function, f, are given below:

$$\left.\frac{\partial f}{\partial x}\right|_{i,j} = \frac{f_{i+1,j} - f_{i-1,j}}{2h} + \frac{h^2}{6}\frac{\partial^3 f}{\partial x^3} \qquad (26)$$

$$\left.\frac{\partial^2 f}{\partial x^2}\right|_{i,j} = \frac{f_{i+1,j} - 2f_{i,j} + f_{i-1,j}}{h^2} + \frac{h^2}{12}\frac{\partial^4 f}{\partial x^4}. \qquad (27)$$

Here, h is the finite difference interval as shown in Fig. 2.

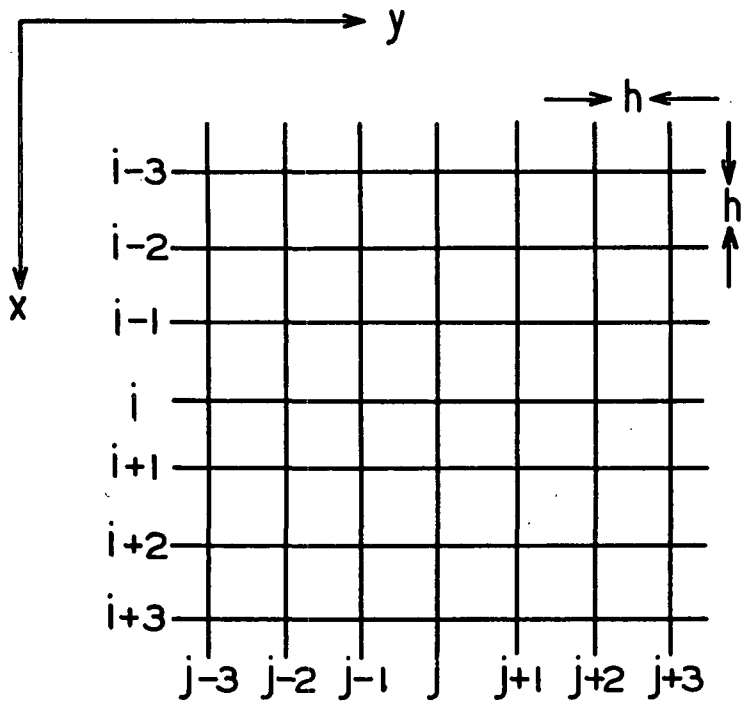

Figure 2. Finite Difference Grid

The approximation of Equation (20) in finite difference form becomes

$$\Psi_{i,j} = (\Psi_{i,j+1} + \Psi_{i,j-1} + \Psi_{i+1,j} + \Psi_{i-1,j} + h^2\Omega_{i,j})/4 + O(h^4). \qquad (28)$$

Similarly, the vorticity transport equation, presented as Equation (21), becomes

$$\Omega_{i,j} = \Omega_M - \frac{Re}{32}[(\Omega_{i+1,j} - \Omega_{i-1,j})(\Psi_{i,j+1} - \Psi_{i,j-1}) - (\Omega_{i,j+1} - \Omega_{i,j-1}) \times (\Psi_{i+1,j} - \Psi_{i-1,j})] \qquad (29)$$

where

$$\Omega_M = \frac{1}{4}(\Omega_{i,j+1} + \Omega_{i,j-1} + \Omega_{i+1,j} + \Omega_{i-1,j}). \qquad (30)$$

Since this form of the vorticity transport equation cannot be applied to the solid boundary of the cylinder where the condition of no slip is required, it is

necessary to formulate another equation. The details of the treatment of the boundary are presented in Appendix I. The finite difference equation for this boundary is given in Equation (31).

$$\Omega_B = 2(\Psi_B - \Psi_A)/h^2. \tag{31}$$

The subscript, B, refers to a boundary value, while the subscript, A, refers to a value a distance h in the direction of the normal to the boundary.

COORDINATE TRANSFORMATION

When the Cartesian grid is placed over the two-dimensional plane, z, shown in Fig. 1, it becomes apparent that serious problems will arise in the use of the finite difference equations along the curved boundaries of the cylinder surface. The grid points in the Cartesian grid do not fall on the boundary of the cylinder, thus making the finite difference equations unusable in the form presented here. Elimination of the curved boundary may be accomplished by means of a transformation to a different coordinate system.

The new plane, ξ, is described by the complex potential associated with the irrotational flow problem. The complex potential for the parallel array of cylinders, as derived by Meyer (8) and published by Han (2), is

$$\zeta + i\eta = U_\infty \left[z + \frac{d}{\pi} \sinh^2\left(\frac{\pi r}{d}\right) \coth\left(\frac{\pi z}{d}\right) \right]. \tag{32}$$

Here, ζ is the velocity potential, η is the stream function for irrotation flow and z is the complex variable x + iy. Figure 3 is a comparison of the two planes, z and ξ. The solution in plane z is related to the solution of the ξ plane through the Jacobian of transformation, J, which is (24)

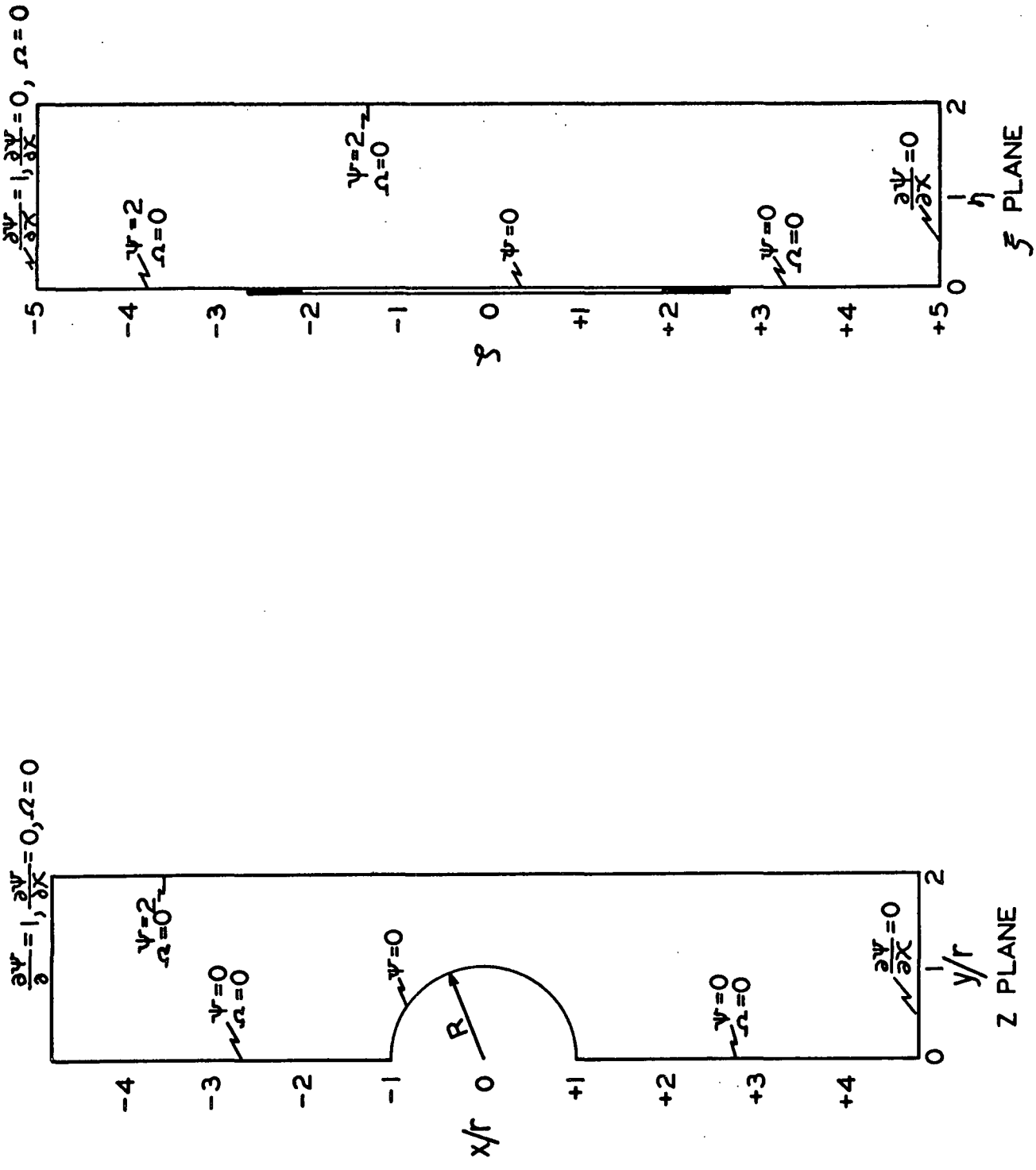

Figure 3. Two-Dimensional Planes for Numerical Solution

$$J = \frac{\partial \zeta}{\partial x}\frac{\partial \eta}{\partial y} - \frac{\partial \zeta}{\partial y}\frac{\partial \eta}{\partial x} . \tag{33}$$

Using the Cauchy-Riemann equations, the Jacobian may be evaluated from

$$J = \left(\frac{\partial \eta}{\partial x}\right)^2 + \left(\frac{\partial \eta}{\partial y}\right)^2 = \left(\frac{\partial \zeta}{\partial x}\right)^2 + \left(\frac{\partial \zeta}{\partial y}\right)^2 . \tag{34}$$

The correspondence between the solution in one plane and the solution in the other plane* is given by

$$\nabla^2_{(x,y)}\Psi = J \cdot \nabla^2_{(\zeta,\eta)}\Psi \tag{35}$$

Thom (19) refers to this Jacobian as the "velocity of transformation," since the net velocity, q, is related by

$$q^2_{(x,y)} = J \cdot q^2_{(\zeta,\eta)} = J \cdot \left[\left(\frac{\partial \Psi}{\partial \zeta}\right)^2 + \left(\frac{\partial \Psi}{\partial \eta}\right)^2\right] . \tag{36}$$

In order to use the Jacobian in the nondimensional finite difference equations, the complex potential [Equation (32)] is first made nondimensional. The Jacobian is then computed using derivatives of these resulting values. The finite difference equation for computing the stream function [Equation (24)] is now

$$\Psi_{i,j} = (\Psi_{i,j+1} + \Psi_{i,j-1} + \Psi_{i+1,j} + \Psi_{i-1,j} + \frac{h^2}{j}\Omega_{i,j})/4 . \tag{37}$$

The no slip boundary equation [Equation (31)] also appears as

$$\Omega_B = 2J_B(\Psi_B - \Psi_A)/h^2 . \tag{38}$$

The Jacobian does not appear in the vorticity transport equation, since the same factor is generated by the convective terms as well as the Laplacian.

*The function Ψ is not identical for the two coordinate systems. The dependence of the function on the coordinate system is implied by the subscripts on the Laplacian operator.

Equations (22)-(25), (29), (30), (37), and (38) represent the final working relationships necessary to solve this problem. It is apparent, however, that the boundary conditions apply to an infinite strip. In order to reduce the problem to a more manageable size for the available digital computer, it is necessary to place constraints on the ends of this strip. At the upstream boundary located a distance of about $5\underline{r}$ from the origin, the conditions of $\underline{v} = 0$ and $\underline{u} = U_\infty$ were applied. For the lower boundary of the same distance downstream, the condition that $\partial\Psi/\partial X = 0$ was applied. This latter condition is truly an approximation and imposes an unreal restriction on the solution, especially at high Reynolds numbers.

The solution then proceeds from grid point to grid point in the η direction and the ζ in the same manner one reads a book. Both the vorticity field and the stream function field are solved simultaneously until the solution has converged.

CONVERGENCE AND STABILITY

The criterion of convergence is of the form similar to that of Fromm (17). Each grid point, $\underline{i},\underline{j}$, must eventually converge to a single value in each of the fields Ψ and Ω. Defining $\underline{n}$ for the moment to be the $\underline{n}$th iteration step and Ψ_{ref} and Ω_{ref} to be reference values, the criterion for convergence is

$$\frac{|\Psi_{i,j}^{(n)} - \Psi_{i,j}^{(n-1)}|}{\Psi_{ref}} \leqslant 0.0001 \qquad (39)$$

and

$$\frac{|\Omega_{i,j}^{(n)} - \Omega_{i,j}^{(n-1)}|}{\Omega_{ref}} \leqslant 0.0001. \qquad (40)$$

The reference stream function was given a value of unity, while the reference vorticity was given a value of 2. The solution is not completed until all of the grid points in both fields have converged according to the above criterion.

Thom (18) has reported that along the boundary of the cylinder and in the downstream wake at higher Reynolds number, the vorticity values will begin to oscillate. This oscillation is a peculiarity of the numerical method and not of the differential equations. In order to alleviate this problem, a modified value $\Omega_{\underline{ij},\underline{b}}^{(\underline{n})}$ is computed from the first value $\Omega_{\underline{ij},\underline{a}}^{(\underline{n})}$ and the previous value $\Omega_{\underline{ij},\underline{b}}^{(\underline{n-1})}$ according to the following equation

$$\Omega_{ij,b}^{(n)} = \Omega_{ij,b}^{(n-1)} + k\left(\Omega_{ij,a}^{(n)} - \Omega_{ij,b}^{(n-1)}\right). \tag{41}$$

A value of $\underline{k} = 1/2$ gave satisfactory results.

All of the numerical solutions were performed on an IBM system 360-40 (64K memory) with the average solution requiring about 30 minutes of computer time.

METHODS OF TESTING SOLUTIONS

Lapidus (25), Collatz (26), Forsythe and Wasow (27), and Greenspan (22) all have, in their discussions on finite difference methods, indicated that these systems of equations do not have unique solutions. However, it is possible to obtain a reasonable quantitative solution whose accuracy is not very great, but often suffices for many problems. Collatz sums up the warning given by many authors when he stated:

> ....that formal calculations applied to partial differential equations can lead to false results very easily and that approximate methods can converge in a disarmingly innocuous manner to values bearing no relation to the correct value.

The conclusion to be drawn from these thoughts is that the numerical solution should be compared with known information regarding the problem before judging the solution to be valid and reasonable.

There are several criteria which may be used to judge the numerical results. One is the mapping of the stream function and vorticity fields. The others

include vortex length, pressure distribution around the surface of the cylinder, the wall shear stress distribution, and the drag coefficient from a macroscopic momentum balance. All of these criteria will be discussed and their results presented except for the drag coefficients. The data for the drag coefficients will be presented in the Results Section, along with the experimental data.

The stream function pictures or maps are probably the most helpful means of determining the validity of the whole solution. They may be compared with maps from other solutions and with experimental photographs of the fluid in similar problems. Figures 4 and 5 are computer-drawn pictures of the vorticity and stream function fields at $\underline{Re}$ = 10 and 40, respectively. The flow proceeds from left to right with the stream function in the upper half of each frame and the vorticity field in the lower half of the frame*. The irregularities of the -0.6 vorticity line is not a real phenomenon, but appears to be due to the constraint placed at this downstream boundary. The slight distortion in many of the lines near the midpoint of the fields is believed to be the result of a peculiarity in the complex potential [Equation (32)].

These maps, however, compare very reasonably with those of an isolated cylinder published in the literature (13, 14, 18, 20, 21). The differences between these pictures and those of the isolated cylinder demonstrate the confining effect on the flow downstream of the cylinder due to the adjacent cylinders. The apparent point of separation, as indicated by the zero streamline, for $\underline{Re}$ = 40 is about 126 degrees from the leading stagnation point. This compares with 131 degrees and 132 degrees for isolated cylinders given by Batchelor and Kawaguti, respectively, for the same Reynolds numbers ($\underline{Re}$ = 40).

*These vorticity maps are mirror images of the upper half of the frames, thus the negative values.

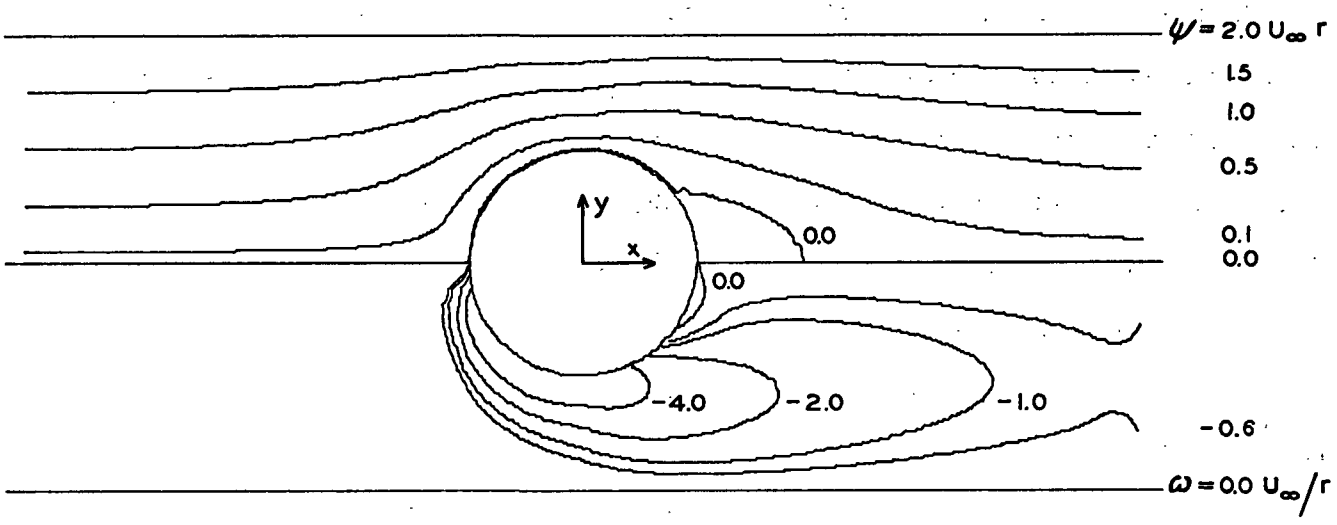

Figure 4. Stream Function (Upper Half) and Vorticity (Lower Half) for Parallel Array of Cylinders. Re = 10

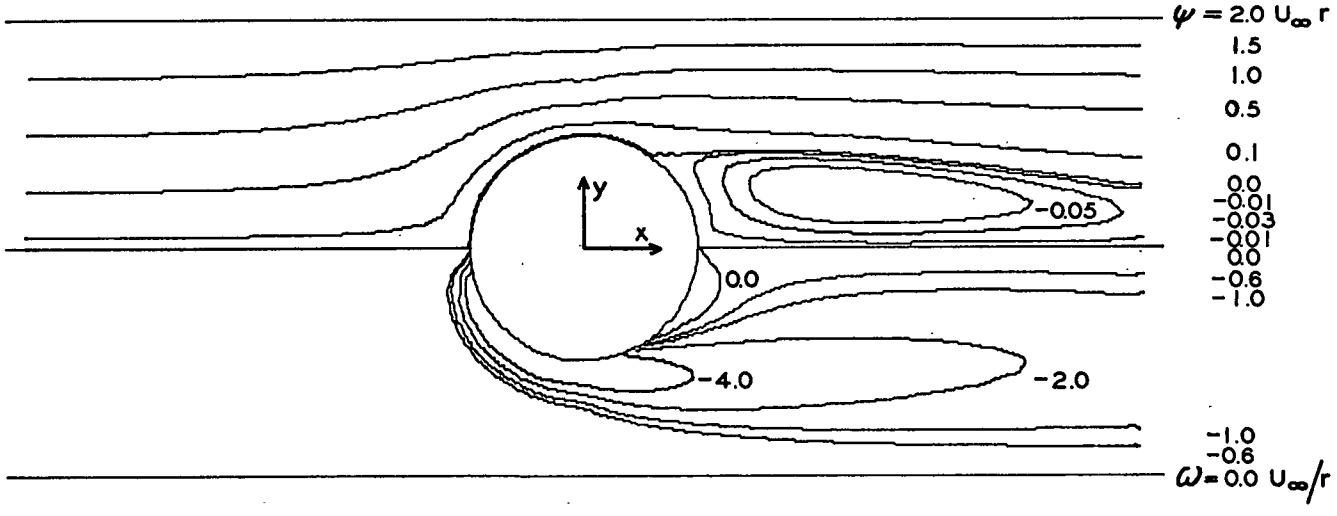

Figure 5. Stream Function (Upper Half) and Vorticity (Lower Half) for Parallel Array of Cylinders. Re = 40

Another criterion for judging the validity of these solutions is the length of the vortex behind the cylinder. Taneda (28) measured this length from photographs of standing eddies behind an isolated cylinder. His results are presented in Fig. 6, where the ratio of vortex length, s, to cylinder diameter, $2R$, is plotted against the Reynolds number. The length of the vortex from the numerical solution is similarly plotted in Fig. 6. There is no vortex for $Re = 2$, and the vortex for $Re = 40$ and 60 has extended beyond the boundary of the problem (the maximum $s/2R$ ratio that can be obtained from these solutions is 1.9). Although there are only two data points for comparison, their trend is consistent with that of isolated cylinders. The longer vortex would be expected for the cylinder in the array, since the velocity is greater in the neighborhood of the cylinder than it would be for the isolated cylinder at the same Reynolds number. This higher velocity is due to the presence of the adjacent cylinders.

PRESSURE DISTRIBUTION

Another criterion for judging the numerical solution is the pressure distribution around the surface of the cylinder. The pressure at any point in the field may be computed from the stream function and vorticity fields. Starting with the Navier-Stokes equations (7) and (8), it is possible (19) to solve for the pressure in the transformed coordinate system. Proceeding along a potential flow streamline (ζ direction) from Point 1 to Point 2, the dimensionless pressure, $P/1/2\rho U_\infty^2$, is

$$P_2/\tfrac{1}{2}\rho U_\infty^2 = P_1/\tfrac{1}{2}\rho U_\infty^2 + (Q_1^2 - Q_2^2) - \int_1^2 \Omega \frac{\partial \Psi}{\partial \zeta} d\zeta - \frac{2}{Re} \int_1^2 \frac{\partial \Omega}{\partial \eta} d\zeta \qquad (42)$$

where Q^2 is the dimensionless magnitude of the velocity vector. The integrals were crudely approximated with summations. At $X = -5R$, P_1 was assumed to be zero, and Q_1 is unity. Since the zero streamline is used, the first integral is zero and along the surface of the cylinder *per se*, the velocity is zero. Equation (42) is

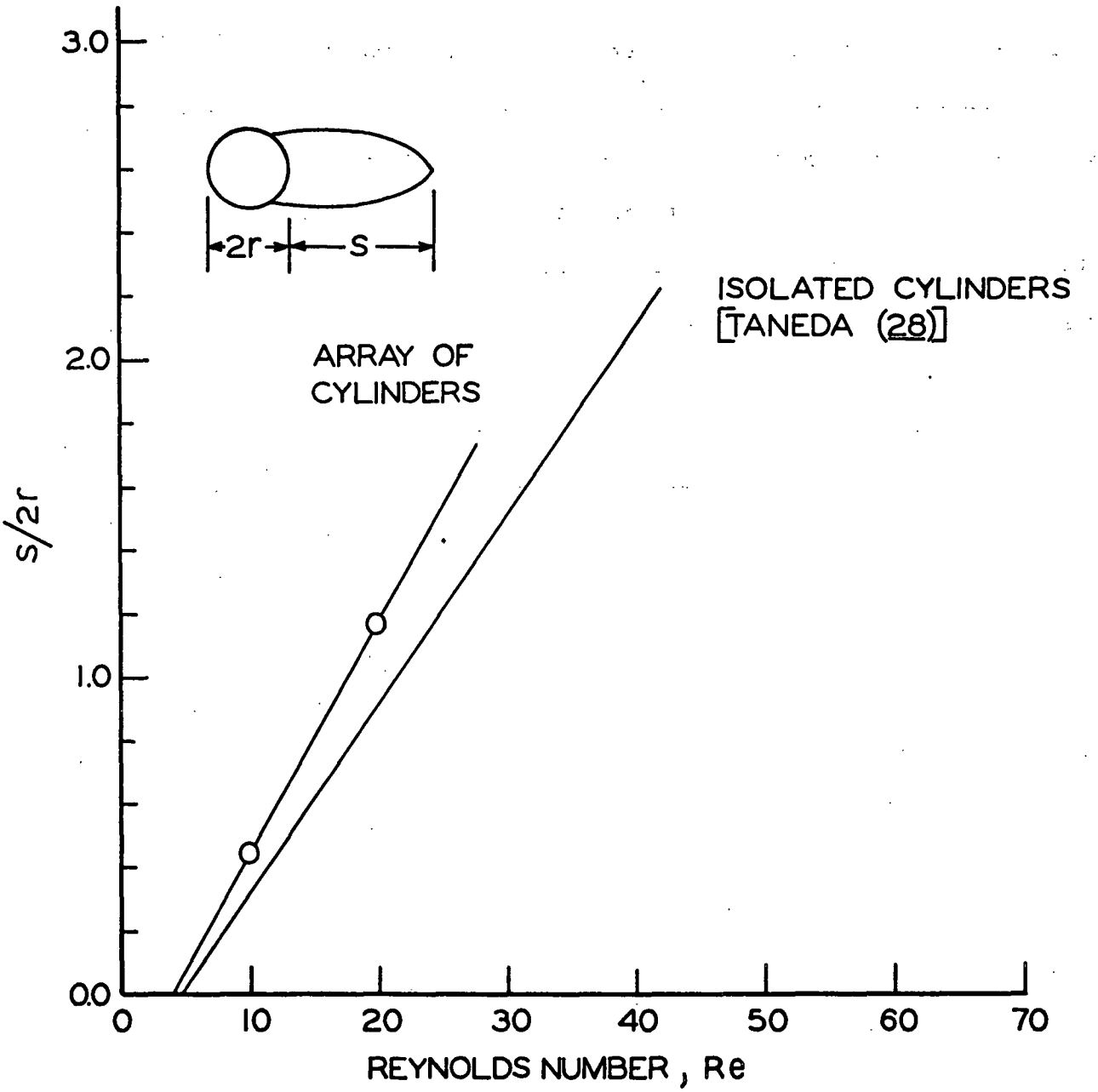

Figure 6. Vortex Length vs. Reynolds Number

then

$$P_2/\tfrac{1}{2}\rho U_\infty^2 = 1. - Q_2^2 - \frac{2}{Re} \sum \frac{\partial \Omega}{\partial \eta} \Delta\zeta \ . \qquad (43)$$

Figure 7 is a plot of the pressure distribution around the surface of the cylinders in the array. Here again, the distribution is basically right; however, the accuracy is not very good. The ideal flow case gives a curve which is symmetrical about the 90-degree point, and reaches a minimum value of -6.25. The distortions in the curve at about 18 degrees and 162 degrees are a consequence of the grid point distribution on the cylinder surface. These are the first grid points from either end, after which the increment reduces to about 4 degrees. These pressure distributions are not symmetrical about the midpoint of the cylinder as they are for potential flow because of the presence of the vortex behind the cylinder.

SHEAR STRESSES

The shear-stress distribution is another means of comparing the numerical solution with other reported data. This wall shear stress may be obtained directly from the vorticity on the solid boundary. The shear stress, τ_{rs}, is defined as

$$\tau_{rs} = -\mu \frac{\partial U_s}{\partial r} \qquad (44)$$

where, for the moment, s is in the direction tangential to the contour of the cylinder, and r is in the direction of the normal to the contour. From Equation (11), defining vorticity, there results

$$\frac{\partial U_s}{\partial r} = \frac{\partial U_r}{\partial s} - \omega \qquad (45)$$

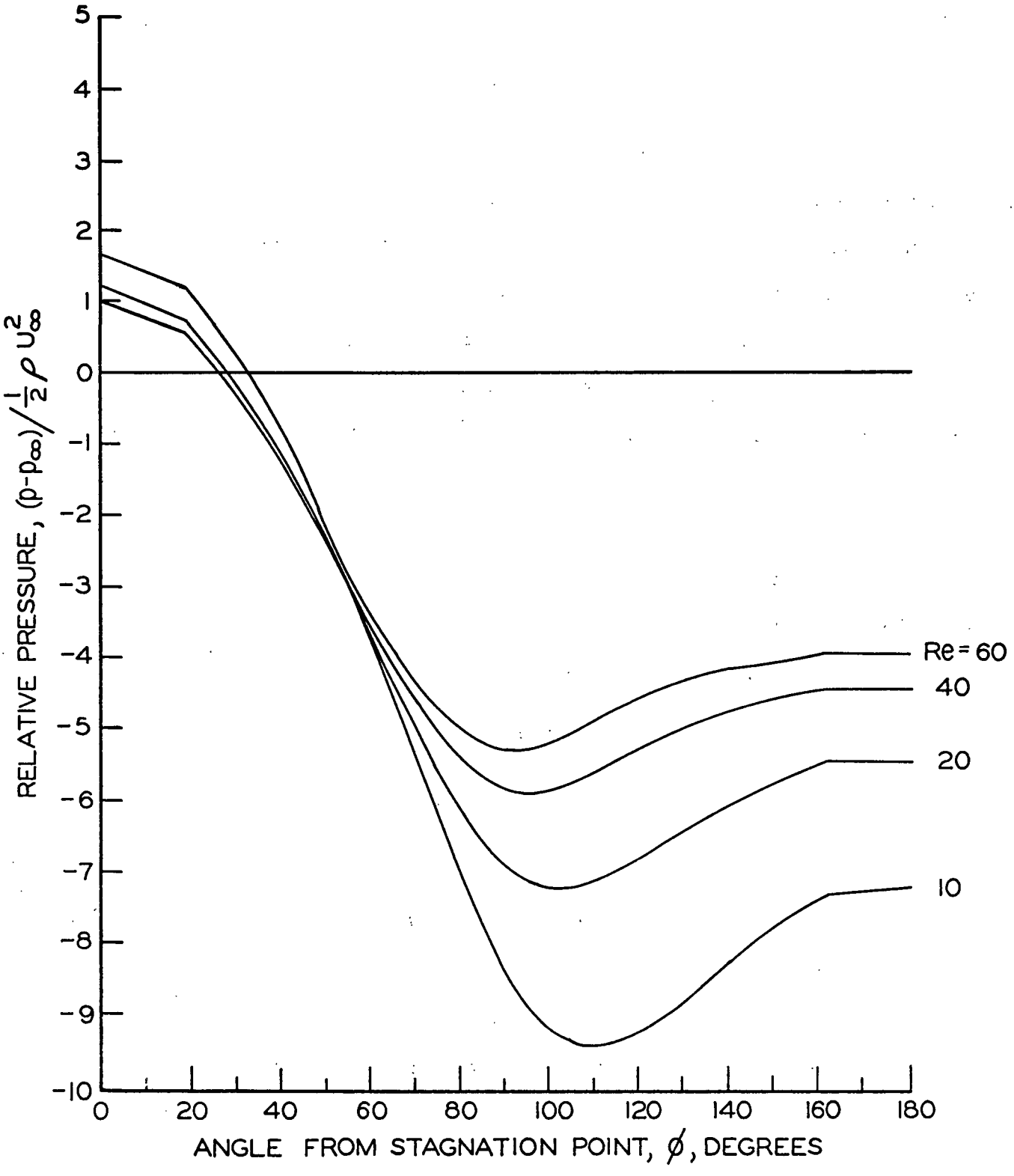

Figure 7. Pressure Distribution Around Surface of Cylinder in Parallel Array

At the wall $\partial U_r/\partial s = 0$ so that the wall shear stress is proportional to the wall vorticity

$$\tau_{rs} = \mu\omega \tag{46}$$

Figure 8 is a plot of the wall vorticity around a cylinder in the array. Again, these curves compare favorably with those in the literature (13, 20). The point of the boundary layer separation may be observed where the vorticity passes through zero. The point of the boundary layer separation is where the back flow and forward flow meet to form a stagnation point. At this point, $\partial U_r/\partial n = 0$. These curves again suffer from the consequences of rough approximations as evidenced by the distortion in the early stages of the development of the wall shear stress.

DRAG COEFFICIENTS

The final test for justifying the numerical results is the determination of the total drag, D, on the system. The drag coefficient, C_D, is a convenient method for expressing the drag and is here defined as

$$C_D = D/\tfrac{1}{2}\rho U_\infty^2 S'. \tag{47}$$

The characteristic area, S', for cylinders is defined as 2RL, where L is the length of the cylinders.

There are two methods for determining the drag or drag coefficient, each of which serves as a check on the other. One method involves breaking the total drag into two components; the "form drag" and the "skin friction." The other method is the macroscopic momentum balance over the entire system. Both methods will be discussed here.

The form drag portion of the total drag is the component, in the direction of motion, of the forces normal to the body or cylinder. This may be obtained through

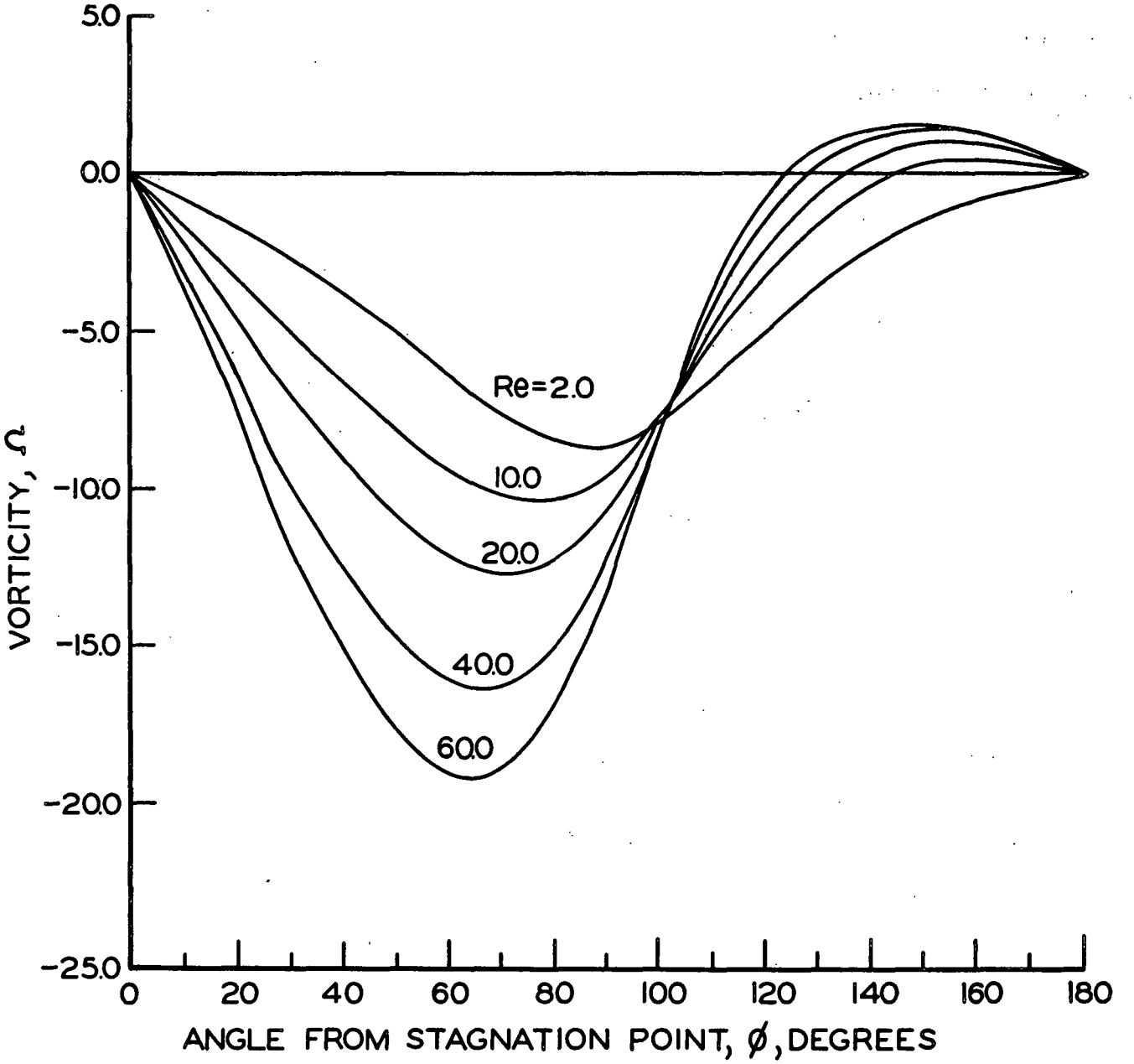

Figure 8. Shear Stress Distribution Around Surface of Cylinder in Parallel Array

the integration of the pressure distribution.

$$\text{Form Drag} = -2 \int_0^{\pi} p \cos\phi \, d\phi \tag{48}$$

where $\cos\phi$ is the direction cosine. The angle, ϕ, is measured from the leading stagnation streamline.

The skin friction is the component of the wall shear stress in the direction of motion. This may be determined from

$$\text{Skin Friction} = 2 \int_0^{\pi} \tau_{ns} \sin\phi \, d\phi. \tag{49}$$

The factor of two in each case accounts for the two halves of the cylinder. In this study, the integrals are replaced by simple summations (19) which was necessary because of limited memory capacity of the computer.

The momentum balance method for determining the drag coefficient is used to check the results from the method described. In later studies with the model, this method will prove useful. The momentum balance, strictly speaking, must be applied over the entire infinite strip from $x = -\infty$ to $x = +\infty$.

A method, however, was developed by Betz [13 (p. 616-18), 14, 29] for measurements made close to the body. The balance is made between Plane 1 upstream from the cylinder and Plane 3 downstream from the cylinder below the standing vortices. The total drag for the two-dimensional flow is then determined by

$$D = L \left\{ \int_{-\infty}^{+\infty} (G_1 - G_3) \, dy + \frac{\rho}{2} \int_{-\infty}^{+\infty} (U_1^2 - U_3^2) \, dy \right\} \tag{50}$$

where $\underline{G} = \underline{p} + \frac{1}{2}\rho\underline{U}^2$. The integration is performed over the total width of the field which, in this case, is $4\underline{R}$. The drag computed from Equation (50) is referred to as the "profile drag."

When applying the Betz method to this particular study, it is apparent that problems will arise as a result of the lower plane falling below the lower boundary of this study. If the lower boundary is considered as Plane 2, the pressure at Plane 3 may be obtained by a momentum balance between Planes 2 and 3, according to Equation (51)

$$p_3 = p_2 + \rho U_3(U_2 - U_3). \qquad (51)$$

The velocity at Plane 3 was assumed to be uniform and equal to the approach velocity. The drag may now be computed by Equation (51).

The drag coefficients, as computed by these two methods, will be presented in the Results Section where they may be discussed in conjunction with the experimental data.

APPROXIMATIONS FOR THE MAT-CYLINDER SYSTEM

Having developed the mathematical model for the parallel array of cylinders, it is of interest to model the combined mat-cylinder system. The description of the boundary conditions within a porous medium, however, cannot be strictly defined for use with the Navier-Stokes equation. Whitaker (30) has solved the equations of motion for porous media by neglecting the inertial terms and making various other approximations. His end result is the D'Arcy equation.

A means of modeling the mat-cylinder system, however, is to add terms to the Navier-Stokes equation which account for the effects of the porous medium. The D'Arcy equation, which describes the macroscopic flow properties in a porous medium, is given by

$$\nabla p = -\mu A' \vec{w} \qquad (52)$$

where $\nabla \underline{p}$ is the gradient of the pressure and $\underline{A}'$ is the specific resistance which

is the inverse of the permeability of the porous medium. The velocity, $\vec{w}$, is a mean flow rate. In order to incorporate this term into the Navier-Stokes equation, it is necessary to assume that the velocities and pressure are superficial quantities averaged over a small region of space, which is small with respect to the macroscopic dimensions of the flow system, but large with respect to the macroscopic dimensions of the porous medium. Incorporation of the D'Arcy equation into the Navier-Stokes equation permits one to define macroscopic boundary conditions (i.e., the surface of the cylinder), which affect the flow in the porous medium. Brinkman (31) discusses this development and compares his results with experimental results for flow through packed columns.

Having included the D'Arcy equation in the equation of motion,* one may obtain a vorticity transport equation in the same manner as described on page 10. The result for the steady state case is

$$\nu\nabla^2\omega - \nu A'\omega = u\frac{\partial\omega}{\partial x} + v\frac{\partial\omega}{\partial y} \quad (53)$$

A straight bridging porous medium resting on the parallel array of cylinders is defined in the problem. The finite difference form of Equation (53) is then applied to the mesh points which fall within the boundaries of the porous medium. Outside of the porous medium the specific resistance is zero and the finite difference form of Equation (53) reduces to Equations (29) and (30). Where the boundaries of the porous medium are straight lines in the $\underline{z}$ plane, they become curved lines in the ξ plane. This will result in a mat boundary which may be crudely represented.

*The modified equation of motion is

$$\frac{\partial\vec{w}}{\partial T} + (\vec{w}\cdot\nabla)\vec{w} = \frac{1}{\rho}\left[-\nabla p + \rho\vec{g} - \mu A'\vec{w} + \mu\nabla^2\vec{w}\right].$$

The solution of the model mat-cylinder system proceeds in the same manner as described for the parallel array of cylinders. The results from these solutions will be presented and discussed in conjunction with the experimental program.

EXPERIMENTAL

DESCRIPTION OF APPARATUS

A pipe loop was constructed for the purpose of obtaining the pressure drop-velocity data across the simulated mat-wire system. The loop is shown schematically in Fig. 9. A close-up drawing of the actual test zone and the simulated mat-wire system is shown in Fig. 10.

The pipe loop is here described in terms of its components. A 12-inch diameter circular header (B) is equipped with a cooling coil for fluid temperature control. The fluid proceeds downward through 9½-inch diameter circular Lucite pipe and through the flow evening screens (C). Each of the screens is of a different mesh, varying from 4 to 40 (9). The fluid enters the test section (D) where the portion near the wall is separated from the main flow by the test zone proper (see Fig. 10). The main flow passes through the mat-wire system and orifice plate (G) and on to the variable speed pump (I). The diverted flow passes through another orifice plate and joins the main flow at the variable speed pump (I). The fluid is then returned to the cooling header. A bypass (K) around the test zone is available to provide a finer adjustment of flow through the test zone. A 100-gallon tank (M) is used for surge control and filling of the pipe loop. Internal pressure leads pass from the 6-inch diameter test zone through bulkhead fittings (E) to the outside. A thermometer (F) indicates the temperature of the main flow. All of the piping is either polyvinyl chloride or clear acrylate.

The test section is shown as a scaled drawing in Fig. 10. The wall of the main 9½-inch pipe is depicted as (N) and the wall of the test zone proper by (P). An entrance nozzle (Q) for the test zone was machined to provide an acceleration of the fluid into the test zone. Thus, the boundary layer thickness occurring

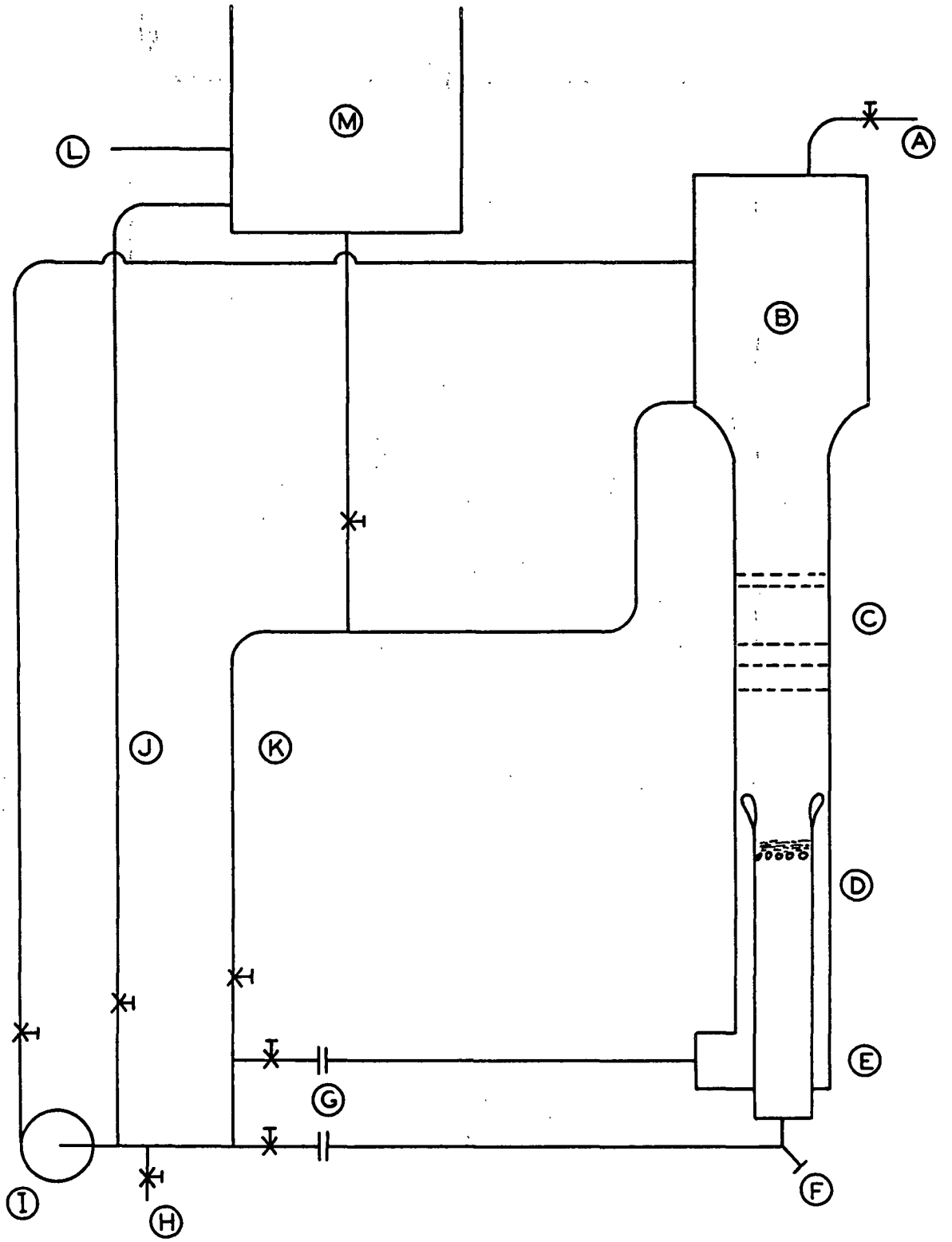

Figure 9. Schematic Diagram of Pipe Loop

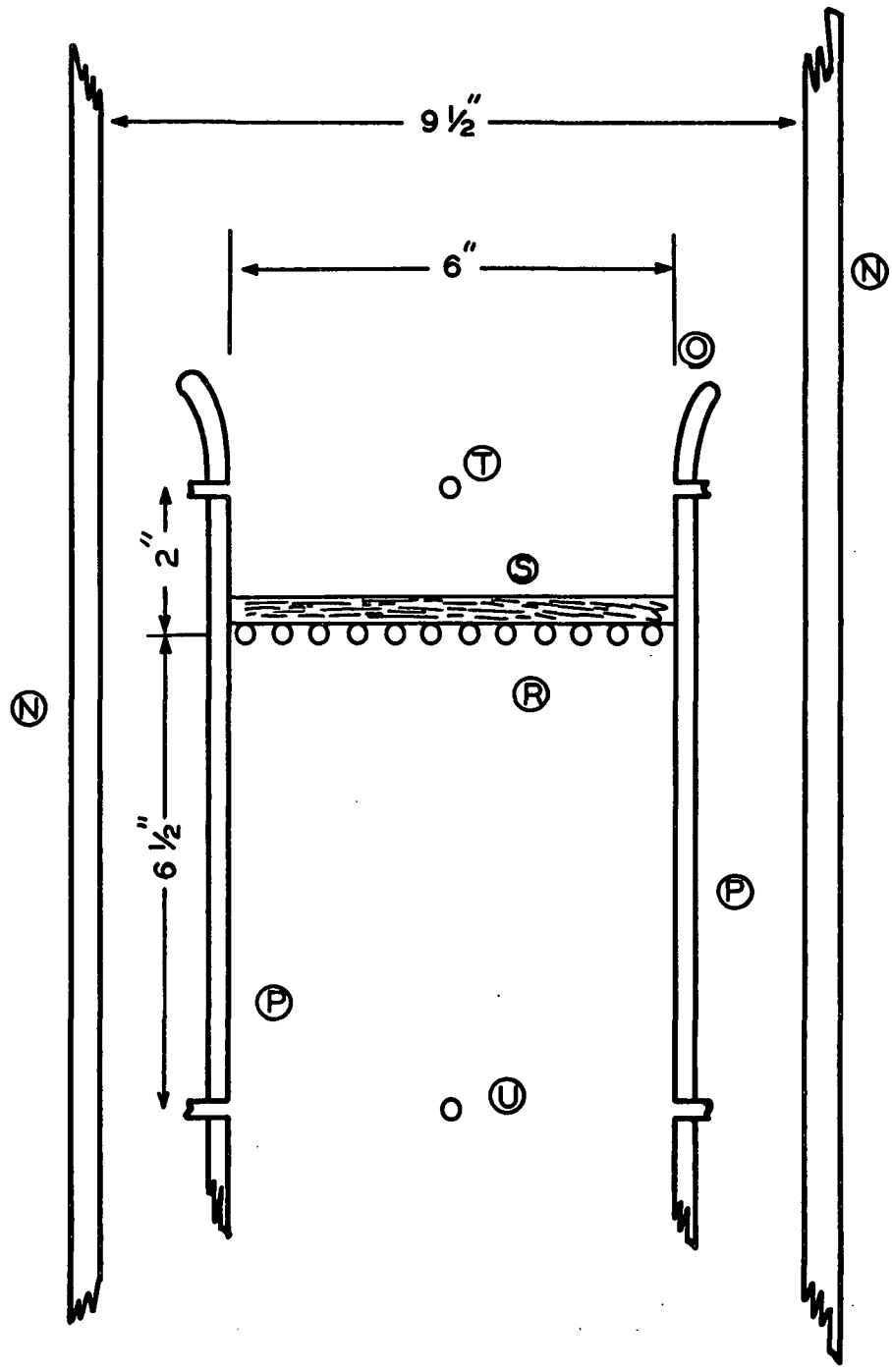

Figure 10. Transverse Section of Test Zone

along the wall of the test zone would be reduced and, as a result, a flatter velocity profile across the test zone could be obtained.

The parallel array of cylinders (R) and a few layers of screens (S) are depicted in the test zone. The static pressure taps (T, U) for obtaining the pressure drop across the simulated mat-wire system are also shown.

SIMULATED MAT AND WIRE

The simulated wire is composed of a parallel array of ¼-inch diameter brass rods with centers spaced ½ inch apart. The entire array is mounted in a 6-inch diameter mild steel ring which joins the 6-inch test pipe with shouldered joints. The upper portion of the test zone and entrance nozzle are fitted in the same fashion onto the steel ring.

The simulated mats were constructed of layers of wire screen. The layers were rotated in such a manner that the wire components of one layer are 45 degrees to the wires of the adjacent layer. This was done to eliminate large channels through the composite structure. The sets of mats were built to represent fiber mats of different porosity. Both sets of mats were made with plain weave phosphor bronze wire screens. Set A was constructed of 6 by 6-mesh screen with 0.027-inch diameter wires, whereas Set B employed 9 by 9-mesh screen with 0.035-inch wires. The physical dimensions and properties of the two sets of mats are given in Table I.

In order to assure reproducible conditions, a mat for each thickness was prepared and then tied with 0.001-inch diameter stainless steel wire. The tie wires are fine enough to contribute negligibly to the resistance of the mat and yet there are enough of them to provide a rigid structure.

The fluid used in this study was a synthetic oil called INDOPOL-L-10 polymer, manufactured by Amoco Chemical Company, Chicago. According to the manufacturer,

this oil is a polyisobutylene polymer with a molecular weight of about 300. In order to confirm Newtonian characteristics, a sample of the oil was placed in a calibrated Ferranti-Shirley plate-cone viscometer. A shear stress--shear rate line was obtained to a maximum shear rate of 16,000 $sec.^{-1}$. No indication of non-Newtonian characteristics were observed.

TABLE I

PHYSICAL PROPERTIES OF WIRE MESH SCREENS AND MATS

Wire Screens

	Mesh	
	6 by 6	9 by 9
Diameter of warp, $\underline{d}_w$, inches	0.027	0.035
Diameter of shute, $\underline{d}_s$, inches	0.028	0.035
Number of warp wires/inch, $\underline{n}_w$	5.98	9.2
Calculated specific surface, $\underline{S}$, per unit volume of solid wires, $cm.^2/cm.^3$	57.24	44.96

Mats Prepared from Wire Screens

	Thickness, cm.		Calculated Porosity	
Number of Layers	6 by 6	9 by 9	6 by 6	9 by 9
1	0.1346	0.212	0.8646	0.774
2	0.2667	0.3937	0.8633	0.7566
3	--	0.6096	--	0.7642
4	0.5359	0.8179	0.8639	0.7657
6	0.8026	--	0.8637	--
8	1.064	--	0.8630	--

A viscosity-temperature curve was then determined and fitted to a third-order polynomial equation for computational use. Similarly, a density-temperature curve was obtained. These data are presented in Appendix II.

PRESSURE MEASURING SYSTEM

The pressure differential for the orifice meter was measured with an inverted air over fluid U-type manometer. The air pressure in the manometer could be adjusted to put the manometer into the proper range. A description of the system and calibration procedure are presented in Appendix I.

The measurement of pressure drops across the mat-wire models was obtained with the use of a PACE pressure transducer (Pace Engineering, California). This is a variable reluctance device with interchangeable diaphragms. In most of the work in this study, the 10-cm. H_2O diaphragm (range is between -10-cm. H_2O and +10-cm. H_2O) was used, and occasionally the 100-cm. H_2O diaphragm was necessary. Output from the transducer indicator was then either displayed with a digital voltmeter or a recording potentiometer. In order to minimize the sensitivity of the transducer to pressure pulses emanating from the pump, it was desirable to use air rather than liquid in the cavities of the transducer. The volume of air remained small in order to minimize compressibility effects. Four pressure taps, 1/16-inch inside diameter, and connected to one another, were equally spaced in a plane around the circumference of the test zone in order to obtain average static pressures. The upstream taps were located two inches above the plane of the array of cylinders, while the downstream taps were six inches below the plane of the array. Details of the pressure measuring system and the calibration information are presented in Appendix II.

EXPERIMENTAL PROCEDURES

The sample (either the array of cylinders, mat, or both) is placed in the test zone. Referring to Fig. 9, the oil is drained from the surge tank (M) into the bottom of the pipe loop through a ½-inch pipe (J) until the level of the oil is above the flow evening screens (C), at which time the four-inch pipe from the tank

is opened for rapid filling. The air vent (A) is open during this period. When the loop is filled, the variable speed pump (I) is started and allowed to run for about five minutes. The pump is stopped and the entrapped air in the oil is then allowed to rise into the header (B). After a period of one-half to one hour, the air is vented and the pump started again. This procedure is repeated until there is no evidence of air bubbles in the oil. Usually three ventings were required. Air is also bled from all pressure measuring lines.

Before each run, the pressure transducer is checked against the calibrating manometer at several points over the range of the pressure transducer. In the case of the 100-cm. H_2O diaphragm, the calibration is checked only on the 0-50 portion of the range.

The pump is started and run at a low r.p.m. The pressure drop across the test sample, as measured by the transducer, is allowed to stabilize, usually for a period of one to two minutes. A check of the zero point on the transducer is made to assure there being no drift. The transducer reading, orifice manometer reading, and fluid temperature are then recorded. The pump speed is increased, and another set of data is obtained.

Some of the runs were performed at a constant fluid temperature of $23.0 \pm 0.2°C$. by adjustment of the flow of cooling water to the header, whereas with the remaining runs, the fluid temperature was allowed to change at will.

During the early runs with mat Set B (9 by 9 mesh), the data were obtained for the decreasing flow rate steps as well as the increasing flow rate steps. Since there were not any hysteresis effects observed, the decreasing flow rate steps were not performed with later samples.

At the conclusion of a run, the oil is drained into storage barrels and the test sample is removed. A small pump is used to transfer the oil to the 100-gallon tank prior to a run.

The orifice manometer readings are first converted to velocity units, while the transducer readings are converted to standard pressure units by means of a conversion equation presented in Appendix II. These pressure drop, ΔP, and velocity, U_∞, data are given in Appendix III.

RESULTS

EXPERIMENTAL

As was discussed in the introduction, the usual way of characterizing a fibrous mat and many porous media is through the use of the Forchheimer equation:

$$\Delta P = aU_\infty + bU_\infty^2. \qquad (1)$$

According to the defining equation for the coefficients, a and b, [Equations (2) and (3)], it is possible to rearrange the Forchheimer equation into the form

$$\Delta P/\mu U_\infty = A + BU_\infty/\nu \qquad (54)$$

where ν is the kinematic viscosity of fluid and where A will be called the viscous coefficient and B the inertial coefficient for the remainder of this study. This form of the equation simplifies the determination of the coefficients if the fluid properties are not held to an absolute constant.

If the experimental data for the parallel array of cylinders [referred to as the bare cylinders (BC)], the bare mat (BM), and the combined mat-cylinder system (C) all conform to Equation (54), then the Equation (4) defining the interaction may be broken down into two components: the viscous interaction, A_I, and the inertial interaction, B_I. These two terms may be defined in the following manner:

$$A_I = A_C - (A_{BC} + A_{BM}) \qquad (55)$$

and

$$B_I = B_C - (B_{BC} + B_{BM}). \qquad (56)$$

The experimental data for the parallel array of cylinders, plotted in accordance with the rearranged Forchheimer equation (54), are shown in Fig. 11. The line represents the least square error fit of the data. Similar graphs are made for

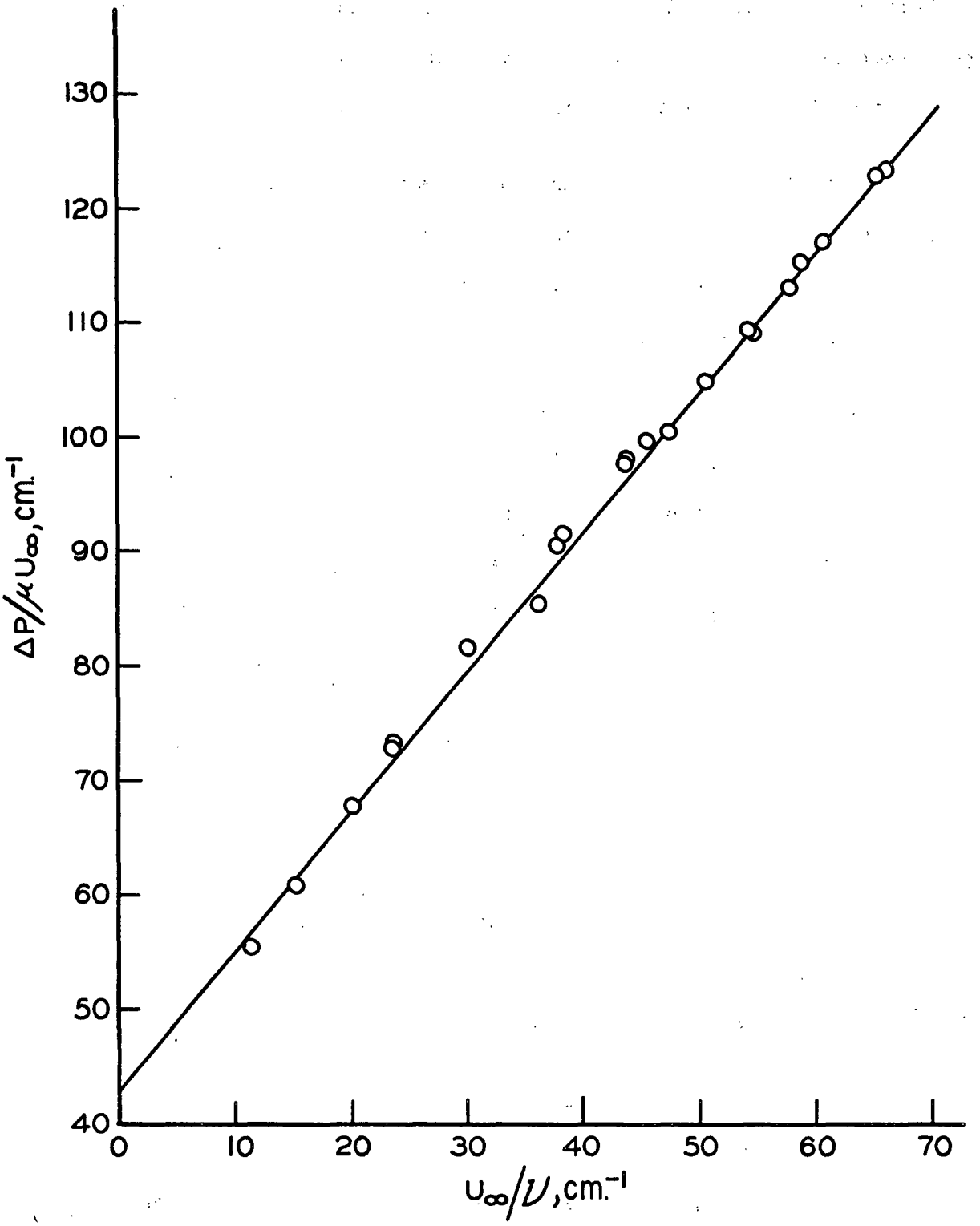

Figure 11. Bare Cylinder Data Plotted According to Modified Forchheimer Equation (54)

each of the bare mats and the combined mat-cylinder systems. A sample of the plot for the bare mat is presented in Fig. 12, and for a mat-cylinder combined in Fig. 13. A graphic example of the interaction, as defined by Equation (4), is shown in Fig. 13 where the dotted line represents the sum of the results from Fig. 12 and 13.

The coefficients A and B are computed for each sample and are summarized in Table II. The correlation coefficients from the least square error analysis are given for each sample in Appendix III. These viscous and inertial coefficients now form the primary data for analysis of the interaction phenomenon.

The precision of the viscous resistance term will vary from about ± 5% for the bare cylinder data to about 1% for the very thick mats and mat-cylinder results. The inertial coefficient is precise to about 3%. These are based on an estimate of the pressure measuring system error of about ± 50 dynes/cm.^{2}. The velocity is estimated to have an error of about 1%. The viscosity and density of the oil were spot checked over a period of one year and were found not to vary by more than 0.8%.

NUMERICAL

Data similar to that of the experimental program may be obtained from the mathematical model developed earlier. The results of the bare cylinder are presented and compared with the experimental data. Some data obtained from the literature are also compared with the results from this study. The results from the mat-cylinder model are also presented.

The drag coefficients, as determined by the skin friction--form drag method and the profile drag or momentum balance method, are plotted as a function of Reynolds number in Fig. 14. The experimental pressure drop measurements for the bare cylinders were converted to drag coefficients and are also presented in Fig. 14.

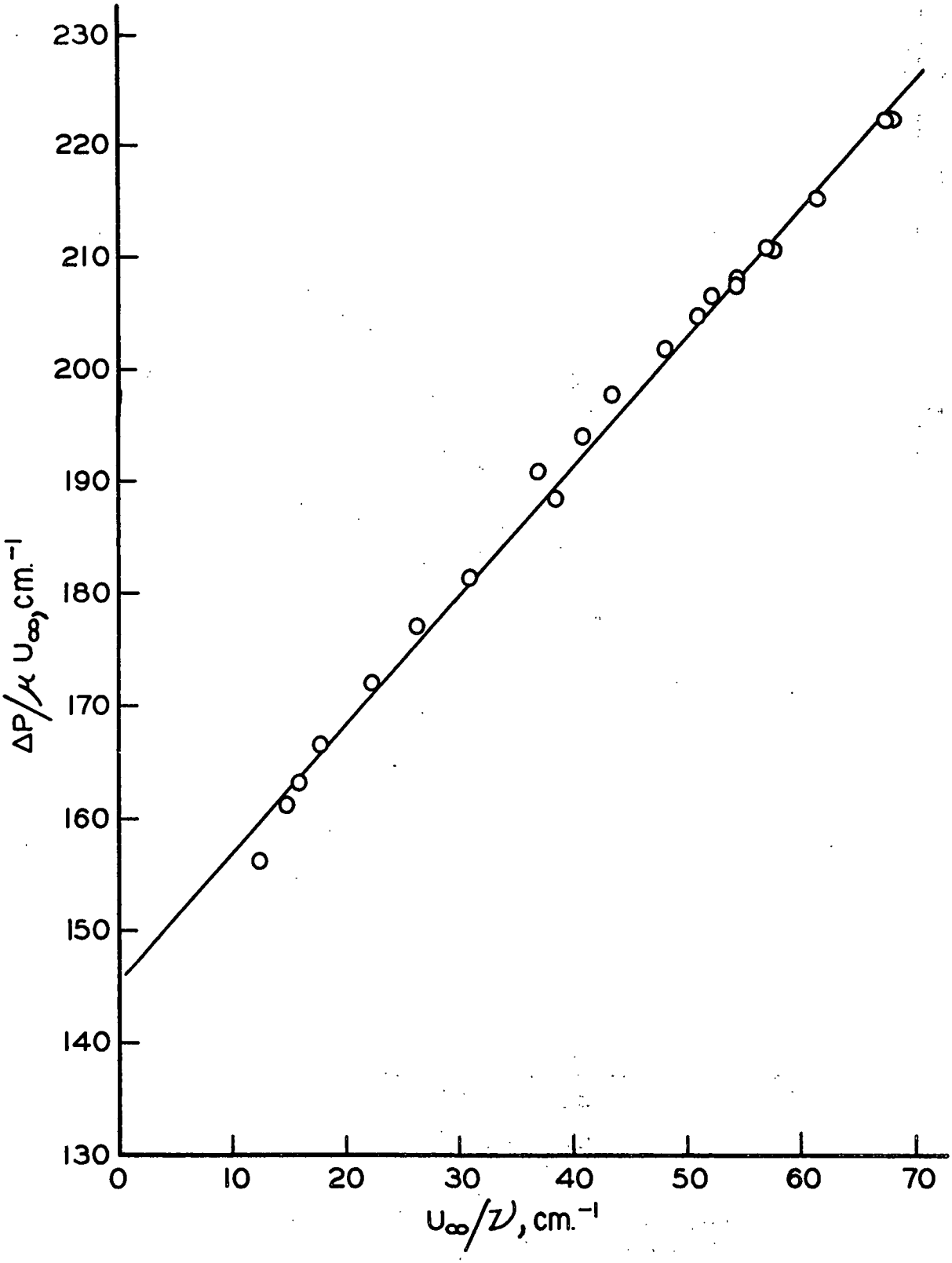

Figure 12. Bare Mat Data for $\underline{t}/\underline{r}$ = 0.84 (6 by 6-Mesh Mat). Plotted According to Modified Forchheimer Equation (54)

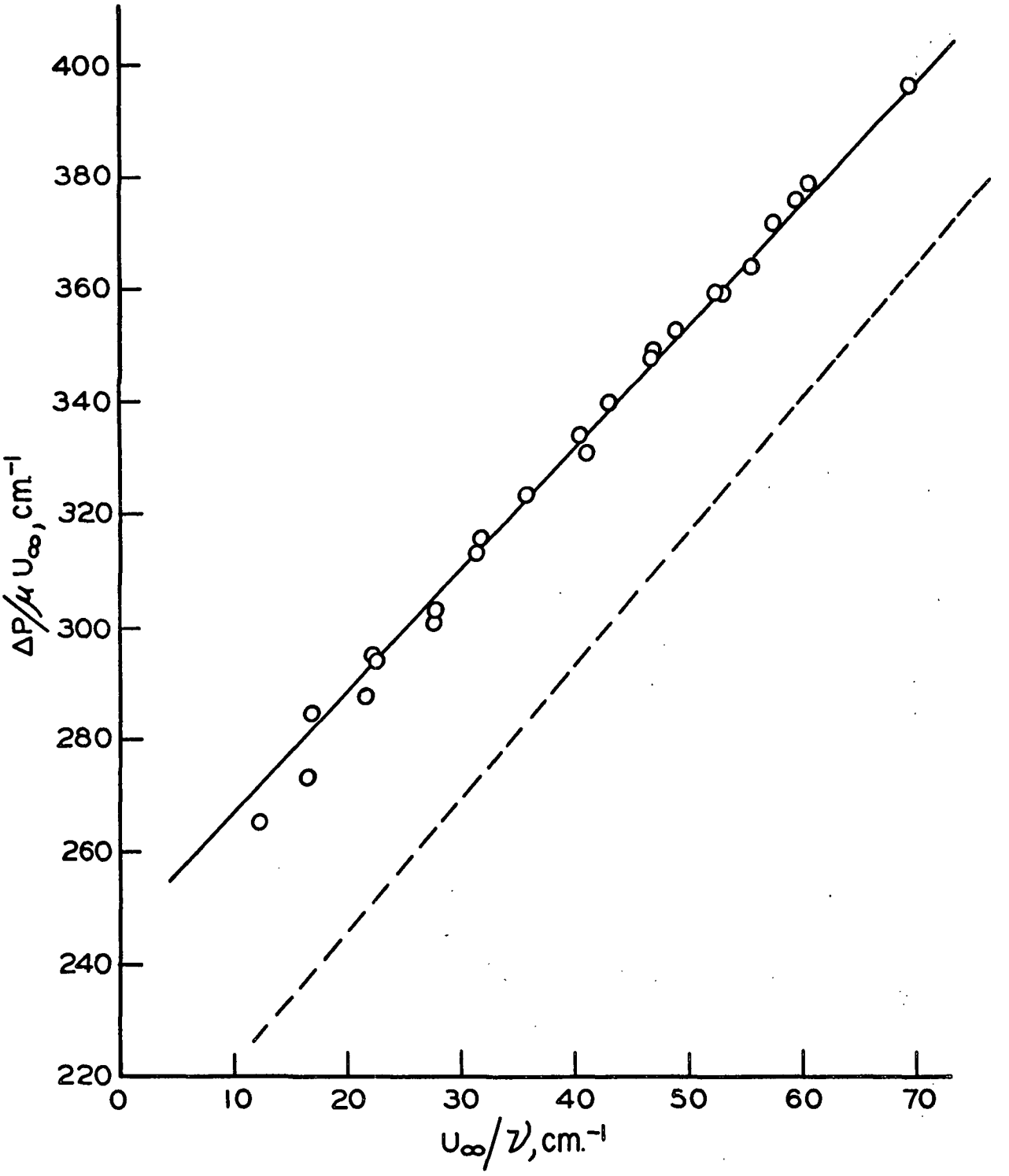

Figure 13. Mat-Cylinder Data for $\underline{t}/\underline{r}$ = 0.84 (6 by 6-Mesh Mats). Plotted According to Modified Forchheimer Equation (54). Dotted Line is Bare Mat Plus Bare Cylinders

TABLE II

EXPERIMENTALLY DETERMINED CONSTANTS FOR THE FORCHHEIMER EQUATION

Sample	6 by 6 Mesh		9 by 9 Mesh	
	$\underline{A}$, $cm.^{-1}$	B	$\underline{A}$, $cm.^{-1}$	B
Cylinders	42.99	1.215	42.99	1.215
Mats only				
1 layer	66.59	0.623	231.69	1.404
2 layers	145.48	1.159	468.39	2.793
3 layers	--	--	745.68	3.835
4 layers	303.61	1.820	1017.90	4.861
6 layers	461.79	2.521	--	--
8 layers	624.39	3.299	--	--
Mats and cylinders				
1 layer	148.28	1.759	319.23	2.446
2 layers	245.93	2.158	586.20	3.764
3 layers	--	--	845.33	4.889
4 layers	407.30	3.127	1080.81	6.773
6 layers	560.88	4.006	--	--
8 layers	729.64	4.578	--	--

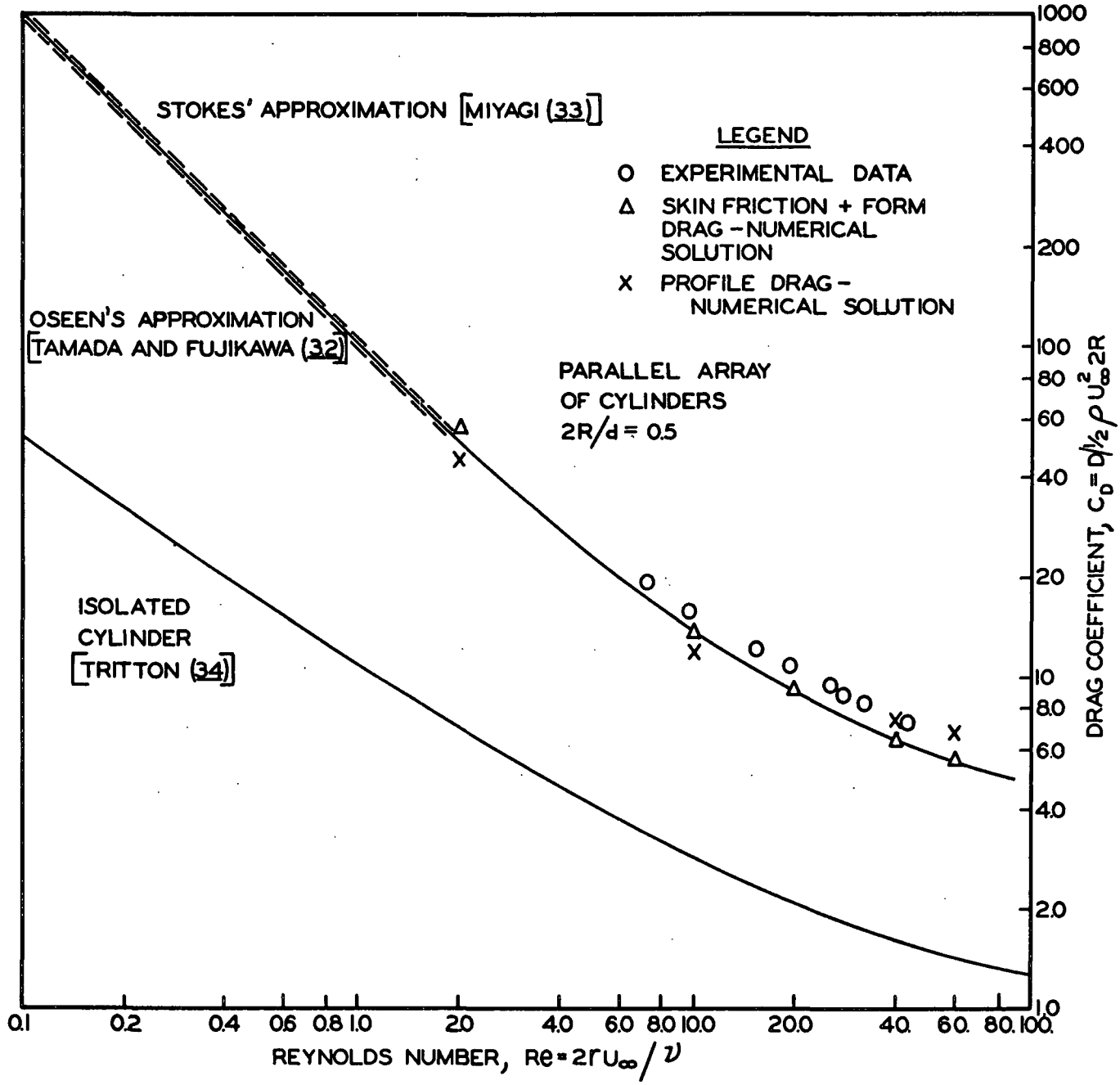

Figure 14. Drag Coefficients for Infinite Circular Cylinders vs. Reynolds Number

With regard to the numerical results, it is apparent that the drag coefficients, determined by the profile drag method, suffer from the effect of the standing vortex. This problem was noted in the discussion on the use of the profile drag method in this study. At the lower Reynolds number (Re = 2), there is the question of which of the two values for C_D is the most accurate.

A review of the literature reveals two independent studies made on a parallel array of cylinders at low Reynolds numbers. These results are presented to confirm the numerical solutions in this study.

Tamada and Fujikawa (32) employed Oseen's approximation to the equations of motion, so that

$$\rho U_\infty \frac{\partial \vec{w}}{\partial x} = -\nabla P + \mu \nabla^2 \vec{w}. \qquad (56a)$$

The arrays studied ranged in spacing ratio, $2R/d$, between 1/500 and 1/5 for Reynolds numbers below 8. Their results show that the drag per unit length of cylinder increases as the spacing ratio increases. For spacing ratios approaching unity, the viscous forces in the fluid are much greater than the inertial contribution as the fluid narrows down to pass between the cylinders. As a consequence, the drag is proportional to U_∞ for Reynolds numbers less than 5. As the spacing ratio becomes smaller the linear dependence on U_∞ is valid for only smaller and smaller Reynolds numbers until, at $2R/d = 0$, the drag on a cylinder becomes that of an infinitely isolated cylinder in an unbounded fluid. For the isolated cylinder at $Re < 1$ the drag is proportional to $U_\infty/\log(c/U_\infty)$, where c is a constant. Extrapolation of their results to $2R/d = \frac{1}{2}$ yields a value of $C_D = 96$ at $Re = 1$.

Similarly, Miyagi (33) employed Stokes' approximation for the array of cylinders so that the equation of motion becomes

$$\nabla P = \mu \nabla^2 \overline{w} \qquad (56b)$$

for $\underline{Re} < 1$. His solution for $2\underline{R}/\underline{d} = \frac{1}{2}$ yields a value of $\underline{C_D} = 105.6$ at $\underline{Re} = 1$.

These two results are shown in Fig. 14 as dotted lines. It would appear that these literature values confirm the numerical results of this study. The drag coefficient for an infinitely long, isolated cylinder in an unbounded fluid as obtained from Tritton (34) is also depicted.

There are several factors which must be considered in explaining the high experimental results. First is the effect of the circular cross section of the test zone on the array. Certainly the cylinders at either end of the array do not encounter the same conditions as the remainder of the array. In fact, the narrowed opening between the end cylinders and the wall of the test zone may choke off a higher proportion of the flow, thus slightly increasing the remainder of the flow in the zone. Also, despite the efforts made to keep the sample close to the entrance of the test zone, a boundary layer effect will be present causing a higher velocity past the major portion of the array as compared with the indicated volumetric mean velocity. Shair, et al. (35) indicate that the confining walls can significantly increase the drag on a cylinder.

The solid line, drawn through the data points in Fig. 14, is believed by this author to represent the information gathered here. The conclusion is that the mathematical model gives fairly good results in describing the flow through the array of cylinders.

The final results to be presented are those of the combined mat-cylinder system. The specific resistance coefficient, $\underline{A}'$, defined in the D'Arcy equation (52) is assumed to be equivalent to the viscous coefficient, $\underline{A}$, from the rearranged Forchheimer equation (54) for unit thickness (i.e., $\underline{A}' = \underline{A}/\underline{t}$). The

coefficients for the 9 by 9-mesh experimental mats were averaged to yield A' = 1190 cm.$^{-2}$, while those of the 6 by 6-mesh mats resulted in A' = 554 cm.$^{-2}$. The specific viscous resistance used in the mathematical model were 1190 cm.$^{-2}$ and 800 cm.$^{-2}$. Solutions were obtained for mat thickness ratios, t/r, of 0.5, 0.8, 1.5, and 3.0 and Reynolds numbers of 2, 10, 20, 40, and 60. The stream function-vorticity maps for the two series of mats are presented in Fig. 15-18 for t/r = 0.5 and Re = 10 and 40. The dotted lines represent the boundaries of the mat. These figures may be compared with those for the bare cylinder shown in Fig. 4 and 5.

The coefficients A and B for the rearranged Forchheimer equation may be obtained from the drag coefficients as determined by the profile drag or momentum balance method. These values are presented in Table III.

TABLE III

NUMERICALLY DETERMINED CONSTANTS FOR THE FORCHHEIMER EQUATION

Specific resistance	A' = 800 cm.$^{-2}$		A' = 1190 cm.$^{-2}$	
	A, cm.$^{-1}$	B	A, cm.$^{-1}$	B
Mat thickness, t/r				
Bare cylinders	31.6	1.312	31.6	1.312
Bare mat				
0.5	127	0.0	189	0.0
0.8	203	0.0	302	0.0
1.5	380	0.0	566	0.0
3.0	761	0.0	1132	0.0
Combined system				
0.5	251	0.967	352	0.884
0.8	355	1.055	504	1.062
1.5	539	1.709	779	2.055
3.0	886	2.972	1295	3.945

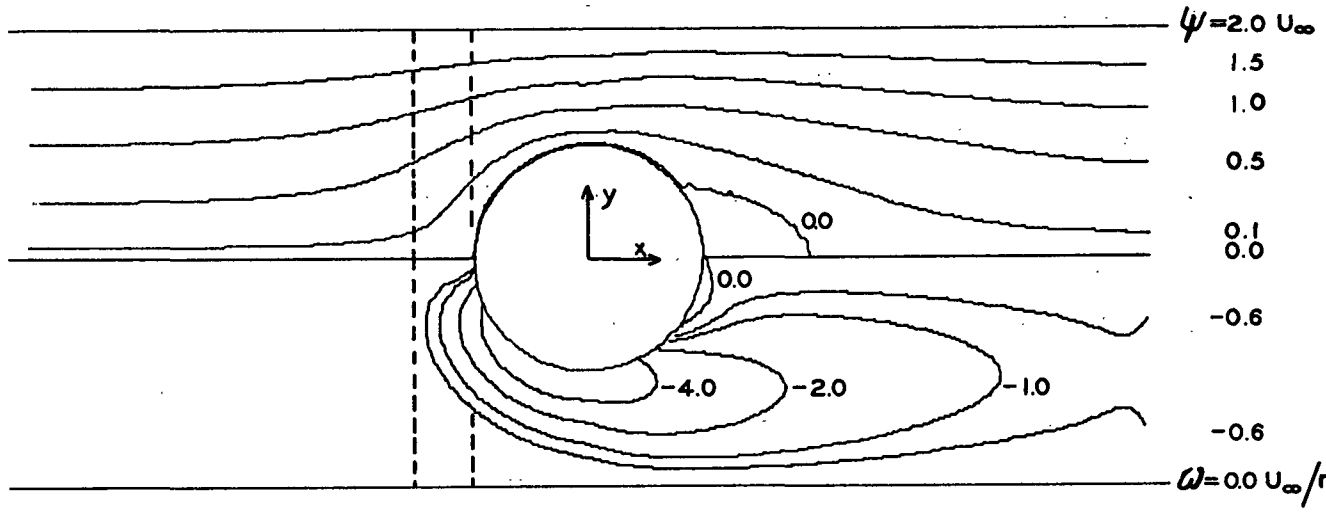

Figure 15. Stream Function (Upper Half) and Vorticity (Lower Half) for Mat on Parallel Array of Cylinders. Re = 10, t/r = 0.5, and A' = 800 cm.$^{-2}$

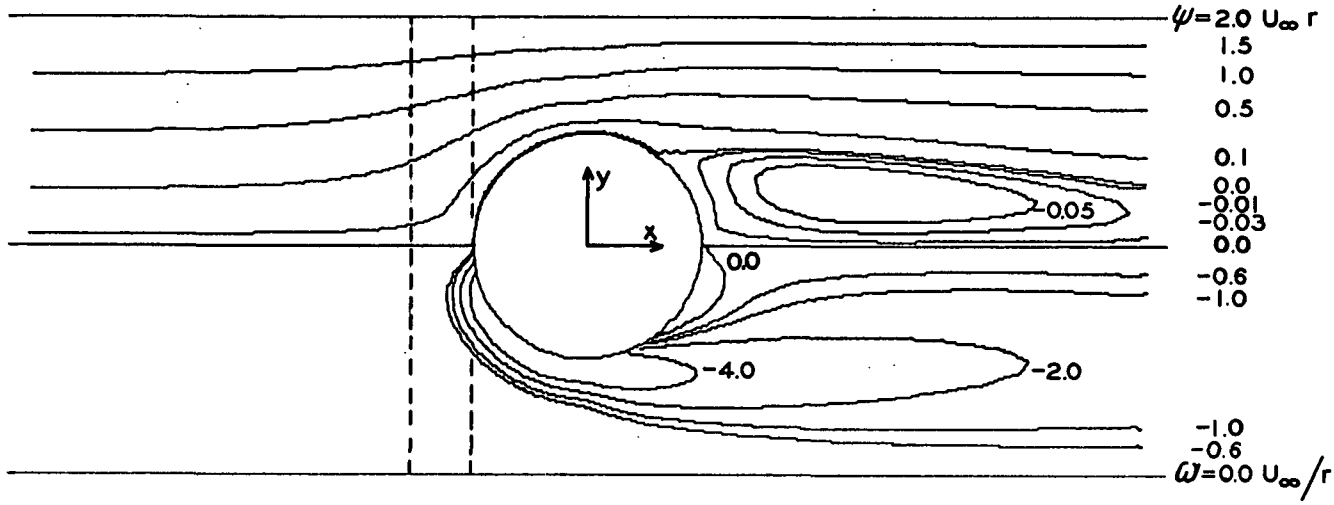

Figure 16. Stream Function (Upper Half) and Vorticity (Lower Half) for Mat on Parallel Array of Cylinders. Re = 40, t/r = 0.5, and A' = 800 cm.$^{-2}$

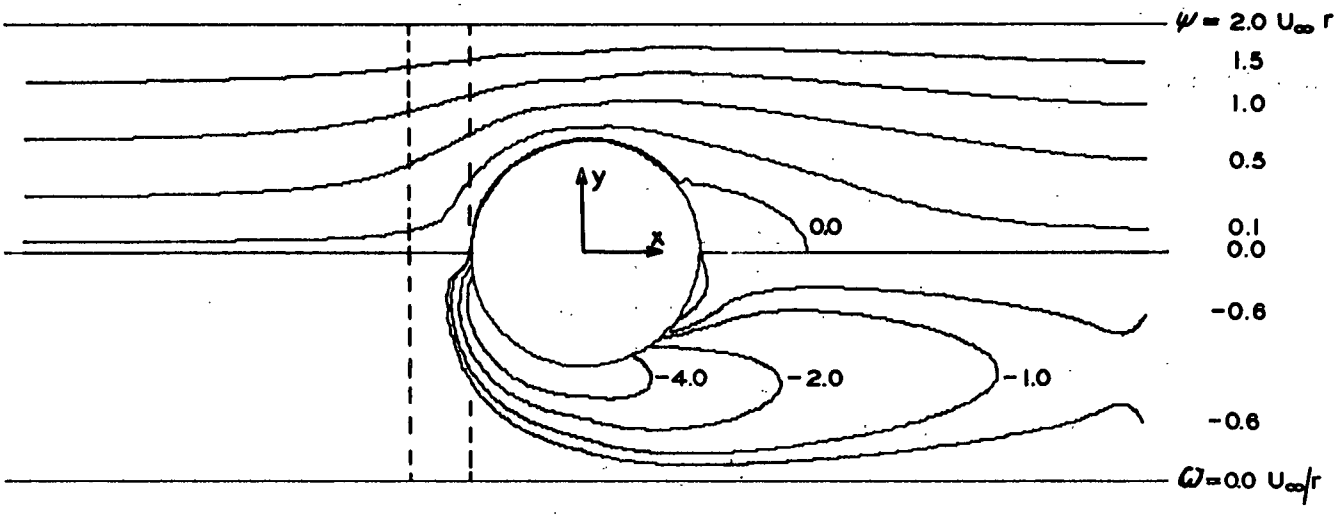

Figure 17. Stream Function (Upper Half) and Vorticity (Lower Half) for Mat on Parallel Array of Cylinders. Re = 10, t/r = 0.5, and A' = 1190 cm.$^{-2}$

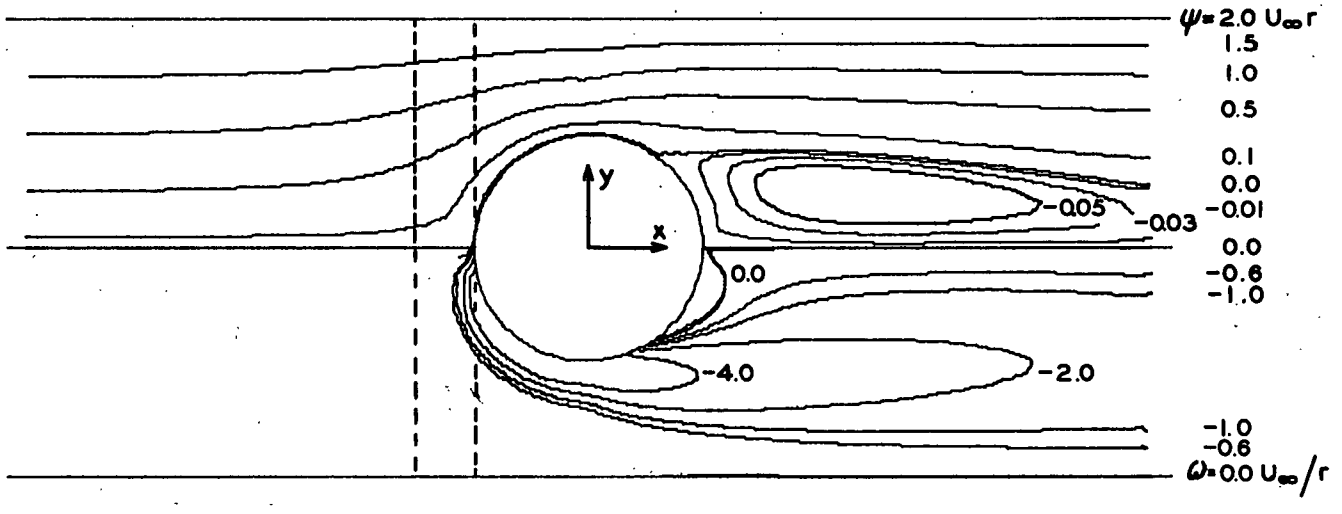

Figure 18. Stream Function (Upper Half) and Vorticity (Lower Half) for Mat on Parallel Array of Cylinders. Re = 40, t/r = 0.5, and A' = 1190 cm.$^{-2}$

The mathematical model has the advantage of looking at the resistance of the cylinders, with and without the presence of the mat. The drag coefficients are determined from the form drag--skin friction method. The viscous and inertial coefficients from these drag measurements are given in Table IV.

TABLE IV

FORCHHEIMER CONSTANTS FOR CYLINDERS

	A	B
Bare cylinders	40.5	0.971
Cylinders in presence of mat		
$\underline{A}' = 800$ cm.$^{-2}$	51.4	0.886
$\underline{A}' = 1190$ cm.$^{-2}$	52.7	0.873

Figure 19 summarizes the viscous interaction as defined by Equation (55) for both the experimental program and the mathematical model. Similarly, the inertial interaction, defined by Equation (56), is summarized in Fig. 20. The error in the experimental viscous interaction is about $\pm$ 20 cm.$^{-1}$ and in the experimental inertial interaction it is about $\pm$ 0.2.

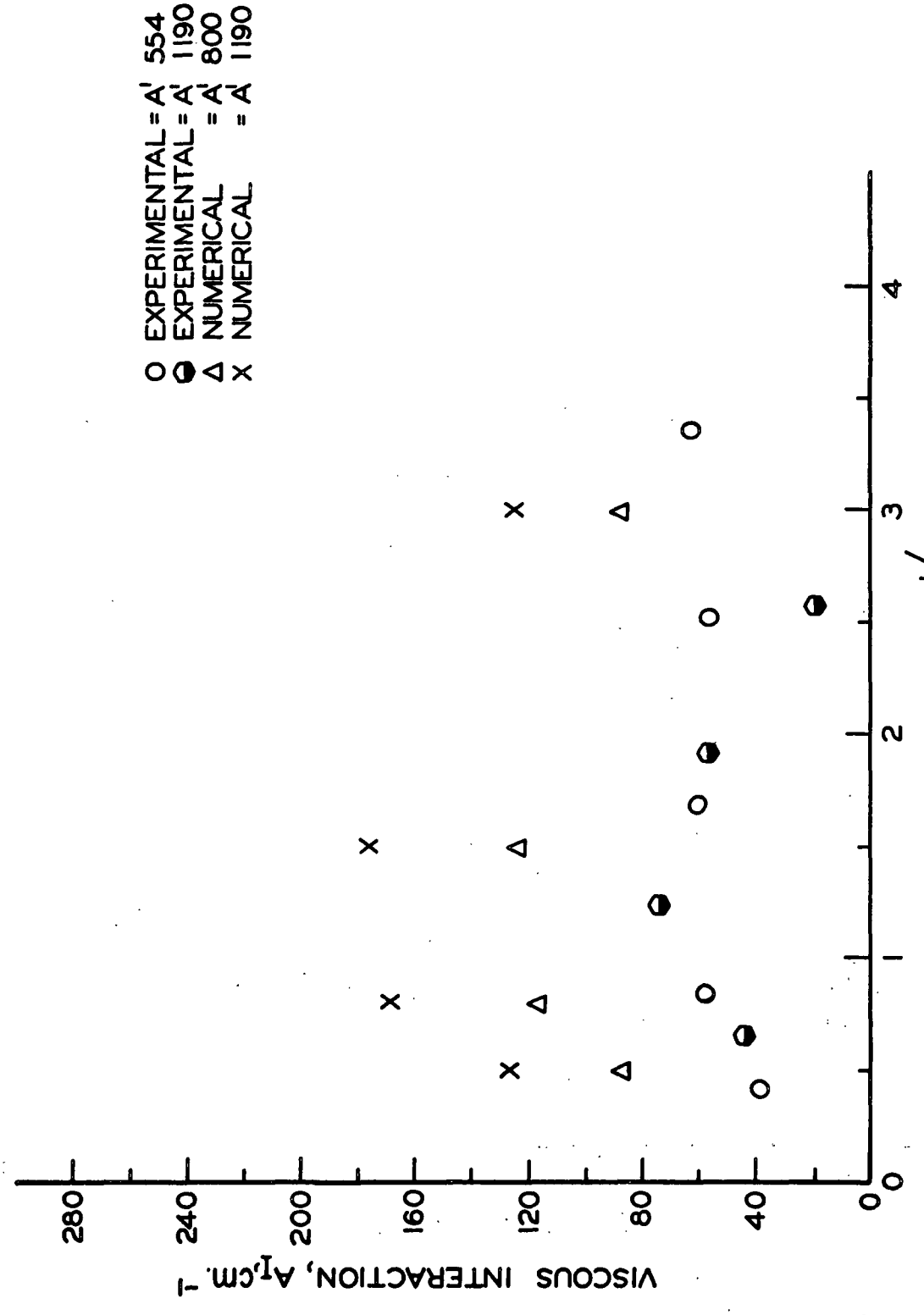

Figure 19. Viscous Interaction vs. Mat Thickness

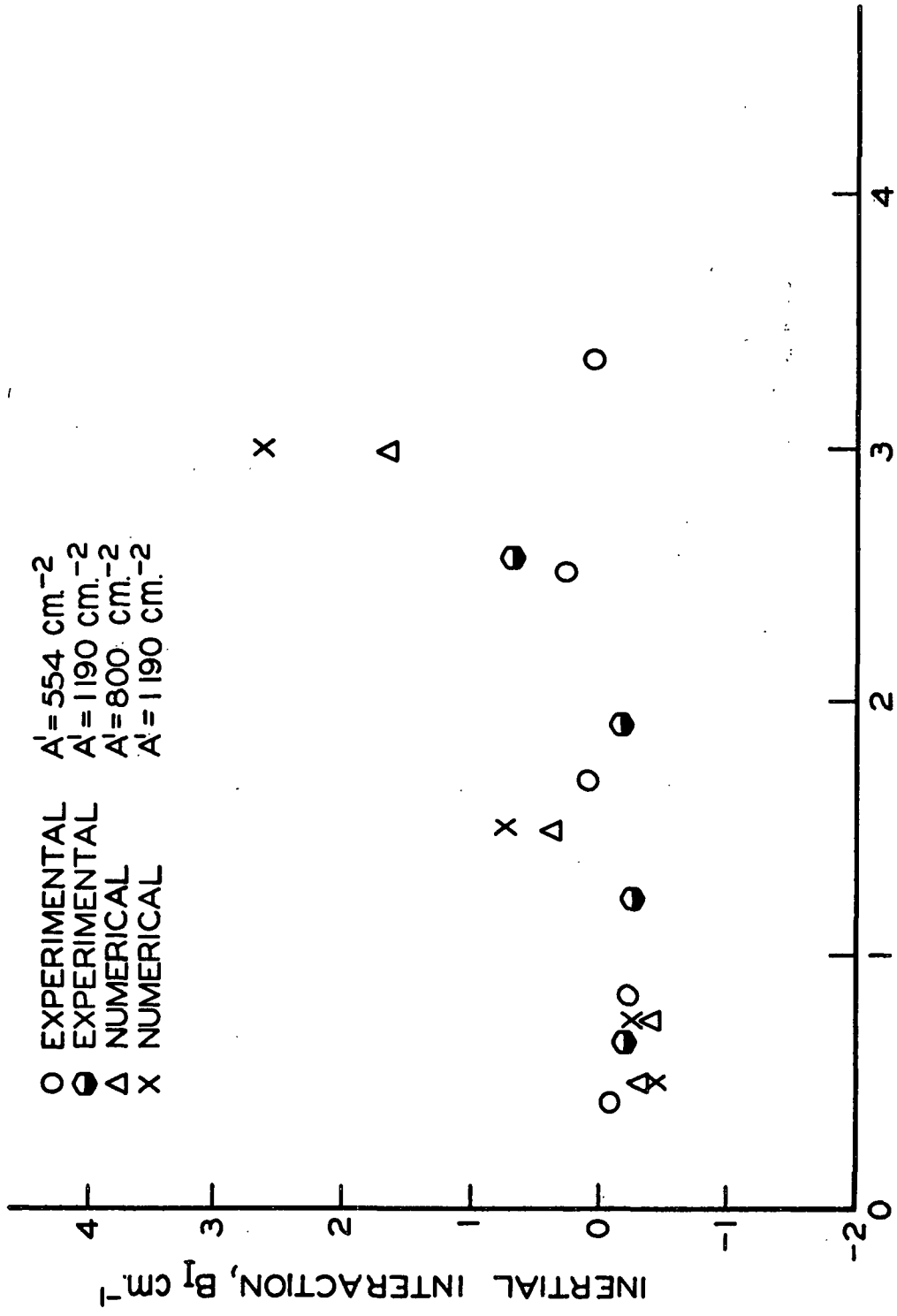

Figure 20. Inertial Interaction vs. Mat Thickness

DISCUSSION

Both the experimental program and the mathematical model have definitely shown an interaction taking place between the mat and the cylinders as evidenced in Fig. 19 and 20. It is now of interest to determine the nature of this interaction.

With regard to the viscous interaction, $\underline{A_I}$, it would appear that there is considerable scatter in the results. It should be recalled, however, that each of these interaction values represent the results of three experiments, and that they are the differences of large numbers. The values of the viscous coefficient, from which the interaction is derived, are shown in Fig. 21 for the experimental data and in Fig. 22 for the data from the numerical model. These figures demonstrate the precision in the experimental results. Similarly, the inertial resistance is depicted in Fig. 23 for the experimental data. Since the mathematical mat has no inertial component, the precision in the combined mat-cylinder system is reflected in the interaction shown in Fig. 20.

The experimental viscous interaction appears to be low for the mat composed of only one layer of wire screen. It should be noted that these one-layer mats are not structurally the same as those of multiple layers. As a consequence, they should not be weighted too heavily in the analysis. It would then appear that the viscous interaction is a constant with a value of about 60 $cm.^{-1}$ for all mat thicknesses.

The results from the mathematical model have more scatter which can be attributed to the approximations and assumptions made in the development of the model. The less resistant mat has an interaction of about 100 $cm.^{-1}$, while the higher resistant mat has a value of about 150 $cm.^{-1}$. Despite the scatter, this is a significant difference.

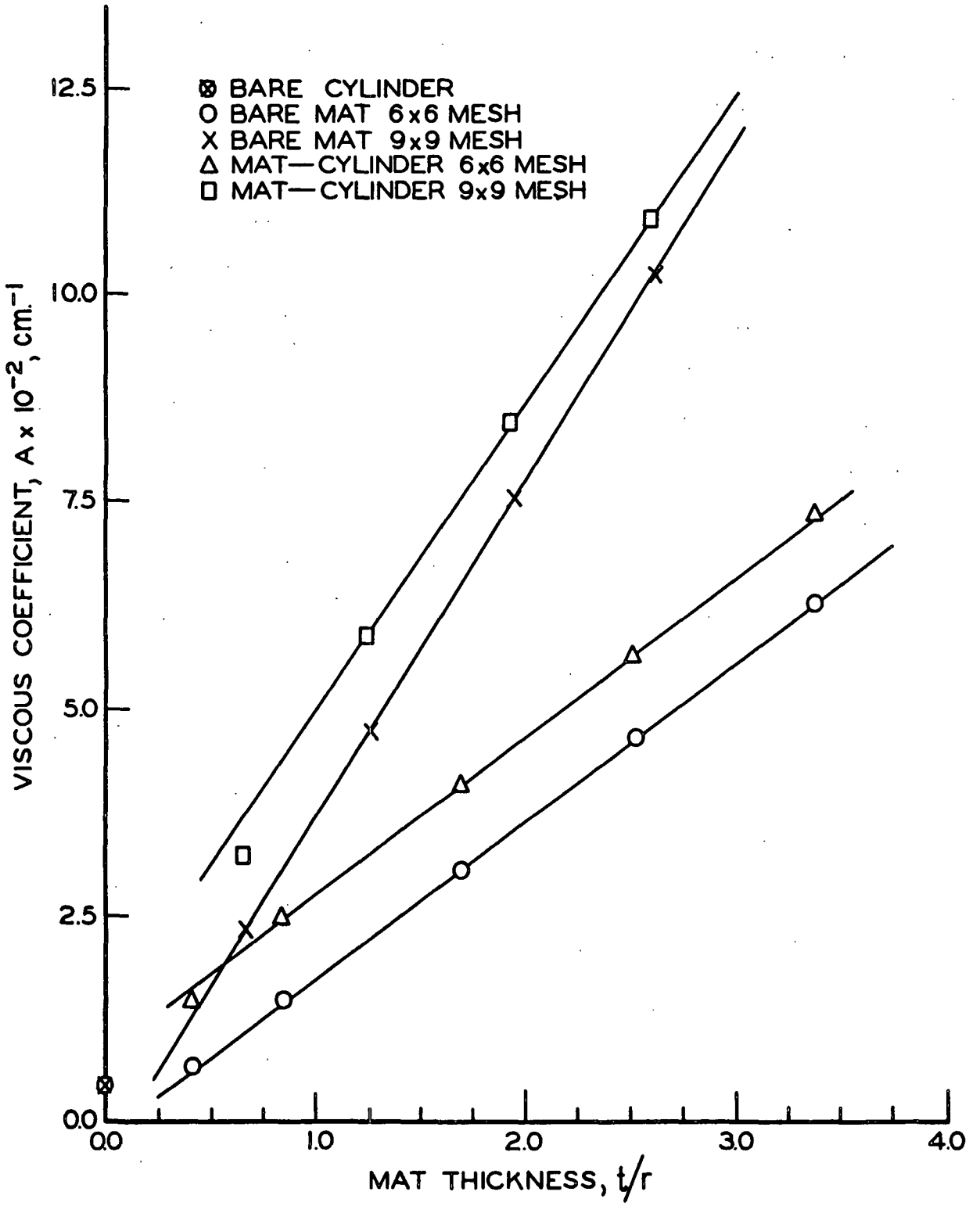

Figure 21. Viscous Coefficient vs. Mat Thickness from Experimental Data

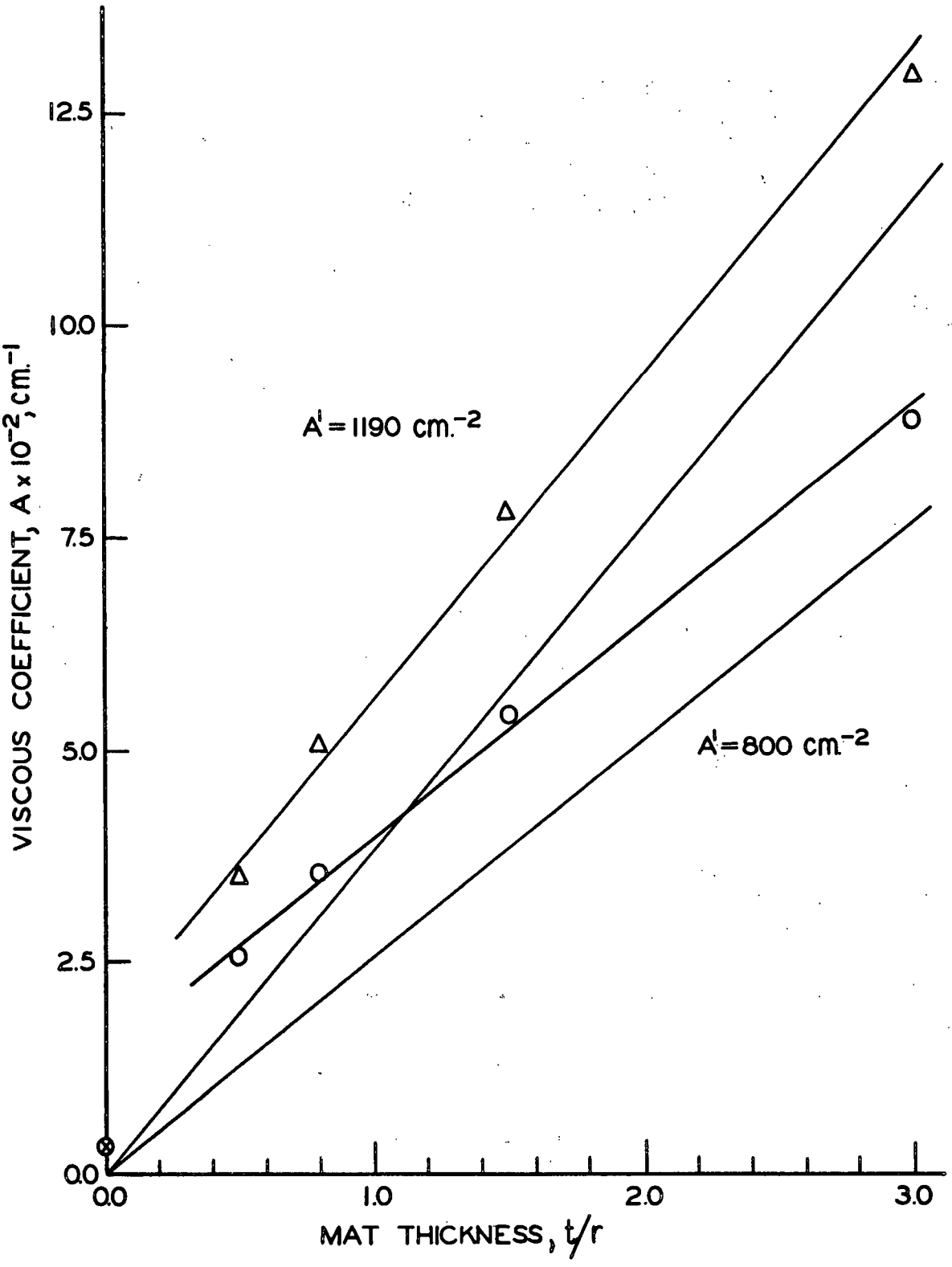

Figure 22. Viscous Coefficient vs. Mat Thickness from Numerical Solutions

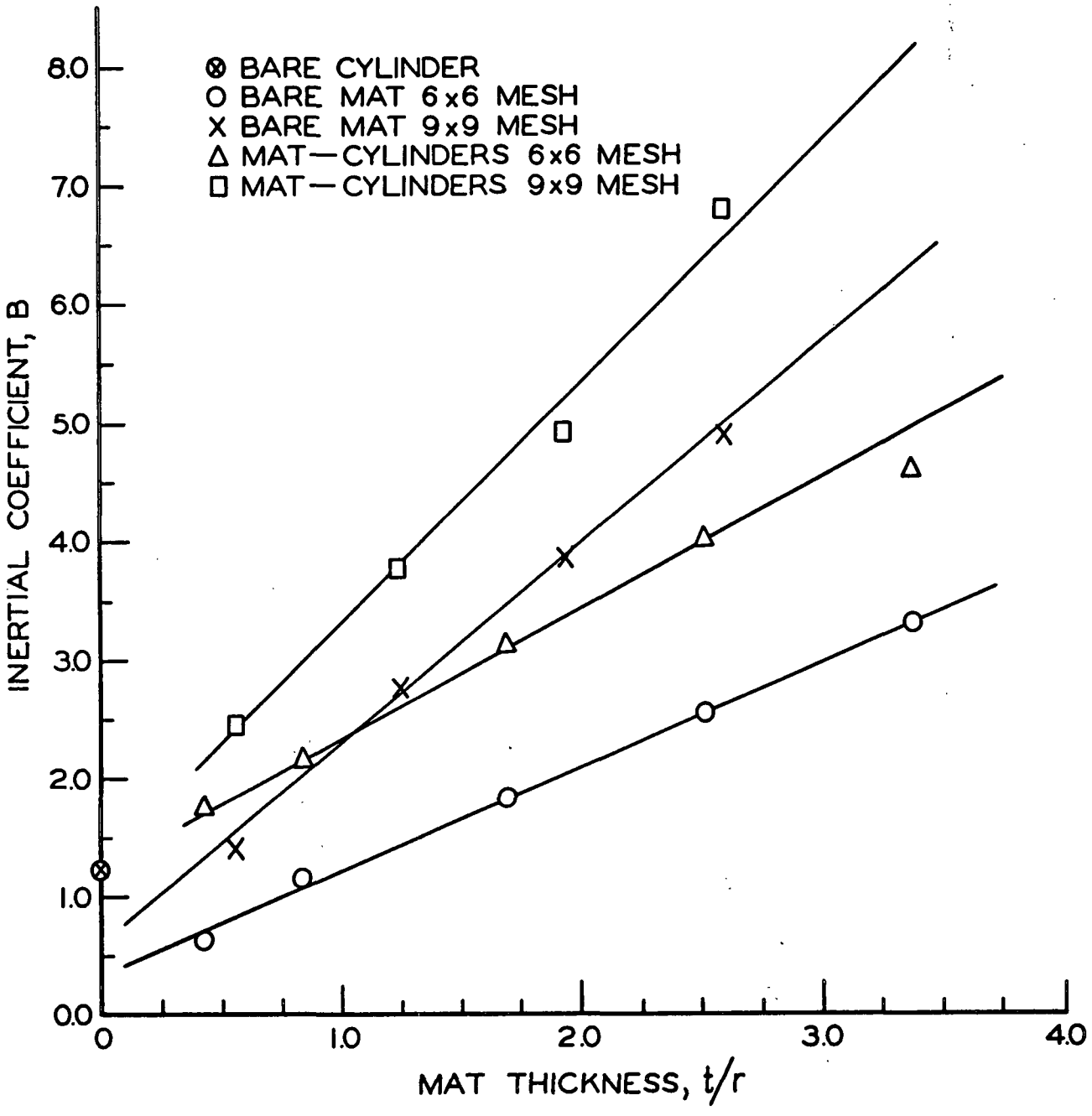

Figure 23. Inertial Coefficient vs. Mat Thickness from Experimental Data

The apparent discrepancy between the experimental system and the mathematical model may be accounted for in terms of the assumptions made in the theoretical model. The model assumes an isotropic porous medium which obeys D'Arcy's equation. The experimental mats, composed of wire screens, are far from being isotropic as a consequence of their construction. Peterson (36) has shown in experimental studies of fibrous mats that the resistance in the plane of the mat is about 25% less than the resistance in a direction normal to the plane of the mat. This result is due to the fact that the drag of the cylinder is greater for flow perpendicular to its longitudinal axis than for flow parallel to this same axis. Since a fiber mat and the layers of wire screens are similar in structure, this same two-dimensional resistance characteristic would be expected in the experimental program of this study. The effect of this character will be to reduce the "effective" resistance where the flow lines are not perpendicular to the plane of the mat. This will result in a lower interaction than that for an isotropic porous medium.

In looking at the inertial contribution depicted in Fig. 20, it is observed that there is a negative contribution to the total interaction for $t/r < 2$ and positive contributions for $t/r > 2$. The high values from the mathematical model are a consequence of the modeling procedure. The bare mat follows D'Arcy's equation where the inertial terms are considered to be negligible. However, the convective terms from the Navier-Stokes equation were included in the model of the mat. These terms are believed to have resulted in the inertial interaction, B_I.

The whole hydrodynamic interaction appears to be of a viscous nature with a small inertial contribution. It is of interest to determine where this interaction is occurring. Employing the mathematical model, it is possible to obtain the drag of the cylinder in the presence of the mat. On the basis of the results given in Table IV, the viscous resistance of the cylinder has increased slightly;

however, this only accounts for about 10% of the total viscous interaction. The inertial interaction, however, is slightly negative.

An analysis of the stream function--vorticity pictures (Fig. 4, 5, and 15-18) shows no difference in the wake of the cylinder with or without a mat present. The boundary layer separation point, as indicated by the zero streamline, has not changed and remains at 126° for $\underline{Re}$ = 40.

These facts would suggest that the interaction is taking place within the mat itself. A comparison of the stream function pictures for the bare cylinders and the mat-cylinders combined shows that the streamline paths have changed due to the presence of the mat. The streamlines upstream of the cylinder are depressed closer to the cylinder when the mat is present as depicted by dotted lines in Fig. 24.

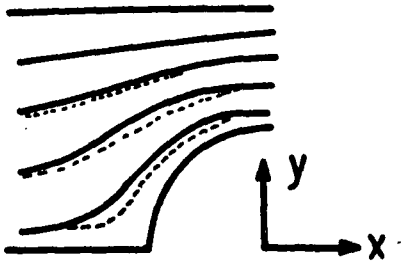

Figure 24. Comparison of Streamlines Around Cylinder

The longer paths of the streamlines would account for the increased resistance of the combined mat-cylinder system.

CONCLUSIONS

On the basis of the experimental model of the mat-wire system, it has been clearly shown that a definite hydrodynamic interaction exists between the cylinders and the mat. This macroscopic approach showed that most of the interaction was of a viscous nature. It was not possible, however, to determine where the interaction was taking place.

The mathematical model, based on the Navier-Stokes equation, verified the experimental results and showed that the increased resistance of the cylinders accounted for only 10% of the total interaction. An analysis of the wake as obtained from the mathematical model, shows no changes taking place with the presence of the mat. The remainder of the interaction occurs in the mat. This interaction is the result of the streamlines diverging around the cylinder later than those of the bare cylinder case. The increased path length taken by the fluid, results in a higher resistance through the mat.

The magnitude of the interaction is about a factor of two or three greater than the resistance of the cylinders. In terms of the specific resistance of the mat, however, the interaction is only about 10% as great. This interaction contributes significantly to the overall pressure loss for very thin mats, but is negligibly small for thick mats where the resistance of the mat is so large.

Concluding remarks can only emphasize the highly complex nature of the flow through this entire system. As the fluid flows through the mat and past the cylinders, the path taken by the fluid will be one which will result in the least overall resistance to flow. Hence, it is necessary to consider the two resistant elements as one entity and to make a microscopic analysis of the flow through it. Only after a systematic study of the effects of the properties of the individual elements can one predict the degree of interaction. With some

refinements, the mathematical model, based on the Navier-Stokes equation, can be a useful tool for further studies in the flow of fluids through complex systems.

SYMBOLS AND NOMENCLATURE

a = viscous coefficient of Forchheimer equation

A = modified viscous coefficient of Forchheimer equation

A' = specific viscous coefficient

b = inertial coefficient of Forchheimer equation

B = modified coefficient of Forchheimer equation

C_D = drag coefficient

D = drag per unit length of infinitely long cylinder

d = distance between centers of cylinders

g = gravitational constant, 977.4925 cm./sec.^{2}

G = defined in text

h = grid interval in iteration procedure

i = index; unit vector; $\sqrt{-1}$

j = index; unit vector

J = Jacobian of transformation

k = unit vector

L = length of cylinder

n = number of iterations

p = pressure variable

P = pressure variable

q = net velocity

Q = explained in text

r = r direction

R = radius of cylinders

Re = Reynolds number

s = contour arc length, vortex length

S = specific surface

$\underline{t}$ = mat thickness

$\underline{T}$ = time

$\underline{u}$ = velocity component in $\underline{x}$ direction

$\underline{U}$ = dimensionless velocity in $\underline{x}$ direction

$\underline{U}_\infty$ = approach velocity

$\underline{v}$ = velocity component in $\underline{y}$ direction

$\underline{V}$ = dimensionless velocity component in $\underline{y}$ direction

$\underline{w}$ = velocity vector

$\underline{x}$ = $\underline{x}$ coordinate

$\underline{X}$ = dimensionless $\underline{x}$ coordinate

$\underline{y}$ = $\underline{y}$ coordinate

$\underline{Y}$ = dimensionless $\underline{y}$ coordinate

$\underline{z}$ = complex physical plane

α = viscous resistance coefficient

β = inertial resistance coefficient

ε = porosity

ζ = coordinate in complex in conformal mapping

η = coordinate in complex plane in conformal mapping

θ = temperature

μ = viscosity of fluid

ν = kinematic viscosity of fluid

ξ = complex plane

π = 3.1415927

ρ = density of fluid

τ = shear stress

ϕ = angle from stagnation point

ψ = stream function

Ψ = dimensionless stream function

ω = vorticity

Ω = dimensionless vorticity

∞ = infinity

$\rightharpoonup$ = vector

$| \, |$ = positive magnitude

∇ = del operator

∇^2 = Laplacian operator

$\int$ = integral

ln = natural log

log = common log

cosh = hyperbolic cosine function

sinh = hyperbolic sine function

$\sum$ = summation

ACKNOWLEDGMENTS

The guidance, support, and criticism of Mr. Heribert Meyer, Chairman of my Advisory Committee, and the other members of the Committee, Dr. Thomas Grace and Dr. Richard Nelson, during this thesis study are greatly appreciated. The inspiration and early support from the late Dr. Ingmanson, to whom this work is dedicated, were most influential in the early stages of this study and his help is gratefully acknowledged.

The discussions with Dr. Robert Holm and Mr. John Bachhuber on the numerical computations and their encouragement in this study are also acknowledged with appreciation.

The services and support of Messrs. Bruce Andrews, Lyle Dambruch, Milo Godschalx, William Krueger, and their staffs in the construction and operation of the experimental equipment is appreciated. Sincere thanks also go out to the library and other staff services within The Institute of Paper Chemistry

The use of the Ferranti-Shirley plate-cone viscometer of the American Can Company, Neenah, Wisconsin, is acknowledged. Sincere appreciation is also given to the Kimberly-Clark Corporation, Neenah, Wisconsin, for the use of their IBM 7074 computer and to the Thilmany Pulp and Paper Company, Kaukauna, Wisconsin, for the use of their IBM System 360-40 computer. These computers were used in the development of the numerical model.

And finally, to my dear wife, Elizabeth, for her tender patience and understanding, and her devoted labor in the typing of reports and the preparation of this manuscript, goes my love.

LITERATURE CITED

1. Whitney, R. P., Ingmanson, W. L., and Han, S. T., Tappi 38, no. 3:157-66(1955).

2. Han, S. T. Status of sheet forming process--a critical review. Appleton, Wisconsin, The Institute of Paper Chemistry, 1965. 342 p.

3. Ingmanson, W. L., and Andrews, B. D., Tappi 46, no. 3:150-5(1961).

4. Han, S. T., and Ingmanson, W. L., Tappi 50, no. 4:176-80(1967).

5. Ingmanson, W. L. Unpublished work, 1963.

6. Ingmanson, W. L., Han, S. T., Wilder, H. T., and Myers, W. T., Jr., Tappi 44, no. 1:47(1961).

7. Arnold, E. W. Unpublished work, 1960.

8. Meyer, H. Unpublished work, 1964.

9. Kiser, K. M., and Hoelacker, H. E., Ind. Eng. Chem. 49:970-7(1957).

10. Dryden, H. L., and Schubauer, G. B., J. Aeronautical Sci. 14:221-8(1947).

11. Elder, J. W., J. Fluid Mechanics 5:355-68(1957).

12. McCarthy, J. H., J. Fluid Mechanics 19:491-512(1964).

13. Schlichting, H. Boundary layer theory. 4th ed. New York, McGraw-Hill Book Company, Inc., 1960. 647 p.

14. Batchelor, G. K. An introduction to fluid dynamics. Cambridge, Cambridge University Press, 1967. 615 p.

15. Marris, A. W., J. Basic Eng. 31:185-97(June, 1964); Trans. ASME 86(D):185-97 (1964).

16. Grove, A. S., Shair, F. H., Peterson, E. E., and Acrivos, A., J. Fluid Mechanics 19:60-80(1965).

17. Fromm, J. The time dependent flow of an incompressible viscous fluid. In. Alder's Methods in computational physics. Vol. 3. p. 346-82. New York, Academic Press, 1964.

18. Thom, A., Proc. Roy. Soc., A, 141:651-69(1933).

19. Thom, A., and Apelt, C. J. Field computations in engineering and physics. New York, D. Van Nostrand Company, Ltd., 1961. 165 p.

20. Kawaguti, M., J. Phys. Soc. Japan 18, no. 6:734-57(Nov.-Dec., 1953).

21. Allen, D. N., and Southwell, R. V., Quart. J. Mech. and Appl. Math. 8, no. 2:129-45(1955).

22. Greenspan, D., Jain, P. C., Manohair, R., Noble, B., and Sakurai, A. Numerical studies of the Navier-Stokes equation. MRC TSR 482. Madison, Wis., Mathematical Research Center, University of Wisconsin, May, 1964. 56 p.

23. Burggraf, O. R., J. Fluid Mechanics 24:113-51(1966).

24. Hildebrand, F. B. Advanced calculus for applications. Englewood Cliffs, New Jersey, Prentice Hall, Inc., 1962. 646 p.

25. Lapidus, L. Digital computations for chemical engineers. New York, McGraw-Hill Book Company, Inc., 1962. 407 p.

26. Collatz, L. The numerical treatment of differential equations. 3rd ed. Berlin, Springer-Verlag, 1960. 568 p. (English translation by P. G. Williams.)

27. Forsythe, G. E., and Wasow, W. R. Finite-difference methods for partial differential equations. New York, John Wiley & Sons, Inc., 1960. 444 p.

28. Taneda, S., J. Phys. Soc. Japan II:302(1956). [Found in (14), p. 260.]

29. Tietjens, O. G., and Prandtl, L. Applied hydro- and aeromechanics. 1st ed. New York, McGraw-Hill Book Company, 1934. 311 p. (English translation by J. P. Den Hartog.)

30. Whitaker, S., Chem. Eng. Sci. 21:291-300(1966).

31. Brinkman, H. C., Appl. Scientific Research A1:27-34, 81-6(1947).

32. Tamada, K., and Fujikawa, H., Quarterly J. Mech. and Appl. Math. 10, no. 4:425-32(1957).

33. Miyagi, T., J. Phys. Soc. Japan 13, no. 5:493-6(1958).

34. Tritton, D. J., J. Fluid Mechanics 6:547-67(1959).

35. Shair, F. H., Grove, A. S., Petersen, E. E., and Acrivos, A. A., J. Fluid Mechanics 17:546-50(1946).

36. Peterson, R. M. Private communications, 1968.

37. Hodgman, C. D. Handbook of chemistry and physics. 39th ed. Cleveland, Ohio, Chemical Rubber Co., 1957.

38. Perry, J. H. Chemical engineers' handbook. 3rd. ed. New York, McGraw-Hill Book Company, 1950.

39. Tuve, G. L., and Sprenkle, R. E., Instruments 6:201-6(1933).

APPENDIX I

DERIVATION OF FINITE DIFFERENCE EQUATION FOR NO SLIP BOUNDARY CONDITION

The values of Ψ are known along the boundary; however, the initial boundary values of Ω are unknown and must be obtained as the solution proceeds. The solid boundary with a finite difference grid is shown in Fig. 25.

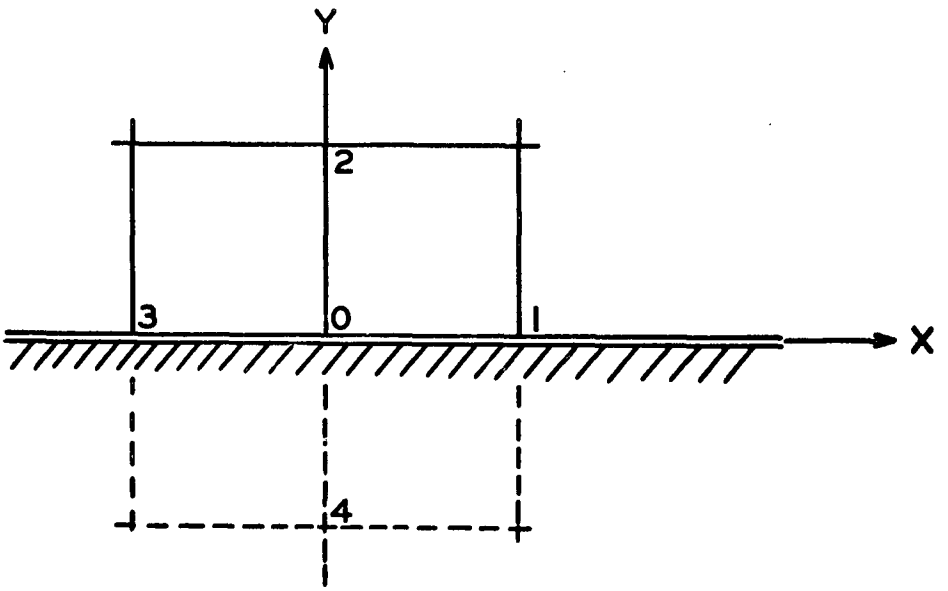

Figure 25. Solid Boundary

A Taylor expansion about 0 results in

$$\Psi_2 = \Psi_0 + h \left(\frac{\partial \Psi}{\partial Y}\right)_0 + \frac{h^2}{2!} \left(\frac{\partial^2 \Psi}{\partial Y^2}\right)_0 + \frac{h^3}{3!} \left(\frac{\partial^3 \Psi}{\partial Y^3}\right)_0 + \ldots . \qquad (57)$$

Now, from Equation (20)

$$\frac{\partial^2 \Psi}{\partial Y^2} = -\Omega - \frac{\partial^2 \Psi}{\partial X^2} . \qquad (58)$$

Differentiation results in

$$\frac{\partial^3 \Psi}{\partial Y^3} = - \frac{\partial \Omega}{\partial Y} - \frac{\partial^2}{\partial X^2} \left(\frac{\partial \Psi}{\partial Y} \right). \tag{59}$$

The boundary conditions stated that $\Psi = 0$ along the solid boundary and hence, all derivatives of Ψ with respect to $\underline{X}$ are zero. Also,

$$\left(\frac{\partial \Psi}{\partial Y} \right)_0 = 0. \tag{25}$$

Substitution of these quantities into Equation (57) gives

$$\Psi_2 = \Psi_0 - \frac{h^2}{2} \Omega_0 - \frac{h^3}{6} \left(\frac{\partial \Omega}{\partial Y} \right). \tag{60}$$

Terms after the second are neglected so that the vorticity may be computed from the following:

$$\Omega_0 = 2 (\Psi_0 - \Psi_2)/h^2. \tag{61}$$

When transforming the coordinate system, the above equation becomes

$$\Omega_0 = 2 J (\Psi_0 - \Psi_2)/h^2. \tag{62}$$

This derivation was obtained from Thom and Apelt (19).

APPENDIX II

EXPERIMENTAL APPARATUS AND MATERIALS

PROPERTIES OF INDOPOL L-10 POLYMER

The fluid used in this thesis study is a synthetic white oil consisting of polyisobutylene. In order to avoid density and viscosity measurements with each run, a set of density-temperature and viscosity-temperature curves were obtained.

The density of the oil was determined by means of a hydrometer thermometer with a specific gravity range of 0.700 to 0.850. The hydrometer was placed in a 1-liter graduated cylinder of the oil. The graduate was then placed in a large beaker of water which could be heated with a hot plate. The oil was well stirred and, when the hydrometer settled, a reading was obtained along with the temperature. This was performed over a temperature range of 17-35°C. The hydrometer was then calibrated with absolute ethanol and compared with values found in the handbook (37). The experimental values agreed with the handbook values within 0.6%. The density-temperature data, along with the least squares regression line, are presented in Fig. 26. The density is then computed from the following equation:

$$\rho = 0.84736 - 0.00056625\ \theta \qquad (63)$$

where θ is the temperature of the oil in °C.

The kinematic viscosity-temperature curve was then determined. A Cannon-Fenske capillary viscometer (No. 200) was placed in a well-circulated water bath whose temperature could be maintained to $\pm$ 0.01°C. The viscometer was first calibrated with a National Bureau of Standards oil (Type K, Lot 19) at 20, 25, 30, and 37.78°C. Efflux times were obtained in quintuple at the same temperatures. The kinematic viscosity was then fitted to a third-order polynomial equation which appears as follows:

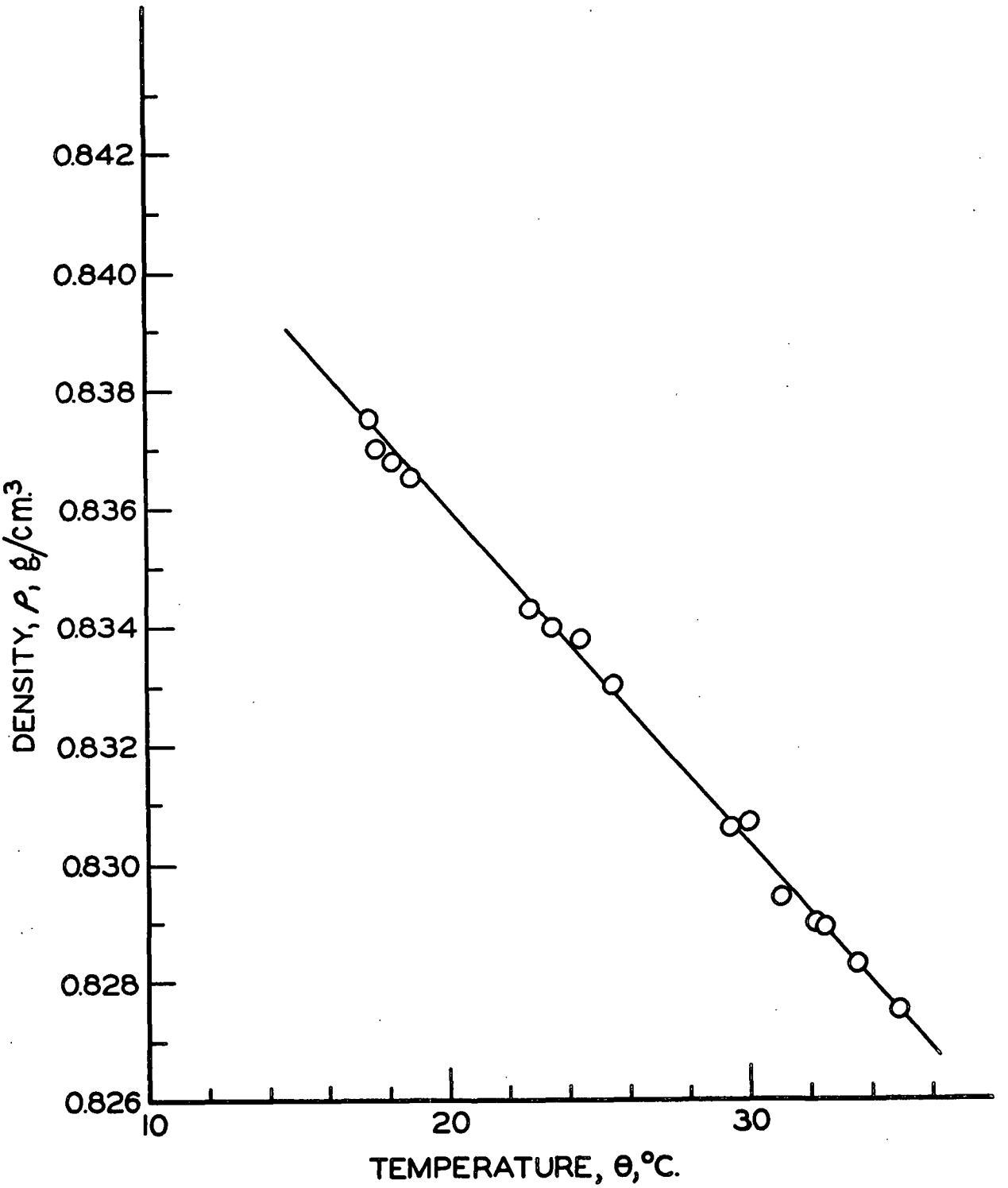

Figure 26. Density vs. Temperature for Indopol L-10 Polymer

$$\nu = 153.34 - 8.6756 \cdot \theta + 0.20197 \cdot \theta^2 - 0.001747 \cdot \theta^3. \qquad (63)$$

The curve and the data points are presented in Fig. 27.

VELOCITY MEASUREMENTS

The approach velocity, U_∞, was measured with the use of a manometer and orifice plate. The orifice plate was built according to the Chemical Engineers' Handbook (38). The plate is a sharp-edged orifice, 2.01 inches in diameter with 1/16-inch radius pressure taps. The orifice plate was calibrated in place by pumping water from a large pool, through the lower portion of the test zone, the orifice plate, and into a tank of known volume. The volumetric flow rate ranged from 70 to 200 gallons per minute. The orifice equation is as follows:

$$Q = CS_2 \sqrt{2g\ \Delta H_f} \qquad (65)$$

where Q is the volumetric flow rate, C is the discharge coefficient, S_2 is the cross-sectional area of the orifice, g is the gravitational constant, and ΔH_f is the pressure drop in head of flowing fluid. The coefficient of discharge, C, was determined to be 0.632. Since the cross-sectional area of the test zone is known, the velocity could then be computed. When oil was placed in the pipe loop, however, it was found that the orifice Reynolds number, Re_o, was below that where the discharge coefficient is constant. Tuve and Sprenkle (39) presented some experimental coefficients with Reynolds numbers Re_o between 200 and 20,000 for the same type orifice plates. Their data over the range $450 < Re_o < 8000$ was described by the equation

$$C = 0.884 - 0.062 \cdot \log(Re_o). \qquad (66)$$

The experimental data of this thesis study fell within this range. The appropriate discharge coefficient for each data point (ΔP-U_∞) was found by an iterative procedure until the coefficient changed by less than 0.1%.

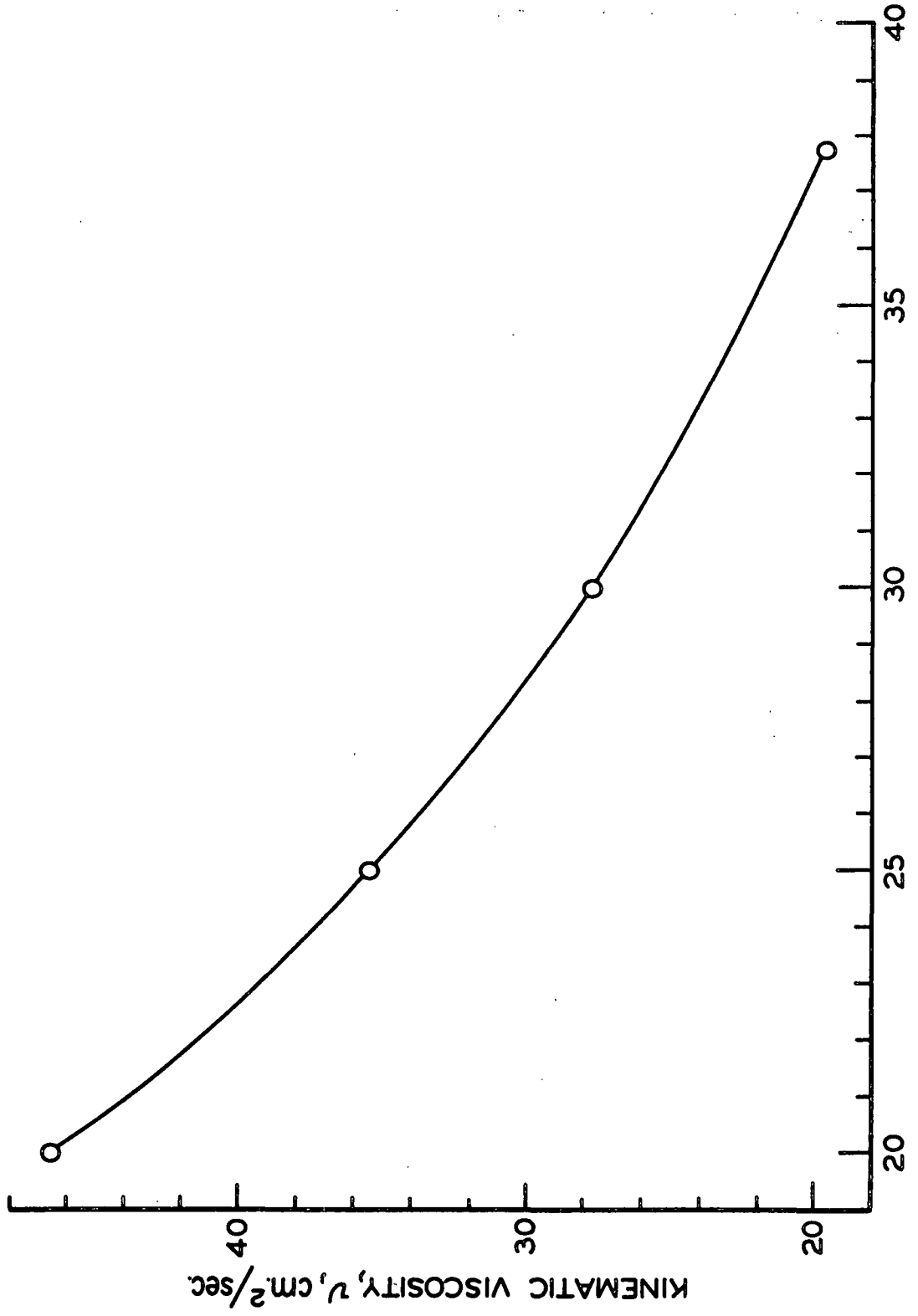

Figure 27. Kinematic Viscosity vs. Temperature for Indopol L-10 Polymer

Figure 28 is a schematic diagram of the orifice plate-manometer system. The two reservoirs are used to bleed air from the pressure lines leading to the orifice plate and to prevent air from entering the manometer. An air over flowing fluid, inverted U-type manometer was used. Equation (67) is the final working equation for converting the manometer reading to approach velocity.

$$U_\infty = 4.96\ C\ \sqrt{\Delta H_m\ \rho_m/\rho_f} \qquad (67)$$

where ΔH_m is the manometer reading in centimeters of the oil (Indopol L-10), ρ_m is the density of the oil in the manometer, and ρ_f is the density of the flowing fluid (both computed from temperature).

PRESSURE DROP MEASURING SYSTEM

The heart of the pressure measuring system is the PACE Engineering Company pressure transducer (Model KP-15) and transducer indicator (Model CD25). Figure 29 is a schematic of the pressure measuring system. It was necessary to use air in the cavities of the transducer to minimize undesirable pressure fluctuations at the transducer. In addition, each of the reservoirs was preceded by a fluid resistance element which consisted of a 0.040-inch hole about ½-inch long bored through a piece of Lucite rod to further dampen out rapid pressure fluctuations. The 10-cm. H_2O diaphragm was calibrated in cm. of oil before each run and the accumulated data were used to obtain a calibration curve. This curve is then described by the following equation:

$$P_A = -0.011575 + 0.93289 \cdot P_I + 0.006472 \cdot P_I^2 + 0.0000692 \cdot P_I^3 . \qquad (68)$$

Here, P_A is the actual pressure (cm. of oil) and the P_I is the indicated pressure (cm. of oil). The indicated pressure is converted to the actual pressure and then to the c.g.s. system of pressure. The 100-cm. H_2O diaphragm was found to be accurate and required no correction.

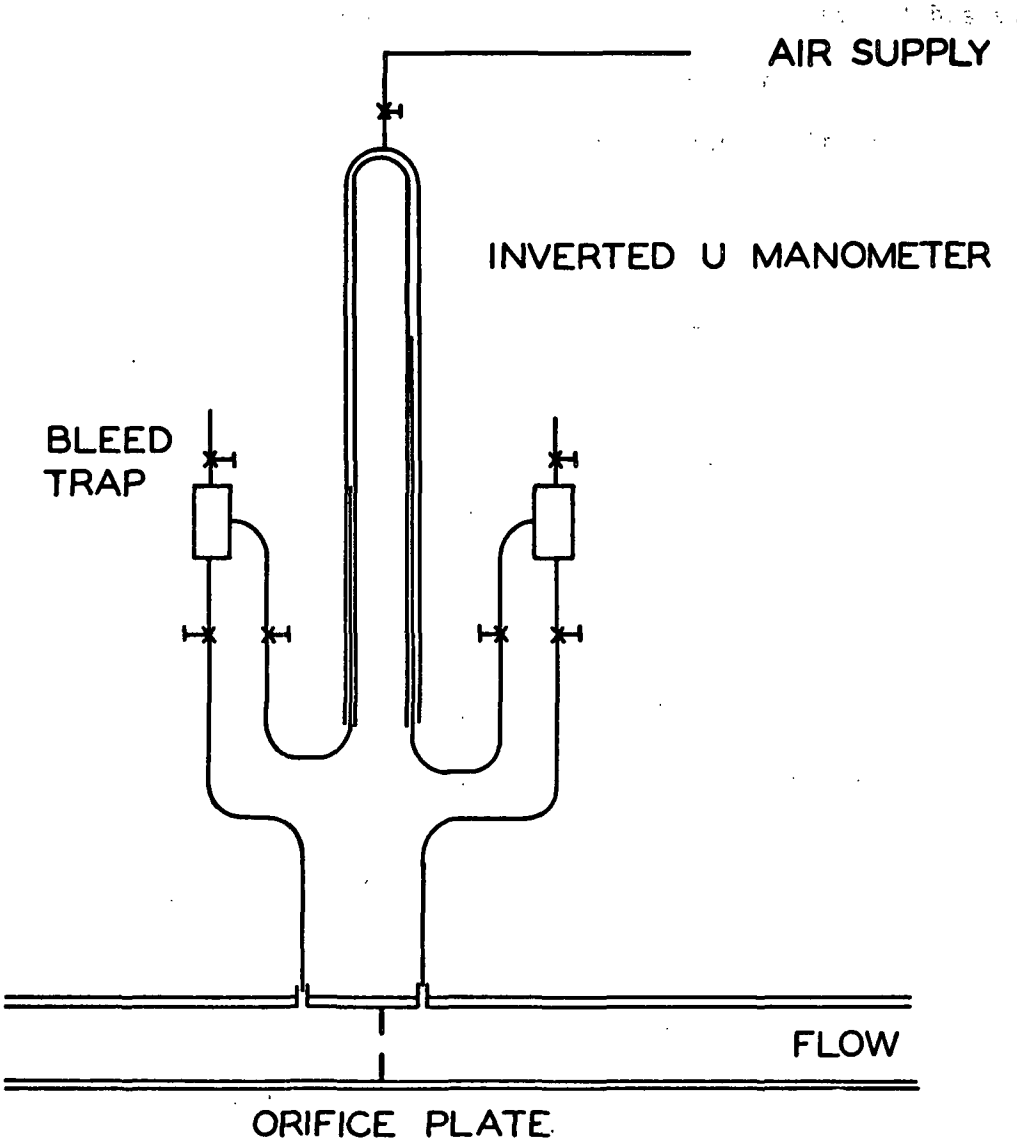

Figure 28. Schematic Diagram of Orifice-Manometer System

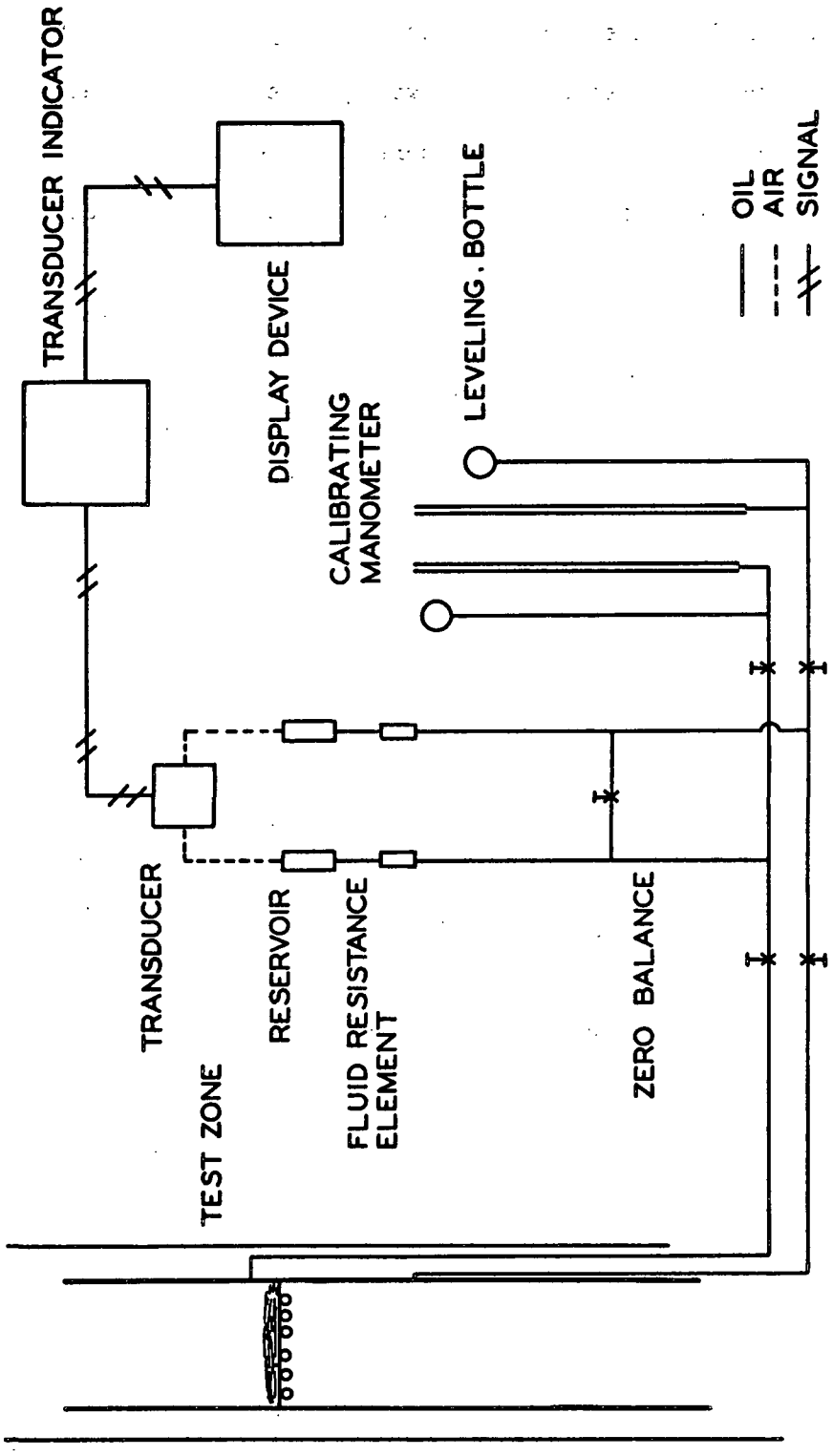

Figure 29. Schematic Diagram of Pressure Measuring System

APPENDIX III

EXPERIMENTAL DATA

The experimental data used in this thesis are presented in the following tables. The raw data have been converted with the equations presented in Appendix I. Equation (54) is fit to the data by means of a least squares regression. The coefficients are given with each run, along with a correlation coefficient.

TABLE V

BARE CYLINDERS DATA

Run No. 67121801
Mat Thickness = 0.00 Number of Layers = 0

θ Temperature, °C.	μ Viscosity, g./cm. sec.	ρ Density, $g./cm.^3$	U_∞ Velocity, cm./sec.	ΔP Press. Drop x 10^{-2}, $dynes/cm.^2$
23.00	0.3286	0.834	4.58	0.83
22.95	0.3295	0.834	6.03	1.20
23.00	0.3286	0.834	9.38	2.23
23.00	0.3286	0.834	9.40	2.26
23.05	0.3276	0.834	11.89	3.17
23.10	0.3267	0.834	14.25	3.96
22.40	0.3397	0.834	15.68	4.87
23.00	0.3286	0.834	17.28	5.54
23.00	0.3286	0.834	17.29	5.58
23.00	0.3286	0.834	18.75	6.29
22.85	0.3313	0.834	20.15	6.98
23.00	0.3286	0.834	21.43	7.69
23.00	0.3286	0.834	21.64	7.74
23.10	0.3267	0.834	22.70	8.37
22.95	0.3295	0.834	23.27	8.81
22.95	0.3295	0.834	23.31	8.84
22.85	0.3313	0.834	24.16	9.36
22.80	0.3322	0.834	24.30	9.45
22.70	0.3341	0.834	26.22	10.75
22.60	0.3360	0.834	26.69	11.04
22.30	0.3417	0.834	23.20	8.64
22.30	0.3417	0.834	23.20	8.70
23.00	0.3286	0.834	21.31	7.60
23.05	0.3276	0.834	21.35	7.62
23.00	0.3286	0.834	18.09	5.91
22.80	0.3322	0.834	15.26	4.62
22.90	0.3304	0.834	12.52	3.41
23.00	0.3286	0.834	10.28	2.54
23.00	0.3286	0.834	7.97	1.77
23.00	0.3286	0.834	6.10	1.22
23.00	0.3286	0.834	6.09	1.19

Viscous coefficient, A = 42.99 $cm.^{-1}$
Inertial coefficient, B = 1.215
Correlation coefficient = 0.9981

TABLE VI

BARE MAT DATA

Run No. 67121401
Mat Thickness = 0.134 Number of Layers = 1 Mesh 6 x 6

θ Temperature, °C.	μ Viscosity, g./cm. sec.	ρ Density, g./cm.^{3}	U_∞ Velocity, cm./sec.	ΔP Press. Drop x 10^{-2}, dynes/cm.^{2}
22.95	0.3295	0.834	3.80	0.88
22.85	0.3313	0.834	5.14	1.24
22.80	0.3322	0.834	7.23	1.87
22.90	0.3304	0.834	9.14	2.42
23.00	0.3286	0.834	14.22	4.21
23.00	0.3286	0.834	14.27	4.32
23.00	0.3286	0.834	16.86	5.27
23.00	0.3286	0.834	18.09	5.77
23.00	0.3286	0.834	18.23	5.86
23.00	0.3286	0.834	20.06	6.61
23.05	0.3276	0.834	21.44	7.06
23.05	0.3276	0.834	21.55	7.06
22.80	0.3322	0.834	22.43	7.43
23.00	0.3286	0.834	23.57	8.07
23.00	0.3286	0.834	23.64	8.09
23.60	0.3179	0.833	26.80	9.32
23.50	0.3196	0.834	23.23	7.59
23.40	0.3214	0.834	23.30	7.69
23.00	0.3286	0.834	22.40	7.47
23.15	0.3258	0.834	20.16	6.45

Viscous coefficient, $\underline{A}$ = 66.59 cm.$^{-1}$
Inertial coefficient, $\underline{B}$ = 0.623
Correlation coefficient = 0.9893

TABLE VII

BARE MAT DATA

Run No. 67121302
Mat Thickness = 0.266 Number of Layers = 2 Mesh 6 x 6

θ Temperature, °C.	μ Viscosity, g./cm. sec.	ρ Density, $g./cm.^3$	U_∞ Velocity, cm./sec.	ΔP Press. Drop x 10^{-2}, $dynes/cm.^2$
23.05	0.3276	0.834	4.90	2.51
23.00	0.3286	0.834	5.87	3.11
22.40	0.3397	0.834	7.20	4.06
22.40	0.3397	0.834	8.74	5.08
22.50	0.3378	0.834	10.66	6.38
23.05	0.3276	0.834	15.12	9.34
22.90	0.3304	0.834	16.19	10.38
22.95	0.3295	0.834	17.16	11.19
23.20	0.3249	0.834	18.72	12.28
23.00	0.3286	0.834	20.06	13.49
22.95	0.3295	0.834	21.36	14.61
22.95	0.3295	0.834	21.39	14.71
22.95	0.3295	0.834	22.45	15.61
23.05	0.3276	0.834	24.08	17.00
23.20	0.3249	0.834	26.30	19.03
23.20	0.3249	0.834	26.48	19.15
23.05	0.3276	0.834	22.51	15.56
22.95	0.3295	0.834	20.56	14.01
23.00	0.3286	0.834	17.17	11.16
23.00	0.3286	0.834	14.55	9.14
23.00	0.3286	0.834	12.04	7.18
23.00	0.3286	0.834	8.75	4.95
23.00	0.3286	0.834	6.23	3.34

Viscous coefficient, $A = 145.48\ cm.^{-1}$
Inertial coefficient, $B = 1.159$
Correlation coefficient = 0.9973

TABLE VIII

BARE MAT DATA

Run No. 67121201
Mat Thickness = 0.535 Number of Layers = 4 Mesh 6 x 6

θ Temperature, °C.	μ Viscosity, g./cm. sec.	ρ Density, g./cm.^{3}	U_∞ Velocity, cm./sec.	ΔP Press. Drop x 10^{-2}, dynes/cm.^{2}
23.00	0.3286	0.834	3.76	3.86
23.00	0.3286	0.834	4.99	5.55
23.00	0.3286	0.834	7.08	7.89
23.00	0.3286	0.834	9.20	10.44
23.00	0.3286	0.834	11.77	14.01
23.00	0.3286	0.834	11.85	14.05
23.00	0.3286	0.834	14.73	18.19
23.10	0.3267	0.834	14.86	18.29
23.00	0.3286	0.834	16.99	21.53
23.00	0.3286	0.834	17.06	21.51
23.00	0.3286	0.834	18.86	24.36
23.00	0.3286	0.834	20.72	27.16
23.00	0.3286	0.834	21.62	28.64
23.10	0.3267	0.834	22.50	30.15
23.10	0.3267	0.834	22.65	30.24
23.00	0.3286	0.834	21.97	29.01
23.00	0.3286	0.834	22.06	29.22
23.00	0.3286	0.834	20.71	26.96
23.00	0.3286	0.834	19.41	24.93
22.95	0.3295	0.834	18.19	23.25
23.00	0.3286	0.834	18.25	23.33
23.00	0.3286	0.834	15.80	19.52
22.85	0.3313	0.834	15.82	19.74
23.10	0.3267	0.834	14.70	17.89
23.10	0.3267	0.834	14.82	18.03
23.00	0.3286	0.834	12.18	14.28
23.05	0.3276	0.834	9.90	11.12
23.00	0.3286	0.834	5.36	5.70

Viscous coefficient, $\underline{A}$ = 303.6. cm.$^{-1}$
Inertial coefficient, $\underline{B}$ = 1.820
Correlation coefficient = 0.9886

TABLE IX

BARE MAT DATA

Run No. 67121202
Mat Thickness = 0.802 Number of Layers = 6 Mesh 6 x 6

θ Temperature, °C.	μ Viscosity, g./cm. sec.	ρ Density, $g./cm.^3$	U_∞ Velocity, cm./sec.	ΔP Press. Drop x 10^{-2}, $dynes/cm.^2$
23.00	0.3286	0.834	4.66	7.46
23.00	0.3286	0.834	5.46	8.91
23.00	0.3286	0.834	6.80	11.47
23.05	0.3276	0.834	10.19	17.58
22.60	0.3360	0.834	12.05	21.88
22.80	0.3322	0.834	14.11	26.01
23.00	0.3286	0.834	16.25	30.37
23.00	0.3286	0.834	17.53	33.18
22.90	0.3304	0.834	18.86	36.52
22.90	0.3304	0.834	18.95	36.73
23.00	0.3286	0.834	20.44	39.91
23.00	0.3286	0.834	21.24	41.45
23.00	0.3286	0.834	21.51	42.45
23.00	0.3286	0.834	22.42	44.24
22.85	0.3313	0.834	18.93	36.42
23.00	0.3286	0.834	15.92	29.53
23.10	0.3267	0.834	13.22	23.38
23.30	0.3231	0.834	11.55	19.77

Viscous coefficient, $\underline{A}$ = 461.79 $cm.^{-1}$
Inertial coefficient, $\underline{B}$ = 2.521
Correlation coefficient = 0.9935

TABLE X

BARE MAT DATA

Run No. 67121301
Mat Thickness = 1.064 Number of Layers = 8 Mesh 6 x 6

θ Temperature, °C.	μ Viscosity, g./cm. sec.	ρ Density, g./cm.^{3}	U_∞ Velocity, cm./sec.	ΔP Press. Drop $x_2 10^{-2}$, dynes/cm.
23.20	0.3249	0.834	3.21	6.55
23.05	0.3276	0.834	4.78	10.32
23.00	0.3286	0.834	6.53	14.63
23.00	0.3286	0.834	6.59	14.71
23.10	0.3267	0.834	8.74	20.51
23.15	0.3258	0.834	8.84	20.30
23.15	0.3258	0.834	8.97	20.65
22.80	0.3322	0.834	12.03	29.05
22.80	0.3322	0.834	14.89	37.24
22.80	0.3322	0.834	15.13	37.57
23.20	0.3249	0.834	17.51	44.24
23.20	0.3249	0.834	17.64	44.47
23.00	0.3286	0.834	18.87	48.64
23.00	0.3286	0.834	18.95	48.96
22.90	0.3304	0.834	20.94	55.31
22.90	0.3304	0.834	21.01	55.53
23.10	0.3267	0.834	22.34	58.82
23.20	0.3249	0.834	22.41	58.82
23.00	0.3286	0.834	20.79	54.51
23.05	0.3276	0.834	17.86	45.18
23.05	0.3276	0.834	17.94	45.57
23.05	0.3276	0.834	17.92	45.29
23.00	0.3286	0.834	15.00	36.74
23.00	0.3286	0.834	12.39	29.55
23.15	0.3258	0.834	10.23	23.85
23.15	0.3258	0.834	10.26	23.94
23.00	0.3286	0.834	7.94	18.10

Viscous coefficient, $A = 624.39$ cm.$^{-1}$
Inertial coefficient, $B = 3.299$
Correlation coefficient = 0.9892

TABLE XI

BARE MAT DATA

Run No. 67082801
Mat Thickness = 0.212 Number of Layers = 1 Mesh 9 x 9

θ Temperature, °C.	μ Viscosity, g./cm. sec.	ρ Density, g./cm.^{3}	U_∞ Velocity, cm./sec.	ΔP Press. Drop x 10^{-2}, dynes/cm.^{2}
26.20	0.2768	0.832	3.09	2.05
26.30	0.2754	0.832	3.45	2.44
26.40	0.2740	0.832	5.31	3.71
26.40	0.2740	0.832	5.38	3.81
26.40	0.2740	0.832	6.88	4.88
26.50	0.2726	0.832	7.03	4.98
26.50	0.2726	0.832	8.59	6.25
26.50	0.2726	0.832	8.75	6.35
26.60	0.2712	0.832	8.88	6.45
26.90	0.2671	0.832	11.33	8.50
26.90	0.2671	0.832	11.34	8.60
27.00	0.2657	0.832	13.02	10.16
27.10	0.2644	0.832	13.19	10.16
27.20	0.2631	0.831	13.32	10.36
27.30	0.2618	0.831	15.43	12.31
27.30	0.2618	0.831	15.55	12.41
27.40	0.2605	0.831	15.66	12.51
27.50	0.2592	0.831	17.61	14.27
27.60	0.2579	0.831	17.70	14.17
27.60	0.2579	0.831	17.75	14.17
27.70	0.2566	0.831	17.82	14.27
27.90	0.2541	0.831	20.29	16.61
28.10	0.2516	0.831	20.30	16.71
28.30	0.2491	0.831	22.00	18.27
28.50	0.2467	0.831	22.17	18.37
28.60	0.2455	0.831	22.31	18.57
28.70	0.2443	0.831	22.33	18.47
28.90	0.2420	0.830	21.83	17.79
29.00	0.2408	0.830	21.98	17.69
29.20	0.2385	0.830	20.81	16.32
29.30	0.2374	0.830	20.79	16.42
29.40	0.2363	0.830	18.98	14.76
29.50	0.2352	0.830	19.10	14.76
29.60	0.2341	0.830	17.17	12.60
29.60	0.2341	0.830	17.06	12.41
29.70	0.2329	0.830	17.19	12.90
29.80	0.2319	0.830	15.73	11.43
30.00	0.2297	0.830	16.01	11.63

TABLE XI (Continued)

BARE MAT DATA

Run No. 67082801
Mat Thickness = 0.212 Number of Layers = 1 Mesh 9 x 9

θ Temperature, °C.	μ Viscosity, g./cm. sec.	ρ Density, $g./cm.^3$	U_∞ Velocity cm./sec.	ΔP Press. Drop x 10^{-2}, $dynes/cm.^2$
29.90	0.2308	0.830	15.83	11.43
30.00	0.2297	0.830	14.08	9.87
30.00	0.2297	0.830	14.08	9.77
30.00	0.2297	0.830	12.56	8.50
30.00	0.2297	0.830	12.60	8.60
30.00	0.2297	0.830	11.22	7.62
30.00	0.2297	0.830	11.22	7.52
30.00	0.2297	0.830	9.82	6.54
30.00	0.2297	0.830	9.77	6.45
30.00	0.2297	0.830	8.48	5.37
30.00	0.2297	0.830	8.43	5.37
30.00	0.2297	0.830	6.99	4.30
30.00	0.2297	0.830	7.02	4.30
28.60	0.2455	0.831	2.56	1.46
28.50	0.2467	0.831	4.44	2.63
28.50	0.2467	0.831	5.70	3.51
28.50	0.2467	0.831	5.81	3.61
28.50	0.2467	0.831	7.37	4.88
28.50	0.2467	0.831	7.49	4.98
28.50	0.2467	0.831	9.14	6.15
28.50	0.2467	0.831	9.31	6.45
28.50	0.2467	0.831	11.13	7.91
28.50	0.2467	0.831	11.20	7.91
28.60	0.2455	0.831	13.18	9.67
28.70	0.2443	0.831	13.45	9.77
28.70	0.2443	0.831	13.48	9.87
28.80	0.2432	0.831	15.20	11.43
28.80	0.2432	0.831	15.40	11.53
28.80	0.2432	0.831	15.50	11.63
28.90	0.2420	0.830	17.43	13.39
29.00	0.2408	0.830	17.88	13.68
29.20	0.2385	0.830	20.22	15.83
29.30	0.2374	0.830	20.48	16.12
29.40	0.2363	0.830	22.11	17.79
29.60	0.2341	0.830	22.34	17.88
29.70	0.2329	0.830	22.43	17.98
29.90	0.2308	0.830	22.06	17.39
30.00	0.2297	0.830	22.10	17.30
30.10	0.2286	0.830	20.78	15.83

TABLE XI (Continued)

BARE MAT DATA

Run No. 67082801
Mat Thickness = 0.212 Number of Layers = 1 Mesh 9 x 9

θ Temperature, °C.	μ Viscosity, g./cm. sec.	ρ Density, $g./cm.^3$	U_∞ Velocity, cm./sec.	ΔP Press. Drop x 10^{-2}, $dynes/cm.^2$
30.20	0.2276	0.830	20.78	15.93
30.20	0.2276	0.830	18.87	14.17
30.30	0.2265	0.830	18.91	14.17
30.30	0.2265	0.830	17.07	12.21
30.40	0.2255	0.830	17.20	12.51
30.50	0.2244	0.830	15.57	10.94
30.60	0.2234	0.830	15.65	10.94
30.60	0.2234	0.830	14.09	9.57
30.60	0.2234	0.830	14.11	9.67
30.00	0.2297	0.830	14.22	9.77
30.60	0.2234	0.830	12.73	8.40
30.70	0.2223	0.829	12.78	8.30
30.70	0.2223	0.829	11.45	7.33
30.70	0.2223	0.829	11.55	7.42
30.70	0.2223	0.829	9.82	6.25
30.60	0.2234	0.830	10.01	6.25
30.60	0.2234	0.830	10.07	6.35
30.60	0.2234	0.830	8.66	5.37
30.60	0.2234	0.830	8.70	5.37
30.60	0.2234	0.830	7.37	4.39
30.60	0.2234	0.830	5.16	3.03
30.60	0.2234	0.830	3.50	1.95

Viscous coefficient, A = 231.69 $cm.^{-1}$
Inertial coefficient, B = 1.404
Correlation coefficient = 0.9907

TABLE XII

BARE MAT DATA

Run No. 67082201
Mat Thickness = 0.394 Number of Layers = 2 Mesh 9 x 9

θ Temperature, °C.	μ Viscosity, g./cm. sec.	ρ Density, g./cm.^{3}	U_∞ Velocity, cm./sec.	ΔP Press. Drop x 10^{-2}, dynes/cm.^{2}
23.10	0.3267	0.834	2.75	4.25
23.10	0.3267	0.834	3.84	6.15
23.10	0.3267	0.834	3.98	6.35
23.20	0.3249	0.834	5.41	8.89
23.20	0.3249	0.834	5.51	9.09
23.20	0.3249	0.834	7.12	11.92
23.30	0.3231	0.834	7.31	12.31
23.30	0.3231	0.834	9.04	15.73
23.30	0.3231	0.834	9.36	16.12
23.30	0.3231	0.834	9.51	16.32
23.30	0.3231	0.834	11.06	19.74
23.30	0.3231	0.834	11.33	20.33
23.60	0.3179	0.833	2.68	3.90
23.60	0.3179	0.833	2.68	4.00
23.70	0.3161	0.833	3.47	5.37
23.70	0.3161	0.833	3.49	5.37
23.70	0.3161	0.833	4.37	7.03
23.70	0.3161	0.833	4.46	7.13
23.70	0.3161	0.833	5.71	9.38
23.70	0.3161	0.833	5.77	9.38
23.70	0.3161	0.833	5.89	9.57
23.80	0.3144	0.833	7.33	12.21
23.80	0.3144	0.833	7.50	12.41
23.80	0.3144	0.833	9.50	16.03
23.80	0.3144	0.833	5.59	16.22
23.80	0.3144	0.833	11.63	20.82
23.90	0.3127	0.833	10.53	18.57
23.90	0.3127	0.833	10.63	18.67
23.90	0.3127	0.833	11.22	19.74
23.90	0.3127	0.833	11.37	20.13
24.00	0.3110	0.833	13.15	23.65
24.00	0.3110	0.833	13.43	24.24
24.10	0.3093	0.833	15.56	28.34
24.30	0.3060	0.833	16.71	30.88
24.30	0.3060	0.833	16.67	30.49
24.40	0.3043	0.833	17.65	32.45
24.40	0.3043	0.833	17.72	32.74
24.50	0.3027	0.833	18.64	34.99

TABLE XII (Continued)

BARE MAT DATA

Run No. 67082201
Mat Thickness = 0.394 Number of Layers = 2 Mesh 9 x 9

θ Temperature, °C.	μ Viscosity, g./cm. sec.	ρ Density, g./cm.^{3}	U_∞ Velocity, cm./sec.	ΔP Press. Drop x 10^{-2}, dynes/cm.^{2}
24.70	0.2995	0.833	18.86	34.79
24.90	0.2963	0.833	19.72	36.46
24.90	0.2963	0.833	19.75	36.55
25.00	0.2947	0.833	20.40	38.21
25.00	0.2947	0.833	20.57	38.51
25.10	0.2932	0.833	21.59	40.56
25.10	0.2932	0.833	21.73	40.56
25.20	0.2916	0.833	21.82	40.66
25.40	0.2886	0.832	24.03	45.74
25.60	0.2856	0.832	24.20	45.55
26.00	0.2797	0.832	23.89	44.28
26.10	0.2782	0.832	23.79	43.88
26.30	0.2754	0.832	22.08	39.49
26.50	0.2726	0.832	22.13	39.49
26.60	0.2712	0.832	20.97	36.65
26.70	0.2698	0.832	21.05	36.94
26.90	0.2671	0.832	20.33	34.70
26.90	0.2671	0.832	20.25	34.50
27.10	0.2644	0.832	18.68	30.88
27.20	0.2631	0.831	18.68	30.98
27.20	0.2631	0.831	16.63	26.78
27.30	0.2618	0.831	16.70	26.97
27.30	0.2618	0.831	15.08	23.75
27.30	0.2618	0.831	15.12	23.85
27.30	0.2618	0.831	13.38	20.23
27.30	0.2618	0.831	13.34	20.52
27.30	0.2618	0.831	13.38	20.62
27.30	0.2618	0.831	11.91	17.69
27.30	0.2618	0.831	11.86	17.98
27.30	0.2618	0.831	10.47	15.34
27.30	0.2618	0.831	10.42	15.44
27.20	0.2631	0.831	8.95	12.90
27.20	0.2631	0.831	8.99	13.00
27.10	0.2644	0.832	7.57	10.75
27.10	0.2644	0.832	7.50	10.65
27.10	0.2644	0.832	6.23	8.60
27.10	0.2644	0.832	6.13	8.50
27.00	0.2657	0.832	4.93	6.74

Viscous coefficient, $\underline{A}$ = 468.39 cm.$^{-1}$
Inertial coefficient, $\underline{B}$ = 2.793
Correlation coefficient = 0.9912

TABLE XIII

BARE MAT DATA

Run No. 67100301
Mat Thickness = 0.609 Number of Layers = 3 Mesh 9 x 9

θ Temperature, °C.	μ Viscosity, g./cm. sec.	ρ Density, $g./cm.^3$	U_∞ Velocity, cm./sec.	ΔP Press. Drop x 10^{-2}, $dynes/cm.^2$
26.80	0.2684	0.832	3.94	8.50
26.80	0.2684	0.832	4.09	8.79
26.80	0.2684	0.832	6.33	14.27
26.80	0.2684	0.832	6.64	14.76
26.80	0.2684	0.832	8.47	19.35
26.80	0.2684	0.832	8.78	20.03
26.90	0.2671	0.832	10.61	24.73
26.90	0.2671	0.832	10.77	25.21
27.00	0.2657	0.832	12.69	30.20
27.10	0.2644	0.832	12.87	30.59
27.30	0.2618	0.831	14.74	35.87
27.40	0.2605	0.831	14.99	36.26
27.60	0.2579	0.831	17.08	42.22
27.70	0.2566	0.831	17.31	42.71
28.00	0.2528	0.831	19.25	48.28
28.20	0.2503	0.831	19.51	48.58
28.50	0.2467	0.831	21.64	54.93
28.70	0.2443	0.831	21.99	55.52
29.00	0.2408	0.830	21.48	53.37
29.30	0.2374	0.830	21.69	53.56
29.50	0.2352	0.830	20.33	48.87
29.70	0.2329	0.830	20.35	48.58
29.80	0.2319	0.830	20.33	48.48
29.90	0.2308	0.830	18.81	43.88
30.00	0.2297	0.830	19.17	44.47
30.10	0.2286	0.830	17.31	39.09
30.10	0.2286	0.830	17.26	38.70
30.20	0.2276	0.830	17.32	39.09
30.20	0.2276	0.830	15.71	34.60
30.20	0.2276	0.830	15.84	35.09
30.20	0.2276	0.830	14.16	30.49
30.30	0.2265	0.830	14.30	30.59
30.30	0.2265	0.830	12.79	26.49
30.30	0.2265	0.830	12.98	26.88
30.30	0.2265	0.830	11.35	22.97
30.30	0.2265	0.830	11.33	23.16
30.30	0.2265	0.830	9.87	19.54
30.30	0.2265	0.830	9.89	19.94

TABLE XIII (Continued)

BARE MAT DATA

Run No. 67100301
Mat Thickness = 0.609 Number of Layers = 3 Mesh 9 x 9

θ Temperature, °C.	μ Viscosity, g./cm. sec.	ρ Density, $g./cm.^3$	U_∞ Velocity, cm./sec.	ΔP Press. Drop x 10^{-2}, $dynes/cm.^2$
30.20	0.2276	0.830	8.49	16.61
30.20	0.2276	0.830	8.52	16.71
30.20	0.2276	0.830	7.25	13.88
30.20	0.2276	0.830	7.23	14.07
30.20	0.2276	0.830	6.01	11.33
30.10	0.2286	0.830	5.99	11.33
30.10	0.2286	0.830	4.70	8.79
30.10	0.2286	0.830	3.08	5.47

Viscous coefficient, $\underline{A}$ = 745.68 $cm.^{-1}$
Inertial coefficient, $\underline{B}$ = 3.835
Correlation coefficient = 0.9968

TABLE XIV

BARE MAT DATA

Run No. 7100901
Mat Thickness = 0.818 Number of Layers = 4 Mesh 9 x 9

θ Temperature, °C.	μ Viscosity, g./cm. sec.	ρ Density, $g./cm.^3$	U_∞ Velocity, cm./sec.	ΔP Press. Drop x 10^{-2}, $dynes/cm.^2$
22.50	0.3378	0.834	4.40	15.73
22.50	0.3378	0.834	4.47	16.12
22.50	0.3378	0.834	5.95	21.99
22.50	0.3378	0.834	6.24	22.97
22.50	0.3378	0.834	7.85	29.42
22.60	0.3360	0.834	8.09	30.40
22.70	0.3341	0.834	9.99	38.51
22.80	0.3322	0.834	10.25	39.39
22.90	0.3304	0.834	12.51	48.87
23.00	0.3286	0.834	12.69	48.87
23.30	0.3231	0.834	14.74	57.67
23.40	0.3214	0.834	14.93	58.16
23.80	0.3144	0.833	17.13	66.76
23.90	0.3127	0.833	17.33	67.64
24.10	0.3093	0.833	18.83	73.89
24.30	0.3060	0.833	19.12	74.38
24.50	0.3027	0.833	20.44	80.15
24.80	0.2979	0.833	20.88	80.93
25.00	0.2947	0.833	19.29	72.72
25.10	0.2932	0.833	19.36	72.43
25.30	0.2901	0.833	17.95	65.88
25.40	0.2886	0.832	17.98	65.68
25.50	0.2871	0.832	16.58	59.62
25.50	0.2871	0.832	16.76	60.21
25.70	0.2841	0.832	14.98	52.39
25.90	0.2811	0.832	15.45	53.85
26.00	0.2797	0.832	13.91	47.40
26.10	0.2782	0.832	13.96	47.60
26.20	0.2768	0.832	12.40	41.54
26.20	0.2768	0.832	12.51	41.93
26.20	0.2768	0.832	10.90	35.28
26.10	0.2782	0.832	10.91	35.67
26.10	0.2782	0.832	9.50	30.30
26.10	0.2782	0.832	9.50	30.30
26.00	0.2797	0.832	7.95	25.02
26.00	0.2797	0.832	7.97	25.31
26.00	0.2797	0.832	6.66	20.52
26.00	0.2797	0.832	6.68	20.82

TABLE XIV (Continued)

BARE MAT DATA

Run No. 7100901
Mat Thickness = 0.818 Number of Layers = 4 Mesh 9 x 9

θ Temperature, °C.	μ Viscosity, g./cm. sec.	ρ Density, g./cm.^{3}	U_∞ Velocity, cm./sec.	ΔP Press. Drop x 10^{-2}, dynes/cm.^{2}
26.00	0.2797	0.832	5.24	15.93
26.00	0.2797	0.832	5.21	16.12
25.90	0.2811	0.832	4.04	12.21
25.90	0.2811	0.832	4.04	12.31
25.90	0.2811	0.832	3.16	9.48
25.80	0.2826	0.832	3.16	9.57

Viscous coefficient, A = 1017.90 cm.$^{-1}$
Inertial coefficient, B = 4.861
Correlation coefficient = 0.9956

TABLE XV

MAT-CYLINDER DATA

Run No. 67120501
Mat Thickness = 0.134 Number of Layers = 1 Mesh 6 x 6

θ Temperature, °C.	μ Viscosity, g./cm. sec.	ρ Density, $g./cm.^3$	U_∞ Velocity, cm./sec.	ΔP Press. Drop x 10^{-2}, $dynes/cm.^2$
22.80	0.3322	0.834	2.93	1.62
22.80	0.3322	0.834	4.15	2.30
22.90	0.3304	0.834	5.87	3.36
22.90	0.3304	0.834	7.46	4.48
23.10	0.3267	0.834	9.53	6.03
23.30	0.3231	0.834	12.00	7.82
23.60	0.3179	0.833	14.62	10.30
24.20	0.3076	0.833	17.03	12.20
24.60	0.3011	0.833	19.47	14.46
25.00	0.2947	0.833	20.91	15.81
25.60	0.2856	0.832	26.98	22.01
25.80	0.2826	0.832	25.92	20.61
26.30	0.2754	0.832	25.10	19.28
26.60	0.2712	0.832	23.62	17.67
27.00	0.2657	0.832	20.40	14.15
27.30	0.2618	0.831	18.66	12.52
27.50	0.2592	0.831	17.19	10.90
27.50	0.2592	0.831	15.68	9.56
27.60	0.2579	0.831	14.16	8.26
27.70	0.2566	0.831	12.69	7.15
27.70	0.2566	0.831	11.43	6.17
27.50	0.2592	0.831	9.95	5.17
27.40	0.2605	0.831	8.30	4.21
27.40	0.2605	0.831	7.08	3.36
27.40	0.2605	0.831	5.64	2.58

Viscous coefficient, $\underline{A}$ = 148.28 $cm.^{-1}$
Inertial coefficient, $\underline{B}$ = 1.759
Correlation coefficient = 0.9968

TABLE XVI

MAT-CYLINDER DATA

Run No. 67121901
Mat Thickness = 0.266 Number of Layers = 2 Mesh 6 x 6

θ Temperature, °C.	μ Viscosity, g./cm. sec.	ρ Density, g./cm.^{3}	U_∞ Velocity, cm./sec.	ΔP Press. Drop x 10^{-2}, dynes/cm.^{2}
22.50	0.3378	0.834	5.05	4.52
22.60	0.3360	0.834	6.78	6.48
22.60	0.3360	0.834	9.03	8.95
22.60	0.3360	0.834	9.13	9.02
22.95	0.3295	0.834	12.44	12.84
22.95	0.3295	0.834	12.56	13.07
23.05	0.3276	0.834	14.11	14.94
23.30	0.3231	0.834	15.89	16.98
23.30	0.3231	0.834	15.95	17.22
22.90	0.3304	0.834	17.14	19.26
22.80	0.3322	0.834	18.70	21.63
22.80	0.3322	0.834	18.80	21.79
23.05	0.3276	0.834	20.58	24.25
23.05	0.3276	0.834	20.68	24.33
23.00	0.3286	0.834	21.83	26.09
23.00	0.3286	0.834	21.88	26.41
23.00	0.3286	0.834	22.59	27.60
23.05	0.3276	0.834	23.75	29.45
23.10	0.3267	0.834	27.09	35.10
23.05	0.3276	0.834	23.34	28.73
23.15	0.3258	0.834	21.31	25.13
23.00	0.3286	0.834	19.29	22.35
22.95	0.3295	0.834	16.00	17.61
23.00	0.3286	0.834	13.34	14.01
23.00	0.3286	0.834	10.90	10.79
23.00	0.3286	0.834	10.93	10.89
23.00	0.3286	0.834	8.54	8.07
23.00	0.3286	0.834	6.57	5.89
23.00	0.3286	0.834	4.69	4.55

Viscous coefficient, A = 245.93 cm.$^{-1}$
Inertial coefficient, B = 2.158
Correlation coefficient = 0.9883

TABLE XVII

MAT-CYLINDER DATA

Run No. 67121902
Mat Thickness = 0.535 Number of Layers = 4 Mesh 6 x 6

θ Temperature, °C.	μ Viscosity, g./cm. sec.	ρ Density, g./cm.^{3}	U_∞ Velocity, cm./sec.	ΔP Press. Drop x 10^{-2}, dynes/cm.^{2}
22.85	0.3313	0.834	4.22	6.09
22.60	0.3360	0.834	5.37	8.04
22.85	0.3313	0.834	16.97	30.48
22.95	0.3295	0.834	7.15	10.79
22.95	0.3295	0.834	7.12	10.81
23.00	0.3286	0.834	8.25	12.83
23.00	0.3286	0.834	9.76	15.64
23.00	0.3286	0.834	11.60	19.02
23.00	0.3286	0.834	11.65	19.10
23.20	0.3249	0.834	13.72	23.05
22.90	0.3304	0.834	15.78	27.59
22.90	0.3304	0.834	15.77	27.67
22.90	0.3304	0.834	15.79	27.91
23.00	0.3286	0.834	18.15	32.98
23.05	0.3276	0.834	19.73	36.31
23.00	0.3286	0.834	20.93	39.49
22.90	0.3304	0.834	21.62	41.21
22.95	0.3295	0.834	22.40	43.26
22.95	0.3295	0.834	22.43	43.43
23.00	0.3286	0.834	23.45	45.90
23.00	0.3286	0.834	23.24	45.74
23.00	0.3286	0.834	23.54	45.99
23.10	0.3267	0.834	26.22	52.48
23.10	0.3267	0.834	25.78	51.23
23.00	0.3286	0.834	23.45	45.57
23.10	0.3267	0.834	21.21	39.81
23.00	0.3286	0.834	19.08	35.01
23.00	0.3286	0.834	15.94	28.07
23.15	0.3258	0.834	13.27	22.42
23.05	0.3276	0.834	10.87	17.76
23.00	0.3286	0.834	8.44	13.30
23.00	0.3286	0.834	6.31	9.52
23.00	0.3286	0.834	6.25	9.47

Viscous coefficient, A = 407.30 cm.$^{-1}$
Inertial coefficient, B = 3.127
Correlation coefficient = 0.9980

TABLE XVIII

MAT-CYLINDER DATA

Run No. 67122002
Mat Thickness = 0.802 Number of Layers = 6 Mesh 6 x 6

θ Temperature, °C.	μ Viscosity, g./cm. sec.	ρ Density, g./cm.^{3}	U_∞ Velocity, cm./sec.	ΔP Press. Drop x 10^{-2}, dynes/cm.^{2}
22.90	0.3304	0.834	4.34	8.45
22.95	0.3295	0.834	5.66	11.58
23.00	0.3286	0.834	7.12	14.70
23.00	0.3286	0.834	8.70	18.62
23.05	0.3276	0.834	10.62	23.36
23.10	0.3267	0.834	13.06	29.19
23.10	0.3267	0.834	14.69	33.86
23.05	0.3276	0.834	15.75	37.35
23.15	0.3258	0.834	17.03	40.86
23.00	0.3286	0.834	18.23	44.89
23.05	0.3276	0.834	19.80	49.46
23.00	0.3286	0.834	20.72	52.63
22.85	0.3313	0.834	21.40	55.15
22.95	0.3295	0.834	22.72	59.29
23.10	0.3267	0.834	24.56	64.99
23.10	0.3267	0.834	24.48	64.74
23.00	0.3286	0.834	22.76	58.69
23.00	0.3286	0.834	22.67	58.69
23.00	0.3286	0.834	20.38	51.54
23.00	0.3286	0.834	20.42	51.96
23.00	0.3286	0.834	17.04	41.44
23.15	0.3258	0.834	14.11	32.81
23.15	0.3258	0.834	11.68	26.23
22.95	0.3295	0.834	9.21	20.04
22.80	0.3322	0.834	6.93	14.70

Viscous coefficient, A = 560.88 cm.$^{-1}$
Inertial coefficient, B = 4.006
Correlation coefficient = 0.9959

TABLE XIX

MAT-CYLINDER DATA

Run No. 67122001
Mat Thickness = 1.064 Number of Layers = 8 Mesh 6 x 6

θ Temperature, °C.	μ Viscosity, g./cm. sec.	ρ Density, g./cm.^{3}	U_∞ Velocity, cm./sec.	ΔP Press. Drop x 10^{-2}, dynes/cm.^{2}
23.00	0.3286	0.834	3.29	8.03
23.00	0.3286	0.834	4.85	12.60
23.00	0.3286	0.834	6.62	17.69
23.00	0.3286	0.834	6.67	17.92
23.05	0.3276	0.834	9.01	24.89
23.05	0.3276	0.834	11.54	32.99
23.15	0.3258	0.834	14.16	41.55
22.95	0.3295	0.834	16.44	50.16
23.05	0.3276	0.834	18.04	55.95
23.05	0.3276	0.834	18.15	56.28
23.00	0.3286	0.834	19.85	62.56
23.00	0.3286	0.834	19.99	63.16
22.90	0.3304	0.834	20.99	67.36
22.90	0.3304	0.834	22.09	72.03
22.90	0.3304	0.834	22.21	72.46
23.00	0.3286	0.834	24.34	80.60
23.05	0.3276	0.834	24.51	81.22
23.10	0.3267	0.834	24.47	80.52
23.00	0.3286	0.834	24.92	83.08
23.00	0.3286	0.834	22.14	72.38
23.00	0.3286	0.834	22.62	74.12
23.00	0.3286	0.834	20.99	66.33
23.00	0.3286	0.834	17.98	55.61
23.00	0.3286	0.834	14.97	44.68
22.95	0.3295	0.834	12.41	35.75
23.00	0.3286	0.834	10.05	28.00
23.00	0.3286	0.834	7.91	21.24
23.00	0.3286	0.834	6.02	15.65

Viscous coefficient, A = 729.64 cm.$^{-1}$
Inertial coefficient, B = 4.578
Correlation coefficient = 0.9955

TABLE XX

MAT-CYLINDER DATA

Run No. 67122701
Mat Thickness = 0.212 Number of Layers = 1 Mesh 9 x 9

θ Temperature, °C.	μ Viscosity, g./cm. sec.	ρ Density, g./cm.^{3}	U_∞ Velocity, cm./sec.	ΔP Press. Drop x 10^{-2}, dynes/cm.^{2}
23.10	0.3267	0.834	2.13	2.04
23.00	0.3286	0.834	3.03	3.12
22.95	0.3295	0.834	4.46	5.09
22.90	0.3304	0.834	6.40	7.86
22.90	0.3304	0.834	6.44	7.95
22.95	0.3295	0.834	8.29	10.59
22.95	0.3295	0.834	8.39	10.74
23.00	0.3286	0.834	10.67	14.17
23.00	0.3286	0.834	10.80	14.40
23.05	0.3276	0.834	13.35	18.25
23.05	0.3276	0.834	13.46	18.40
23.05	0.3276	0.834	15.34	21.48
23.05	0.3276	0.834	15.42	21.64
23.00	0.3286	0.834	16.93	24.18
23.00	0.3286	0.834	17.00	24.18
22.90	0.3304	0.834	18.68	26.73
22.85	0.3313	0.834	18.91	27.21
22.80	0.3322	0.834	20.05	29.94
22.80	0.3322	0.834	20.11	30.02
22.90	0.3304	0.834	21.30	31.55
23.10	0.3267	0.834	22.08	32.28
23.05	0.3276	0.834	24.47	36.66
23.50	0.3196	0.834	24.53	36.82
23.50	0.3196	0.834	22.22	32.04
23.40	0.3214	0.834	20.81	29.62
23.10	0.3267	0.834	17.48	23.86
23.10	0.3267	0.834	17.48	23.94
23.00	0.3286	0.834	14.43	19.03
23.00	0.3286	0.834	12.08	15.26
23.05	0.3276	0.834	9.75	11.83
23.10	0.3267	0.834	7.52	8.77
23.10	0.3267	0.834	7.57	8.83

Viscous coefficient, $\underline{A}$ = 319.23 cm.$^{-1}$
Inertial coefficient, $\underline{B}$ = 2.446
Correlation coefficient = 0.9451

TABLE XXI

MAT-CYLINDER DATA

Run No. 67122702
Mat Thickness = 0.394 Number of Layers = 2 Mesh 9 x 9

θ Temperature, °C.	μ Viscosity, g./cm. sec.	ρ Density, g./cm.^{3}	$\underline{U}_\infty$ Velocity, cm./sec.	$\Delta\underline{P}$ Press. Drop x 10^{-2}, dynes/cm.^{2}
23.05	0.3276	0.834	3.70	7.47
23.05	0.3276	0.834	3.71	7.45
23.00	0.3286	0.834	4.85	10.22
23.00	0.3286	0.834	4.95	10.28
23.00	0.3286	0.834	6.38	13.76
23.05	0.3276	0.834	8.03	17.75
23.05	0.3276	0.834	8.05	17.68
23.00	0.3286	0.834	9.96	22.41
23.05	0.3276	0.834	12.14	27.99
23.00	0.3286	0.834	13.31	31.36
22.90	0.3304	0.834	15.51	38.00
22.90	0.3304	0.834	16.89	41.28
22.90	0.3304	0.834	16.99	41.36
23.05	0.3276	0.834	18.02	45.06
23.05	0.3276	0.834	18.05	45.06
23.30	0.3231	0.834	19.58	49.13
23.30	0.3231	0.834	19.74	49.62
23.20	0.3249	0.834	20.88	54.06
23.10	0.3267	0.834	21.63	55.99
23.00	0.3286	0.834	22.62	59.37
23.00	0.3286	0.834	24.29	64.83
23.00	0.3286	0.834	24.35	65.34
23.00	0.3286	0.834	22.07	57.43
23.00	0.3286	0.834	22.09	57.60
22.95	0.3295	0.834	20.60	53.72
22.90	0.3304	0.834	17.84	44.65
22.90	0.3304	0.834	17.80	44.73
22.90	0.3304	0.834	14.80	35.73
22.95	0.3295	0.834	14.89	35.97
23.00	0.3286	0.834	12.21	28.15
23.05	0.3276	0.834	9.93	22.09
23.05	0.3276	0.834	9.95	22.17
23.05	0.3276	0.834	7.66	16.42
23.05	0.3276	0.834	5.71	11.74

Viscous coefficient, $\underline{A}$ = 586.20 cm.$^{-1}$
Inertial coefficient, $\underline{B}$ = 3.764
Correlation coefficient = 0.9948

TABLE XXII

MAT-CYLINDER DATA

Run No. 67122801
Mat Thickness = 0.610 Number of Layers = 3 Mesh 9 x 9

θ Temperature, °C.	μ Viscosity, g./cm. sec.	ρ Density, $g./cm.^3$	U_∞ Velocity, cm./sec.	ΔP Press. Drop x 10^{-2}, $dynes/cm.^2$
22.95	0.3295	0.834	3.58	10.27
22.90	0.3304	0.834	4.87	14.48
22.90	0.3304	0.834	6.45	19.98
22.95	0.3295	0.834	8.47	26.81
23.00	0.3286	0.834	10.68	34.06
23.15	0.3258	0.834	12.94	41.81
23.10	0.3267	0.834	15.38	52.10
23.00	0.3286	0.834	16.58	56.81
23.30	0.3231	0.834	18.15	63.27
23.30	0.3231	0.834	19.79	70.15
23.20	0.3249	0.834	21.02	75.72
23.10	0.3267	0.834	21.83	79.31
23.15	0.3258	0.834	22.97	84.79
23.05	0.3276	0.834	21.54	78.52
23.00	0.3286	0.834	18.68	66.61
23.20	0.3249	0.834	15.64	53.11
23.20	0.3249	0.834	12.85	42.47
23.10	0.3267	0.834	10.44	33.49
23.00	0.3286	0.834	8.10	25.46
23.00	0.3286	0.834	5.35	16.12

Viscous coefficient, $\underline{A}$ = 845.33 $cm.^{-1}$
Inertial coefficient, $\underline{B}$ = 4.889
Correlation coefficient = 0.9939

TABLE XXIII

MAT-CYLINDER DATA

Run No. 67122802
Mat Thickness = 0.818 Number of Layers = 4 Mesh 9 x 9

θ Temperature, °C.	μ Viscosity, g./cm. sec.	ρ Density, $g./cm.^3$	U_∞ Velocity, cm./sec.	ΔP Press. Drop x 10^{-2}, $dynes/cm.^2$
22.95	0.3295	0.834	4.11	14.75
22.95	0.3295	0.834	5.22	20.29
22.95	0.3295	0.834	5.26	20.45
23.00	0.3286	0.834	6.85	27.38
23.00	0.3286	0.834	8.61	34.96
23.00	0.3286	0.834	10.62	43.85
23.05	0.3276	0.834	12.54	54.03
22.95	0.3295	0.834	14.74	65.36
23.00	0.3286	0.834	15.93	71.40
22.95	0.3295	0.834	17.28	78.73
22.95	0.3295	0.834	18.71	86.80
23.00	0.3286	0.834	19.99	93.65
23.10	0.3267	0.834	21.17	99.27
23.05	0.3276	0.834	21.74	103.02
23.10	0.3267	0.834	22.91	109.70
23.10	0.3267	0.834	22.91	109.78
23.00	0.3286	0.834	21.09	97.64
23.00	0.3286	0.834	19.29	92.02
22.95	0.3295	0.834	16.22	73.11
23.00	0.3286	0.834	13.40	58.27
23.00	0.3286	0.834	11.00	46.05
23.05	0.3276	0.834	8.68	35.12
23.05	0.3276	0.834	5.99	23.14

Viscous coefficient, A = 1080.81 $cm.^{-1}$
Inertial coefficient, B = 6.773
Correlation coefficient = 0.9840